OUKA
Osaka University Knowledge Archive

Title	Development of plasma-based nano-precision figuring and finishing techniques for brittle functional materials
Author(s)	Sun, Rongyan
Citation	大阪大学, 2022, 博士論文
Version Type	VoR
URL	https://doi.org/10.18910/88027
rights	
Note	

Osaka University Knowledge Archive : OUKA

https://ir.library.osaka-u.ac.jp/

Osaka University

Doctoral Dissertation

Development of plasma-based nano-precision figuring and finishing techniques for brittle functional materials

Rongyan Sun

December 2021

Graduate School of Engineering,
Osaka University

Table of Contents

Page

Chapter 1 Background **1**
1.1 Introduction 1
1.2 Difficult-to-machine brittle functional materials using convention manufacturing techniques 2
1.2.1 Ultrathin quartz crystal wafer 2
1.2.2 Reaction-sintered silicon carbide (RS-SiC) 4
1.2.3 Aluminum nitride (AlN) ceramics 6
1.3 Motivation of this study 7
1.4 Thesis organization 7
References 8

Chapter 2 Plasma nanomanufacturing process **12**
2.1 Introduction 12
2.2 Current figuring techniques 13
2.2.1 Ultraprecision cutting 13
2.2.2 Ion beam figuring 14
2.2.3 Wet-etch figuring 15
2.3 Current polishing techniques 16
2.3.1 Chemical mechanical polishing 16
2.3.2 Catalyst-referred etching 18
2.3.3 Ultraviolet-assisted polishing 19
2.3.4 Electrochemical mechanical polishing 20
2.3.5 Magnetorheological finishing 21
2.4 Plasma nanomanufacturing process proposal 22
2.4.1 Introduction 22
2.4.2 Basics of plasma for processes 23
2.4.2.1 Collision between electron and molecule/atom in plasma 23
2.4.2.2 Spectroscopic measurements of plasma emission light 24
2.4.2.3 Difference between atmospheric-pressure plasma and vacuum plasma 26
2.4.3 Plasma chemical vaporization machining (PCVM) 29
2.4.4 Plasma-assisted polishing (PAP) 30
2.4.5 Strategies of plasma nanomanufacturing process 31

2.5 Summary 33
References 34

Chapter 3 Optimization of AP-PCVM technique for processing ultra-thin quartz crystal wafer 41
3.1 Introduction 41
3.2 AP-PCVM setup 41
3.3 Current application of AP-PCVM to ultra-thin quartz crystal wafer 42
3.4 Challenge of using Ar instead of He as the carrier gas in AP-PCVM 44
3.5 Penning effect caused by adding ethanol to Ar plasma 45
3.6 Different etching characteristics using Ar and He as the carrier gas in AP-PCVM 49
3.6.1 Shape of removal spot 53
3.6.2 Etching rate 55
3.7 Summary 57
References 58

Chapter 4 Application of plasma nanomanufacturing process to RS-SiC 61
4.1 Introduction 61
4.2 Figuring of RS-SiC by AP-PCVM 61
4.2.1 Microwave AP-PCVM setup used in this work 61
4.2.2 Processing gap 62
4.2.2.1 Analysis of gas distribution in different processing gap using computational fluid dynamics simulation 63
4.2.2.2 Relationship between processing gap and etching rate 70
4.2.3 Causes of deterioration of surface roughness after AP-PCVM 72
4.2.4 Optimization of processing conditions for gas composition 74
4.2.4.1 Correlation between gas composition and etching rate of Si (100) & SiC (0001) 74
4.2.4.2 Mechanism for the change of etching rate under different gas composition 76
4.2.4.3 Improvement of surface roughness of RS-SiC by optimizing gas composition. 80
4.2.4.4 Raster scanning results for AP-PCVM on RS-SiC using optimized gas composition 82
4.2.5 Aspherical shape figuring of RS-SiC by AP-PCVM 85
4.2.6 Optimization of processing conditions: Substrate temperature 87
4.2.6.1 Effect of substrate temperature on redeposition of reaction products 87
4.2.6.2 Effect of substrate temperature on etching rate 89

4.3 Surface finishing of RS-SiC by PAP 90
4.4 Summary 90
References 92

Chapter 5 Highly efficient and dress-free dry polishing technique with plasma-assisted surface modification and dressing 94
5.1 Introduction 94
5.2 Vacuum PAP setup used in this work 95
5.3 Different fixed abrasive grinding stone distinguished according to the type of bond materials 97
5.4 Polishing properties of vitrified-bonded grinding stones with different abrasive particle sizes for conventional dry polishing method 98
5.5 Loading of the grinding stone surface under ultra-low polishing pressure 101
5.6 Increase in MRR by dressing the surface of the grinding stone and cleaning the surface of AlN ceramics wafer 104
5.7 Self-sharpening technique of metal-bonded grinding stones using electrolytic in-process dressing (ELID) 105
5.8 Modification of AlN ceramics wafer by Ar-based CF_4 plasma irradiation 107
5.9 Selection of abrasive particles materials used in PAP 109
5.10 Change of adsorption force between abrasive particles and AlN ceramics surface after Ar-based CF_4 plasma irradiation 111
5.11 Dress-free polishing of AlN ceramics wafer in PAP 114
    5.11.1 Preliminary polishing of AlN grinded surface 114
    5.11.2 Fine surface finishing of AlN polished surface 120
5.12 Dress-free polishing model using CF_4 plasma and a vitrified-bonded grinding stone 123
5.13 Summary 125
References 127

Chapter 6 Summary 130

Acknowledgments 137

Chapter 1
Background

1.1 Introduction

The four industrial revolutions that begun in 1760, promoted the development of human civilization. The innovation of processing and manufacturing technology played an important role in each industrial revolution. The first major shift was in the first industrial revolution (Industry 1.0) between 1760 to 1820 and 1840 [1]. Due to the development of manufacturing technology, humans began to use steam engines and other machines in place of hand production to improve production efficiency, thus, bringing human civilization to the age of machines. With the continuous advancement of manufacturing technology, came the second industrial revolution (Industry 2.0), also known as the technological revolution [2], which dated between 1870 and 1914. This stage of revolution brought about more accuracy in manufacturing, owing to the advent of electricity and modern production lines. The third industrial revolution (Industry 3.0), also known as the digital revolution began in the latter half of the 20th century. This era witnessed the production of the world's first electronic computer built at the University of Pennsylvania in 1945 and was officially pronounced as the digital age in human civilization. Central to this revolution era was the mass production and widespread use of metal-oxide-semiconductor field effect transistors (MOSFETs), integrated circuit (IC) chips, and their derived technologies [3]. This stage witnessed a high manufacturing accuracy to the micron or even submicron scale for processing high-performance semiconductor devices. In the 21st century, the fourth industrial revolution (Industry 4.0) was proposed by the German government in 2011. This revolution stage witnessed the promotion of the automation of traditional manufacturing and industrial practices, and the main aim was modern smart technology. However, large-scale machine-to-machine communication (M2M) and Internet of Things require higher-performance semiconductor devices to achieve high-speed transmission of information. Therefore, the manufacturing precision of higher-performance semiconductor devices has also been further improved to nanometer or even subnanometer scale.

In September 2015, the United Nations proposed the Sustainable Development Goals to achieve a better and more sustainable future for all [4]. To achieve the goals of energy saving and ecofriendly environment, semiconductor substrate materials were transformed from silicon (Si) to silicon carbide (SiC), gallium nitride (GaN), diamond and other materials with wide band gap

[5-9]. In the field of communication devices, to increase the communication speed, the resonance frequency of the quartz crystal unit is increased by reducing the thickness of the quartz crystal wafer [10]. To manufacture more durable lens molds and lighter space telescopes, for optical and imaging devices, reaction-sintered silicon carbide (RS-SiC) is a promising material. Although these materials are proven to have very excellent properties, however, it is essential to develop ultraprecision manufacturing technique for these materials.

1.2 Difficult-to-machine brittle functional materials using conventional manufacturing techniques

Conventional mechanical manufacturing processes such as turning, and grinding have been developed several years ago, but, however, have certain limitations. Such as equipment accuracy, surrounding environment (vibration *et al.*) and other factors. Also, a damage layer formed on the surface of substrate during the conventional mechanical manufacturing process, affects the properties of the substrate itself. There are difficulties in achieving the required manufacturing accuracy working with difficult-to-machine brittle functional materials, which are materials with high hardness, strong chemical inertness, and brittle (broken easily), through conventional mechanical manufacturing methods. Three kinds of difficult-to-machine brittle functional materials are investigated in this study: ultrathin quartz crystal wafer, RS-SiC, and aluminum nitride (AlN) ceramic.

1.2.1 Ultrathin quartz crystal wafer

Piezoelectric effect was discovered in 1880 by the French physicists Jacques and Pierre Curie [11]. Piezoelectric effect occurs when electricity is generated on the surface of a crystal unit due to mechanical pressure. Conversely, when electricity is applied to the surface, mechanical strain is generated (inverse piezoelectric effect). The piezoelectric effect of several materials such as ceramics have been confirmed. Quartz crystal is readily available and has the most accurately measured and stable frequency. For this reason, it has been used as an essential electronic component in various devices. Devices made of quartz crystals include quartz crystal units, crystal oscillators, crystal filters, and optical devices.

Quartz crystal units, such as AT-cut [12] and GT-cut [13] crystal units, have a zero-temperature coefficient over a broad temperature range, centered around room temperature and therefore have excellent frequency-temperature characteristics. More so, quartz crystal units are extremely stable both physically and chemically, and consequently, the frequency change with aging is extremely small. Owing to this excellent frequency stability, quartz crystal units are used in communication devices such as cell phones and wireless applications as well as consumer devices such as televisions, video recorders, digital cameras, and computers to provide accurate reference signals

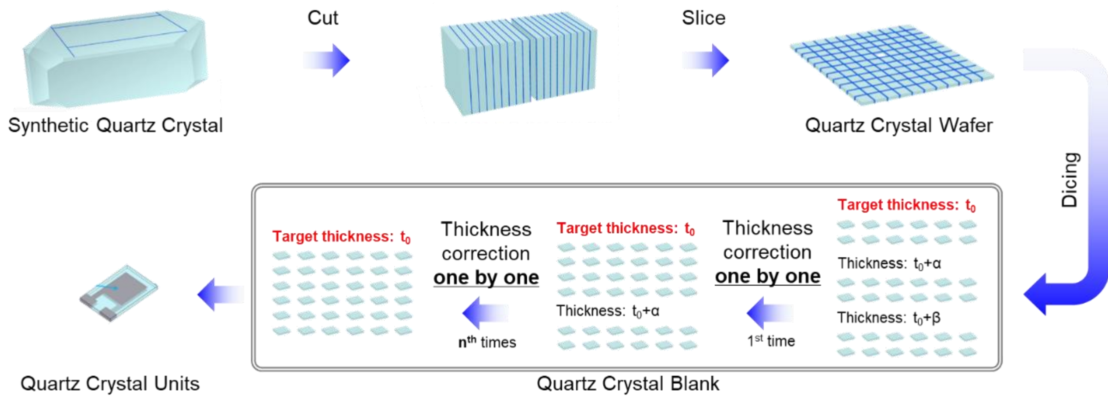

Figure 1.1 Previous commercial production process of quartz crystal unit.

for simultaneous and quick processing huge volume of information. The relationship between resonance frequency f_0 and thickness of quartz crystal blank t_0 can be written as follow:

$$f_0\ [\mathrm{MHz}] = \frac{1670}{t_0\ [\mu\mathrm{m}]}$$

To increase the communication speed, the resonance frequency of the quartz crystal unit should be increased by reducing the thickness of the quartz crystal blank. For an 80 MHz crystal unit, the thickness is only around 20 μm. Since quartz crystal is a type of brittle material, it breaks easily due to mechanical force during conventional mechanical manufacturing process. In previous commercial production of quartz crystal unit, quartz crystal wafer is produced by firstly dicing the crystals into blanks of the target sizes. Due to the uneven thickness of the quartz crystal wafer, the thickness deviation of the quartz crystal blanks is relatively large. To produce quartz crystal units with target resonance frequency, the thickness of quartz crystal blank must be corrected to the target value one after another, to low efficiency (Fig. 1.1). In the recent commercial production of quartz crystal unit, a wafer process was intensively developed to

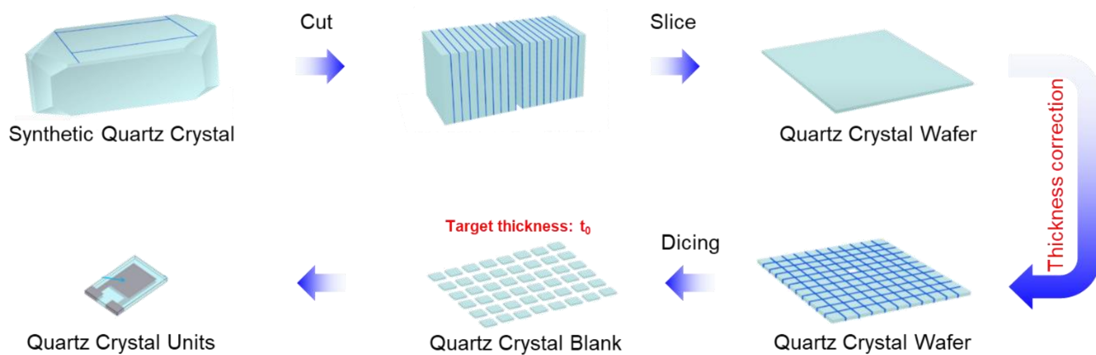

Figure 1.2 Recent commercial production process of quartz crystal unit using wafer process.

improve the productivity of resonators (Fig. 1.2). To improve the productivity of resonators by reducing the processing time for frequency adjustment, a uniform thickness of the quartz crystal wafer is essential. However, commercially available quartz crystal wafers typically have a thickness deviation of ±0.1%, which is induced by conventional mechanical fabrication processes such as cutting with a wire saw, lapping, ion beam figuring, and polishing. This value is about 100-fold larger than the tolerance required for a commercial product. Furthermore, owing to the poor parallelism and the existence of subsurface damage, many spurious peaks, which deteriorate the resonance characteristics were observed in the resonance curve [14)]. Therefore, a highly efficient and damage-free thickness-correction technique for ultrathin quartz crystal wafer is essential.

1.2.2 Reaction-sintered silicon carbide (RS-SiC)

RS-SiC is a very promising material to produce equipment parts for optical mirror devices in space telescope systems, molds for optical components, semiconductor and the manufacturing of liquid crystal display and various production facilities due to their excellent properties, such as light weight, high rigidity, high thermal conductivity and low thermal expansion coefficient. Table 1.1 shows the mechanical properties of tungsten carbide (WC) and RS-SiC. As a type of mold material for optical components, compared with traditionally used WC, RS-SiC has higher hardness, significant of its strong resistance to wear due to abrasion as well as formation of scratches and subsurface damage (SSD). Also, RS-SiC has high durability against high-temperature oxidation, making it suitable for use in long-life applications. RS-SiC has high thermal conductivity and a low thermal expansion coefficient, depicting a very low chance of shape failures due to nonuniformity of the temperature distribution in the molding process [15-19)]. Since the main component of RS-SiC is silicon carbide, RS-SiC is difficult to machine due to its

Table1.1 Mechanical properties of WC and RS-SiC [18, 19)]

	WC	RS-SiC
Vickers hardness (GPa)	17-21	24-28
Coefficient of thermal expansion (10^{-6}/K)	5	2.5
Thermal conductivity (W/m・K)	70	130
Young's modulus (GPa)	190	362
Density (10^3 kg/m^3)	14.5	3.03
Melting point (ºC)	2785	1410 (Si)
Machinability	Comparatively good	Inferior

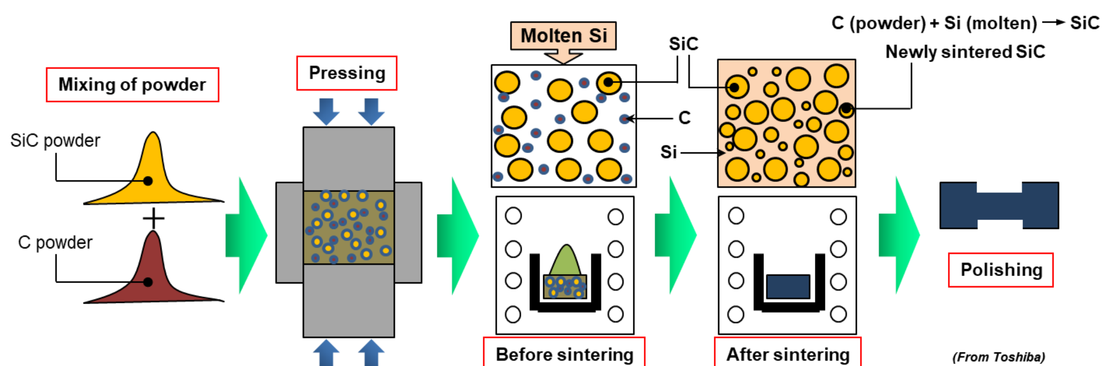

Figure 1.3 Fabrication process flowchart for RS-SiC.

high hardness and chemical inertness [20-27]. Fig. 1.3 shows the fabrication process flowchart for RS-SiC. The slurry used was a mixture of SiC powder, carbon powder and water with some dispersant. The original preforms, the green body, was formed by pressure casting of the slurry. The green body was dried and then reaction-sintered at 1693 K in vacuum together with the molten silicon [28]. Figure 1.4 shows the scanning electron microscope (SEM) image of RS-SiC, SiC component and Si component were both confirmed. However, owing to the difference in the chemical and mechanical properties of SiC and Si grains, it is difficult to form an objective shape with an ultrasmooth surface. Conventional techniques such as turning and grinding using diamond are used in the formation of shapes with high precision, high efficiency, and low cost. However, scratches and an SSD layer are inevitably formed on the machined surface. Therefore, a highly efficient, high-quality, and damage-free figuring and finishing technique for RS-SiC is essential.

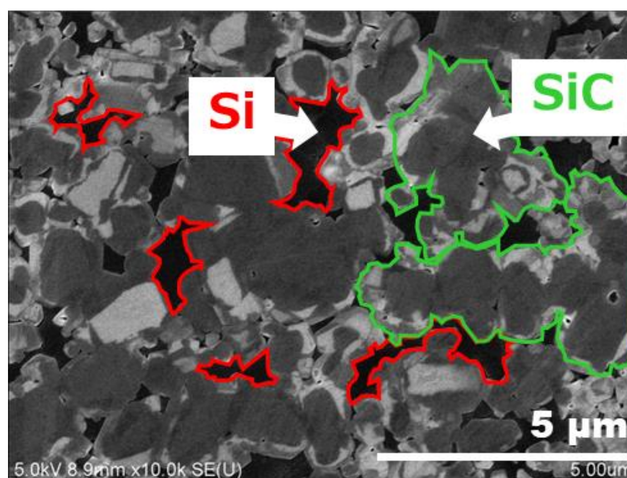

Figure 1.4 SEM image of RS-SiC.

1.2.3 Aluminum nitride (AlN) ceramics

AlN is an excellent choice material for heat sinks and microelectronics applications [29, 30] owing to its high thermal conductivity of 285 $Wm^{-1}K^{-1}$, [31] that is comparable to that of silicon carbide and ~5–7 times greater than that of alumina, high mechanical strength with Vickers hardness of 17 GPa [32], relatively low dielectric constant of 8.5 [33], and low thermal expansion coefficient of 1.8×10^{-8}/K [34]. Furthermore, metalorganic chemical vapor phase epitaxy of gallium nitride (GaN) is currently performed on sapphire and silicon substrates [35-37]. Table 1.2 shows the lattice constant (300 K) and coefficients of thermal expansion (CTE) of GaN, Si, sapphire, and AlN [36, 38]. During the epitaxy process, the large lattice mismatch between GaN and sapphire ~13.9% [39] and between GaN and silicon ~16.9% [36, 37] and the differences in their CTE lead to the formation of cracks when the thickness of the deposited layer exceeds a critical value [40]. AlN buffer layer has been widely used to grow GaN thin films with optically flat crack-free surfaces [41] due to the small lattice mismatch between GaN and AlN ~2.4% [42]. Additionally, the in-plane lattice of AlN is smaller than that of GaN, and this lattice mismatch between AlN and GaN can induce the compressive stress in the GaN layer that can compensate for the tensile stress originating from the mismatch of the CTE [43]. However, it is difficult to produce high quality single-crystal AlN wafer. In recent years, research on the use of AlN substrates as an epitaxial growth substrate in the deposition of a single-crystal AlN film on AlN ceramic, has attracted considerable attention. When subjected to a large mechanical polishing load, grains tend to shed off of the surface of AlN ceramic owing to their weak intergranular interactions, making it difficult to obtain a smooth surface by traditional mechanical polishing. More so, AlN easily reacts with water, and thus, an alternative high-efficiency dry polishing technique that can avoid the shedding-off of AlN grains is desired.

Table 1.2 Lattice constant (300 K) and thermal expansion coefficients of GaN, Si, sapphire, and AlN [36, 38]

	Symmetry	Axis	Lattice constant (Å)	CTE (10^{-6}/K)
GaN	Hexagonal	a-axis	3.189	5.6
		c-axis	5.185	3.2
Si	Cubic	a-axis	5.431	3.6
Sapphire	Hexagonal	a-axis	4.758	7.3
		c-axis	12.983	8.1
AlN	Hexagonal	a-axis	3.111	5.3
		c-axis	4.979	4.2

1.3 Motivation of this study

As described in the previous sections, there are several challenges in the figuring and finishing of difficult-to-machine brittle functional materials to achieve excellent properties in actual products. The motivation of this study is to develop a novel manufacturing technique to resolve the challenges in the current figuring and finishing techniques for these brittle functional materials.

In this study, plasma nanomanufacturing process, which consists of plasma chemical vaporization machining (PCVM) for figuring with nanometer-order form accuracy and plasma-assisted polishing (PAP) for atomically smooth damage-free finishing, was proposed and developed. Plasma nanomanufacturing process using different process gases can be applied for the different processing requirements of different brittle functional materials.

1.4 Thesis organization

This thesis consists of six chapters.

In Chapter 1, the background of this study, the properties and applications of the difficult-to-machine brittle functional materials that will be polished in this study and the aims of this study are described.

In Chapter 2, a review of the current figuring and polishing technique was conducted and their advantages and disadvantages were summarized. To realize highly efficient, cost effective, and damage-free nanoscale manufacturing of different brittle functional materials for different targets, plasma nanomanufacturing process, which combines PCVM and PAP, was proposed. The basics of the use of plasma for processes, and the concepts and strategies of plasma nanomanufacturing process are described.

In Chapter 3, by optimizing the composition of the process gas and some other processing conditions, a stable plasma was generated under atmospheric pressure using ethanol-added Ar as the carrier gas. The replacement of He using ethanol-added Ar as carrier gas made the commercialized AP (atmospheric pressure)-PCVM technology successfully get rid of the unstable supply of He, and reduced production costs under the premise of ensuring the removal rate.

In Chapter 4, by combining the computational fluid dynamics (CFD) simulation results and the experimental results in AP-PCVM, the relationship between the processing gap and the processing characteristics was clarified. Furthermore, by optimizing the oxygen fraction in the process gas, an optimal gas composition for the meeting point between the etching rate of the two components (SiC and Si) in RS-SiC was found, and a smooth processed RS-SiC surface was obtained by AP-PCVM. AP-PCVM was firstly applied to process a multicomponent materials, and thus have further broadened the application of plasma nanomanufacturing process.

In Chapter 5, a novel dry high-efficiency dress-free polishing technique using CF_4 plasma and a vitrified-bonded grinding stone was achieved. In the case of PAP using CF_4 plasma and a vitrified-bonded grinding stone, the CF_4 plasma irradiation not only generated an easily removable and modified layer on the substrate surface but also dressed the grinding stone surface by etching the main components of the bond materials. Owing to the simultaneous plasma-assisted dressing (PAD) occurring in the PAP process, a novel highly-efficient dress-free polishing process was achieved. Thus, the combined contribution of PAP and PAD resulted in twice the material removal rate (MRR) compared with mechanical dry polishing processes without dressing. In the manufacturing process of functional ceramic materials, ultralow pressure dry polishing using CF_4 plasma and vitrified-bonded grinding stones with small abrasive particles is a very promising technique for replacing conventional mechanical polishing processes.

In Chapter 6, we provided the summary of the thesis and recommendations from the work.

References

1) European Route of Industrial Heritage. Council of Europe. Retrieved 2 June 2021.
2) Muntone, Stephanie. "Second Industrial Revolution". Education.com. The McGraw-Hill Companies. Archived from the original on 22 October 2013. Retrieved 14 October 2013.
3) R. Debjani, Cinema in the Age of Digital Revolution, *International Journal of Interdisciplinary and Multidisciplinary Studies.* **1** (2014) 107-111.
4) United Nations (2017) Resolution adopted by the General Assembly on 6 July 2017, Work of the Statistical Commission pertaining to the 2030 Agenda for Sustainable Development
5) H. Okumura, Present Status and Future Prospect of Widegap Semiconductor High-Power Devices, *Japanese Journal of Applied Physics.* **45** (2006) 7565-7586.
6) S. J. Pearton, C. R. Abernathy, D. P. Norton, A. F. Hebard, Y. D. Park, L. A. Boatner and J. D. Budai, Advances in wide bandgap materials for semiconductor spintronics, *Materials Science and Engineering R.* **40** (2003) 137-168.
7) T. Funaki, J. C. Balda, J. Junghans, A. S. Kashyap, H. A. Mantooth, F. Barlow, T. Kimoto and T. Hikihara, Power Conversion with SiC Devices at Extremely High Ambient Temperatures, *IEEE Transactions on Power Electronics.* **22** (2007) 1321-1329.
8) P. Schlotter, J. Baur, Ch. Hielscher, M. Kuner, H. Obloh, R. Schmidt and J. Schneider, Fabrication and characterization of GaN/InGaN/AlGaN double heterostructure LEDs and their application in luminescence conversion LEDs, *Materials Science and Engineering.* **B59** (1999) 390-394.
9) H. Umezawa, M. Nagase, Y. Kato and S. Shikata, High temperature application of diamond power device, *Diamond & Related Materials.* **24** (2012) 201-205.
10) R. Sun, X. Yang, K. Watanabe, *et al.*, Etching characteristics of quartz crystal wafers using argon-based

atmospheric pressure CF_4 plasma stabilized by ethanol addition, *Nanomanufacturing and Metrology.* **2** (2019) 168-176.

11) A. Manbachi, RSD. Cobbold, Development and application of piezoelectric materials for ultrasound generation and detection, *Ultrasound.* **19** (2011) 187-196.
12) L. Pan, J. Krim, Scanning tunneling microscope-quartz crystal microbalance study of temperature gradients at an asperity contact, *Review of Scientific Instruments.* **84** (2013) 014901.
13) M. Nakazawa, S. Kozima, A study of GT-Type quartz crystal plates, *IEEE Transactions on Sonics and Ultrasonics.* **29** (1982) 121-127.
14) Y. Nagaura, S. Yokomizo, Manufacturing method of high frequency quartz oscillators over 1 GHz, *Proceedings of the 1999 IEEE International Frequency Control Symposium*. (1999) 425-428.
15) S.P. Simner, P. Xiao, B. Derby, Processing and microstructural characterisation of RBSiC-$TaSi_2$ composites, *Journal of Materials Science*. **33** (1998) 5557-5568.
16) A. Khounsary, P. Fernandez, L. Assoufid, *et al.* Design, fabrication, and evaluation of an internally cooled silicon carbide mirror, *Review of Scientific Instruments*. **73** (2002) 1537-1540.
17) J. Li, S. Sugimoto, S. Tanaka, M. Esashi, R. Watanabe, Manufacturing silicon carbide microrotors by reactive hot isostatic pressing within micromachined silicon molds, *Journal of the American Ceramic Society*. **85** (2002) 261-263.
18) H. Kim, I. Shon, I. Ko, J. Yoon, J. Doh, G. Lee, Fabrication of ultrafine binderless WC and WC-Ni hard materials by a pulsed current activated sintering method, *Journal of Ceramic Processing Research*. **7** (2006) 224-229.
19) S. Suyama, Y. Itoh, High-strength reaction-sintered silicon carbide for large-scale mirrors -effect of surface oxide layer on bending strength-, *Advances in Science and Technology*. **63** (2010) 374-382.
20) K. Biswas, G. Rixecker, F. Aldinger, Improved high temperature properties of SiC-ceramic sintered with Lu_2O_3-containg additives, *Journal of the European Ceramic Society*. **23** (2006) 1099-1104.
21) T. S. Suzuki, T. Uchikoshi, Y. Sakka, Effect of sintering conditions on microstructure in α-SiC prepared by slip casting in a strong magnetic field, *Journal of the European Ceramic Society*. **30** (2010) 2813-2817.
22) A. L. Ortiz, O. Borrero-Lopez, M. Z. Quadir, F. Guiberteau, A route for the pressureless liquid-phase sintering of SiC with low additive content for improved-wear resistance, *Journal of the European Ceramic Society*. **32** (2012) 965-973.
23) M. Herrmann, K. Sempf, M. Schneider, U. Sydow, K. Kremmer, A. Michaelis, Electrochemical corrosion of silicon carbide ceramics in H_2SO_4**,** *Journal of the European Ceramic Society*. **34** (2014) 229-235.
24) Y. K. Seo, Y. W. Kim, T. Nishimura, W. S. Seo, High-temperature strength of a thermally conductive silicon carbide ceramic sintered with yttria and Scandia, *Journal of the European Ceramic Society.* **36** (2016) 3755-3760.

25) A. Kovalcikova, J. Sedlacek, Z. Lences, R. Bystricky, H. Dusza, P. Saigalik, Oxidation resistance of SiC ceramics prepared by different processing routes, *Journal of the European Ceramic Society*. **36** (2016) 3783-3973.
26) M. Herrmann, K. Sempf, H. Wendrock, M. Schneider, K. Kremmer, A. Michaelis, Electrochemical corrosion of silicon carbide ceramics in sodium hydroxide, *Journal of the European Ceramic Society*. **34** (2014) 1687-1693.
27) J. Breysse, D. Castel, B. Laviron, D. Logut, M. Bougoin, All-SiC telescope technology: recent progress and achievements, *Proceedings of the 5th International Conference on Space Optics, Toulouse*. (2004) 659-671.
28) S. Suyama, T. Kameda, Y. Itoh, Development of high-strength reaction-sintered silicon carbide, *Diamond and Related Materials*. **12** (2003) 1201-1204.
29) K. Nam, K. Hong, H. Park, H. Choe, Facile synthesis of power-based processing of porous aluminum nitride, *Journal of the European Ceramic Society.* **38** (2018) 1164-1169.
30) M. Qin, H. Lu, H. Wu, Q. He, C. Liu, X. Mu, Y. Wang, B. Jia, X. Qu, Powder injection molding of complex-shaped aluminium nitride ceramic with high thermal conductivity, *Journal of the European Ceramic Society*. **39** (2019) 952-956.
31) A. Franco-Junior, D. J. Shanafield, Thermal conductivity of polycrastalline aluminium nitride (AlN) ceramics, *Ceramica.* **50** (2004) 247-253.
32) I. Yonenaga, Thermo-mechanical stability of wide-bandgap semiconductors: high temperature hardness of SiC, AlN, GaN, ZnO and ZnSe, *Physica B.* **308-310** (2001) 1150-1152.
33) K. A. Khor, K. H. Cheng, L. G. YU, F. Boey, Thermal conductivity and dielectric constant of spark plasma sintered aluminum nitride, *Materials Science and Engineering.* **A347** (2003) 300-305.
34) W. M. Yim, R. J. Paff, Thermal expansion of AlN, sapphire, and silicon, *Journal of Applied Physics.* **45** (1974) 1456-1457.
35) Y. Kato, S. Kitamura, K. Hiramatsu, N. Sawaki, Selective growth of wurtzite GaN and $Al_xGa_{1-x}N$ on GaN/sapphire substrates by metalorganic vapor phase epitaxy, *Journal of Crystal Growth.* **144** (1994) 133-140.
36) J. Komiyama, Y. Abe, S. Suzuki, H. Nakanishi, Polarities of GaN films and 3C-SiC intermediate layers grown on (111) Si substrates by MOVPE, *Journal of Crystal Growth.* **298** (2007) 223-227.
37) A. Dadgar, M. Poschenrieder, J. Blasing, et. al., MOVPE growth of GaN on Si (111) substrates, *Journal of Crystal Growth*. **248** (2003) 556-562.
38) W. M. Yim, R. J. Paff, Thermal expansion of AlN, sapphire, and silicon, *Journal of Applied Physics.* **45** (1974) 1456-1457.
39) M. H. Lin, H. C. Wen, Y. R. Jeng, C. P. Chou, Nanoscratch characterization of GaN epilayers on c and a-axis sapphire substrates, *Nanoscale Research Letters.* **5** (2010) 1812.
40) E. Feltin, B. Beaumont, M. Laugt, P. de Mierry, P. Vennegues, H. Lahreche, M. Leroux, P. Gibart,

Stress control in GaN grown on silicon (111) by metalorganic vapor phase epitaxy, *Applied Physics Letters*. **79** (2001) 3230-3232.

41) H. Amano, N. Sawaki, I. Akasaki, Metalorganic vapor phase epitaxial growth of a high quality GaN film using an AlN buffer layer, *Applied Physics Letters*. **64** (1985) 1687 353-355.

42) P. Sohi, D. Martin, N. Grandjean, Critical thickness of GaN on AlN: impact of growth temperature and dislocation density, *Semiconductor Science and Technology*. **32** (2017) 075010.

43) G. Li, W. Wang, W. Yang, Y. Lin, H. Wang, Z. Lin, S. Zhou, GaN-based light-emitting diodes on various substrates: a critical review, *Reports on Progress in Physics.* **79** (2016) 056501.

Chapter 2

Plasma nanomanufacturing process

2.1 Introduction

As described in Chapter 1, there are several challenges in ultraprecision figuring and finishing of difficult-to-machine brittle functional materials. These are:

- Poor machinability due to their brittleness, high hardness, and chemical inertness.
- Difficulty to obtain a high-quality surface without damage and pits.
- Difficulty in achieving high processing efficiency, high processing quality and low processing cost at the same time.

Owing to its high processing efficiency, conventional mechanical manufacturing process using hard tools such as diamond is still widely used in the preliminary figuring and flattening process of difficult-to-machine brittle functional materials to quickly achieve the processing goal. However, due to the removal mechanism of conventional mechanical manufacturing process, the subsurface damage (SSD) layer is inevitably formed, and this affects the excellent properties of the material itself. The formation of an SSD layer can be effectively avoided, since no mechanical external force is applied to the surface of the substrate in the chemical manufacturing process compared to the physical manufacturing process. Due to the relatively high processing efficiency, chemical etching process is usually used to quickly remove the SSD layer which was generated during mechanical process. However, the flattening ability of chemical etching is poor owing that etching is an isotropic process. In recent years, many ultraprecision manufacturing processes that combine chemical modification and physical removal have been developed to achieve damage-free flattening and finishing. In this chapter, a variety of current figuring techniques and finishing techniques were introduced. Although these current manufacturing techniques have their own advantages, they also have their own disadvantages. Aiming at addressing the challenges of the current technology, a new manufacturing process for difficult-to-machine brittle functional materials was proposed. The plasma nanomanufacturing process, which consists of plasma chemical vaporization machining (PCVM) technique was proposed and developed for figuring with nanometer-order form accuracy and plasma-assisted polishing (PAP) for atomically smooth damage-free finishing.

2.2 Current figuring techniques

2.2.1 Ultraprecision cutting

Slow sliding servo (SSS) and fast tool servo (FTS) technology makes ultraprecision cutting become the most effective figuring method [1-4]. Figure 2.1 shows the conceptual diagram of an SSS diamond turning machine [4]. SSS is a type of turning method with T-shaped configuration, in which the Z-axis oscillates back and forth while X and C-axis maintain a constant speed [5]. The processing efficiency of the SSS is relatively low due to the low Z-axis moving speed but possesses a better processing accuracy. By optimizing the tool parameters such as tool nose radius, clearance, rake angles, etc. and other processing paths, the form accuracy in aluminum alloy materials can reach 0.5 μm profile valley (PV). FTS is a self-contained and independently operated positioning device, which was designed and built to eliminate the problem of low Z-axis moving speed by moving only the small mass of the tool itself [3]. The newly designed FTS can fabricate difficult-to-cut materials such as steel, brittle materials, and so on. Mizutani *et al.* employed an FTS with resolution of 5 nm in grinding machine to generate a ceramic mirror surface with the accuracy of ±0.01 μm [6]. Although the SSS and FTS technology made ultraprecision cutting to be widely used in the preliminary figuring of various materials, they still have limitations. At first, since ultraprecision cutting is a kind of contact manufacturing process, it is difficult to fabricate a shape with a large ratio of sag height to diameter due to tool interference. And then, due to the rotary processing method of diamond turning, the shape of the off axis is also difficult to be formed. Furthermore, due to ultraprecision cutting using high-hardness tools, such as diamond, an SSD layer, which affects the durability of the materials, will be formed on the surface. J. Yan *et al.* processed reaction-bonded silicon carbide by diamond turning. Although a surface roughness of 23 nm *R*a was obtained, scratches and damage layers were also formed on

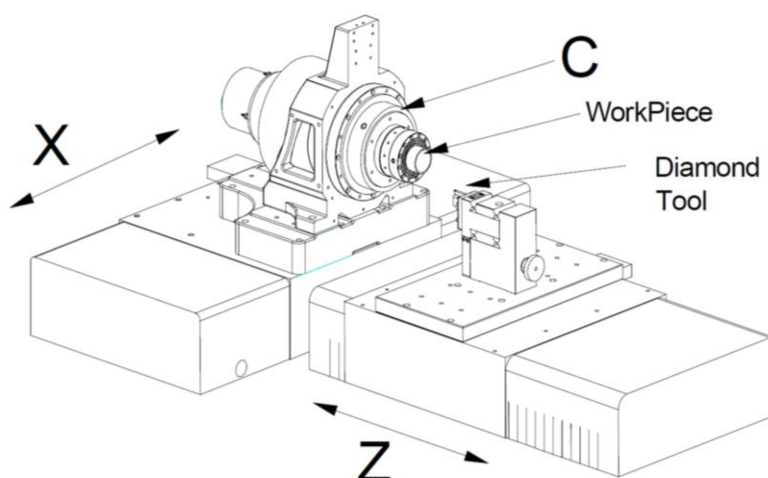

Figure 2.1 Conceptual diagram of SSS diamond turning machine.

the surface of reaction-bonded silicon carbide [7]. The above reasons all limit the application of ultraprecision cutting in the field of ultraprecision figuring for difficult-to-machine brittle functional materials.

2.2.2 Ion beam figuring

In ion beam figuring (IBF) process, the ion beam with a certain energy and spatial distribution is used to impact the substrate surface. It utilizes the physical sputtering occurred during the impact to remove the surface material and correct the surface shape error [8, 9]. In most cases Ar gas is fed to the ion source and thus Ar ions interact with the surface atoms [10]. Figure 2.2 shows the schematic of IBF. When the ions hit the substrate surface, they transfer their energy to the substrate atoms, and when the absorbed energy is greater than the lattice binding energy, the substrate atoms are displaced from their equilibrium positions and collide with surrounding atoms to generate new energy transfer. But when the obtained energy of the substrate atoms is less than the lattice binding energy, there will be no displacement, and the energy obtained will be released in the form of phonons [11]. Based on these principles, IBF process can theoretically achieve atomic-level material removal. Since IBF has high processing accuracy, and good repeatability, it is widely used in the final processing of optical components. Furthermore, IBF is a noncontact processing procedure, that do not require decrease in processing capacity due to tool wear.

IBF was first proposed by A. B. Menel *et al.* in 1965 [12]. Recently, after continuous development and optimization, IBF has become an established deterministic technique employed in high-end optics manufacturing for ultraprecision freeform surface figuring [13, 14]. P. Gailly *et al.* reported that the chemical vapor deposited silicon carbide (CVD-SiC) mirror-surface figure errors can be reduced from 243 nm to 13 nm rms by applying IBF [15]. However, the processing efficiency of IBF is very low, which also limits its wider application

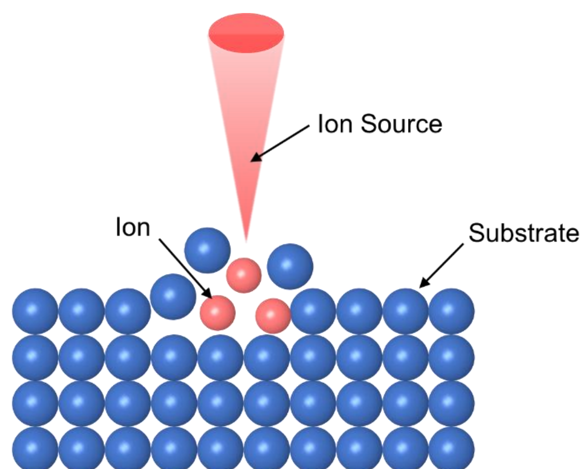

Figure 2.2 Schematic diagram of ion beam figuring.

2.2.3 Wet-etch figuring

As a noncontact figuring technique based on chemical etching, wet-etch figuring (WEF) was first proposed by M. C. Rushford *et al* [16,17]. Figure 2.3 shows the schematic of WEF. WEF utilizes free surface flow driven by surface tension gradients due to the Marangoni effect to fit and adjust the size and shape of an etchant droplet attached to the underside of a glass surface. The droplet, or wetted zone, is placed on the glass surface, leading to the etching of the surface, to facilitate an etching-based small-tool figuring process that is free of mechanical and thermal stresses. However, since the sample must be placed horizontally during WEF when processing both large and thin substrate, the substrate will sag and deform due to gravity. In addition, the absorbed etchant component, which vaporizes and diffuses from the nozzle, may cause undesirable roughening of the surface around the nozzle. In response to these problems, K. Yamamura *et al.* developed a numerically controlled local wet etching (NC-LWE), which uses a vacuum pump to forcefully suction-off the etchant with volatile component around the nozzle [18-20].

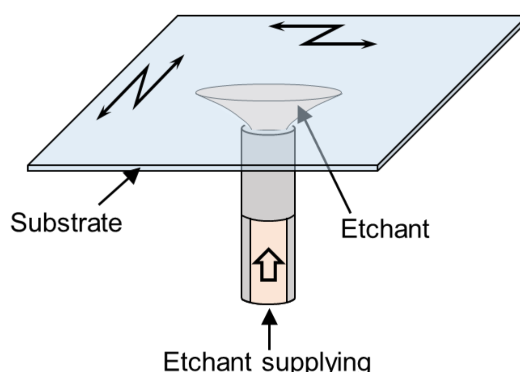

Figure 2.3 Schematic representation of wet-etch figuring.

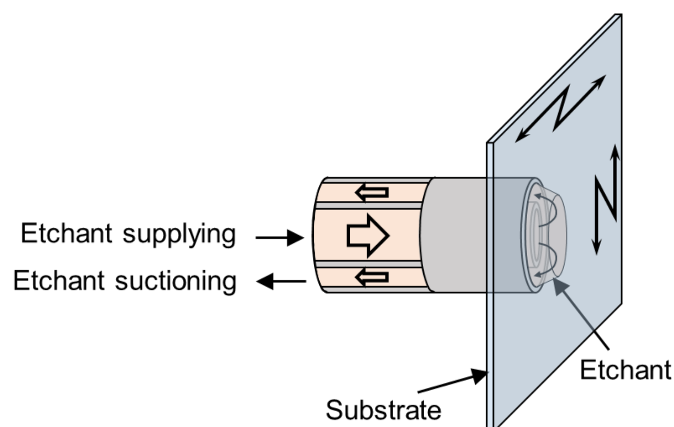

Figure 2.4 Schematic representation of numerically controlled local wet etching.

Figure 2.4 shows the schematic diagram of NC-LWE. The nozzle head consists of an etchant supply part and a suction part, which are arranged coaxially, and the removal area is limited to inner part of the suction slit. No etchant solution remains on the surface of a workpiece after the nozzle has passed, because both the amount of etchant supplied, and the suction of the etchant are properly balanced. The suctioning mechanism of the etchant supply nozzle enables free configuration of the nozzle direction and prevents unwanted surface roughening. K. Yamamura *et al.* verified that the maximum PV decreased from 192 nm to 56 nm for the measurement area of 142 mm × 142 mm for a single application of NC-LWE. The surface roughness was the same as before machining, and its value was less than 0.15 nm *S*q [18].

WEF and NC-LWE has been applied to figuring of quartz substrate, but has limitations since it can only be used to process materials chemically reactive with the etchants, such as quartz glass. Materials with strong chemical inertness, such as SiC, are difficult to process using WEF or NC-LWE.

2.3 Current polishing techniques

2.3.1 Chemical mechanical polishing

In the 1980s, chemical mechanical polishing (CMP) was first proposed at IBM to be combined with reactive ion etching, which was applied in the Shallow Trench Isolation (STI [21]) process which was used in 16 Mb DRAM technology [22, 23]. Different from conventional mechanical polishing, CMP combines chemical reaction and mechanical removal to minimize any surface damages. As a highly smooth polishing method, CMP is gradually being accepted for use in the

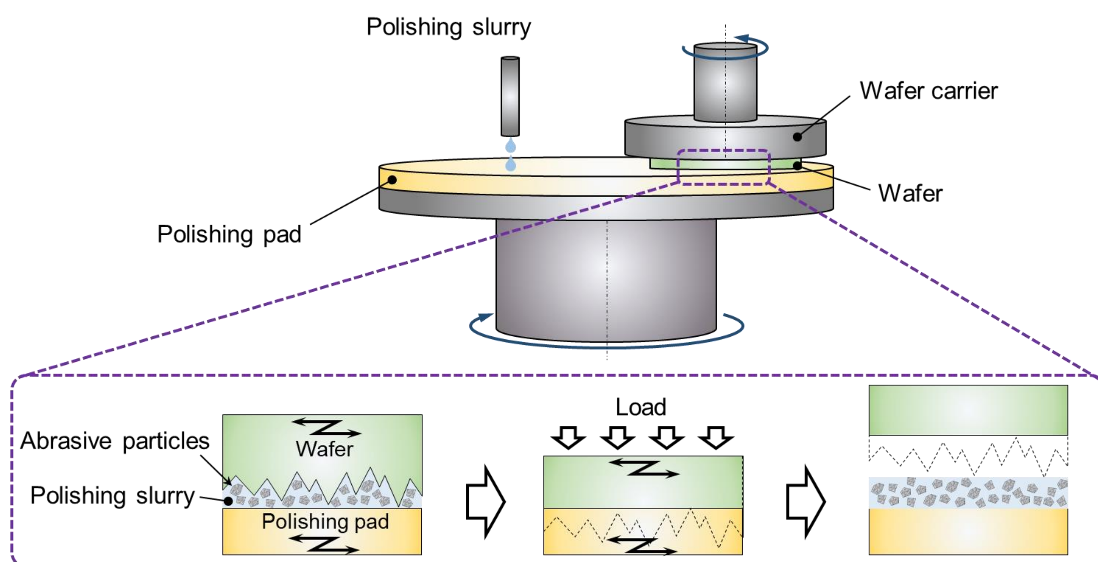

Figure 2.5 Schematic representation of a typical setup and polishing mechanism of CMP.

polishing of a variety of materials, such as semiconductors, metals, polymers, and composites materials [24, 25]. Figure 2.5 shows a schematic representation of a typical setup and polishing mechanism of CMP. The polishing slurry that plays an important role in CMP, generally contains abrasive particles (alumina, silica, and ceria were the most used [24, 26]), oxidant, and alkali (the pH of polishing slurry was adjusted between 8.5–11 using alkali) [25, 27]. During the CMP process, wafer was fixed on the wafer carrier and pressed face-down on the polishing pad to rotate it about its axis. At the same time, the polishing pad was covered by the polishing slurry and was also rotated about the other axis, and the polishing pressure was applied to the wafer through the wafer carrier. The oxidant and alkali in the polishing slurry chemically react with the substrate. A modified layer was generated on the surface of the wafer through the chemical reaction and was removed by abrasive particles with a certain material removal rate (MRR). After continuous development and parameter optimization, the MRR of Si wafer in CMP can reach higher than 10 μm/h, which allows CMP to become an industrially applicable finishing technique for Si wafers [28, 29].

Since SiC has a wider band gap, higher thermal conductivity, and some other excellent properties more than Si, SiC is considered to be the next generation semiconductor material used in high temperature and high power conditions instead of Si [30, 31]. As a promising polishing technology, CMP was to be applied for the finishing of SiC. A lot of research has been carried out on CMP of SiC in recent years [27, 32, 33]. In the CMP of SiC, an alkaline colloidal silica slurry is widely used [27, 33]. The surface of SiC is oxidized into SiO_2, and then removed by silica abrasive, whose Vickers hardness is smaller than that of SiC, and thus there was no SSD layer generated. Y. Zhou *et al.* obtained a surface roughness less than 0.05 nm *S*a for CMP of SiC [34]. However, the oxidation rate of SiC in CMP is very slow due to its strong chemical inertness, which causes the MRR of SiC in CMP (less than 200 nm/h in Ref. 34) to be far lesser than that of Si. G. Pan *et al.* and S. Kurokawa *et al.* proved that the addition of potassium permanganate ($KMnO_4$) and hydrogen peroxide (H_2O_2) into the polishing slurry can effectively increase the oxidation rate of SiC, thereby increasing the MRR [27, 35]. In addition, a mixed abrasive slurry consisting of colloidal silica and nano-diamond has also been developed [36]. The diamond abrasive forms mechanical stress at the surface of SiC and increases the surface modification rate, resulting in an increase in the MRR from 0.06 μm/h to 0.55 μm/h. V. D. Heydemann *et al.* reported that the addition of 0.1 μm diamond abrasive and sodium hypochlorite oxidizer to the colloidal silica slurry resulted in an MRR increase to 0.92 μm/h and produced substrates with an *S*a surface roughness of 0.52 nm [37].

Besides the low MRR, large particles can easily be formed by the agglomeration of the abrasive particles in slurry when it is placed for a long time. These agglomerated particles are the cause of the formation of scratches and SSD layer during CMP processes [38]. More so, since most of the

polishing slurry is alkaline, the used polishing slurry must undergo a series of tedious treatments such as neutralization before being discharged, which greatly increases the cost and environmental burden. The huge cost due to the management and disposal of the used slurry also limits the actual industrial application of CMP.

2.3.2 Catalyst-referred etching

As described in the previous section, an SSD layer was formed easily on the surface of the substrate when mechanical polishing method was applied. Chemical etching method is an effective way of removing the SSD layer. However, it is difficult to obtain a flat surface due to the isotropy of the chemical etching method. Although CMP combines chemical reaction and mechanical removal, the surface waviness of the processed substrate also increases during the processing because of the elastically soft polishing pad that was used in CMP. To obtain a wafer surface with high flatness and without SSD layer, Hara *et al.* developed an abrasive-free planarization method called catalyst-referred etching (CARE) [39-41]. Figure 2.6 shows a schematic diagram of a typical setup and polishing mechanism of CARE. In the case of SiC wafer processing, the wafer was immersed in hydrofluoric acid (HF) solution. HF can etch materials such as SiO_2 but cannot react with SiC. The flat plate made of catalyst material such as Pt, which can provide a reference plane for the polishing process, was also immersed in HF solution. The catalyst generated reactive species that were activated only next to the catalyst surface and were deactivated when exiting the surface. Only the raised positions on the wafer surface generate oxide films due to catalytic reaction, and are then etched by HF and removed from the surface [39]. The locations that were not in contact with the catalyst plate will not be etched. As the processing

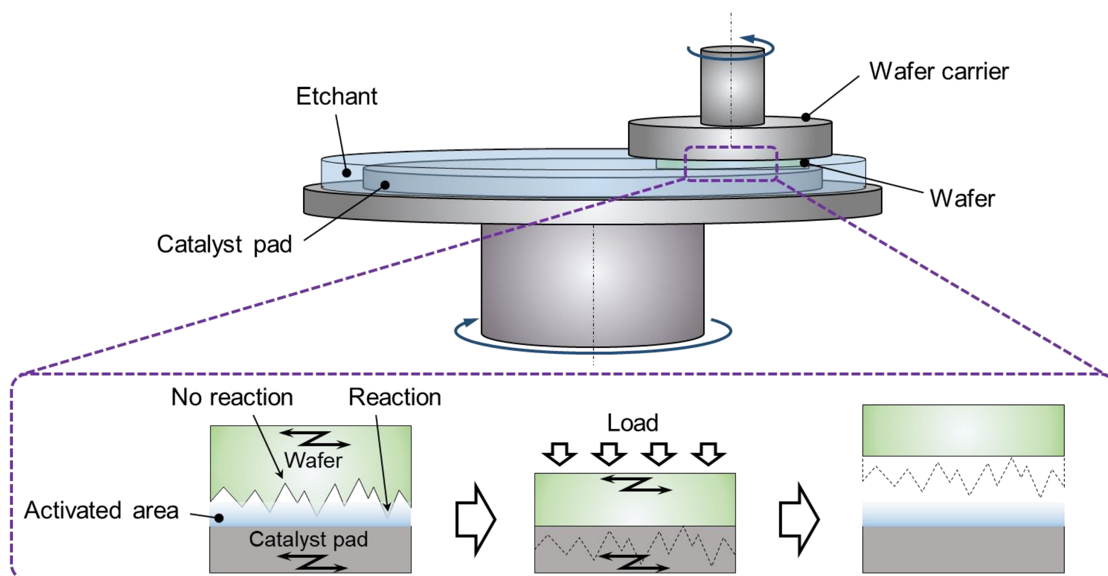

Figure 2.6 Schematic representation of a typical setup and polishing mechanism of CARE.

time increases, a damage-free SiC surface with high flatness could be obtained. The MRR of CARE is proportional to the atomic step density because CARE proceeds only at step edge because of the step-flow etching phenomenon [42]. Although a surface roughness less than 0.1nm *S*a can be obtained through CARE, the MRR was only approximately ~10 nm/h for on-axis SiC wafer, and ~100 nm/h for 4°-off SiC wafer [43, 44]. To improve the MRR of CARE, Toh *et al.* proposed to irradiate the surface of SiC wafer by UV light to improve the oxidation rate of SiC, and the MRR of the 4°-off SiC wafer was increased to about 190 nm/h [45]. In 2015, the mechanism of platinum-assisted hydrofluoric acid etching of SiC was clarified by P. V. Bui *et al.* using density functional theory calculations [46], and the OH^- is considered to play the same role as F^- in CARE [47]. Isohashi *et al.* and P. V. Bui *et al.* proposed water-CARE using pure water instead of HF solution to make CARE more practically applicable and environment-friendly [47,48]. But low MRR of CARE remains a challenge that needs to be solved.

2.3.3 Ultraviolet-assisted polishing

As an ultraprecision polishing method, Ultraviolet (UV)-assisted polishing was proposed to polish SiC substrate by J. Watanabe *et al.* [49]. Figure 2.7 shows a schematic diagram of a typical setup and polishing mechanism of UV-assisted polishing. In their research, a quartz disk was

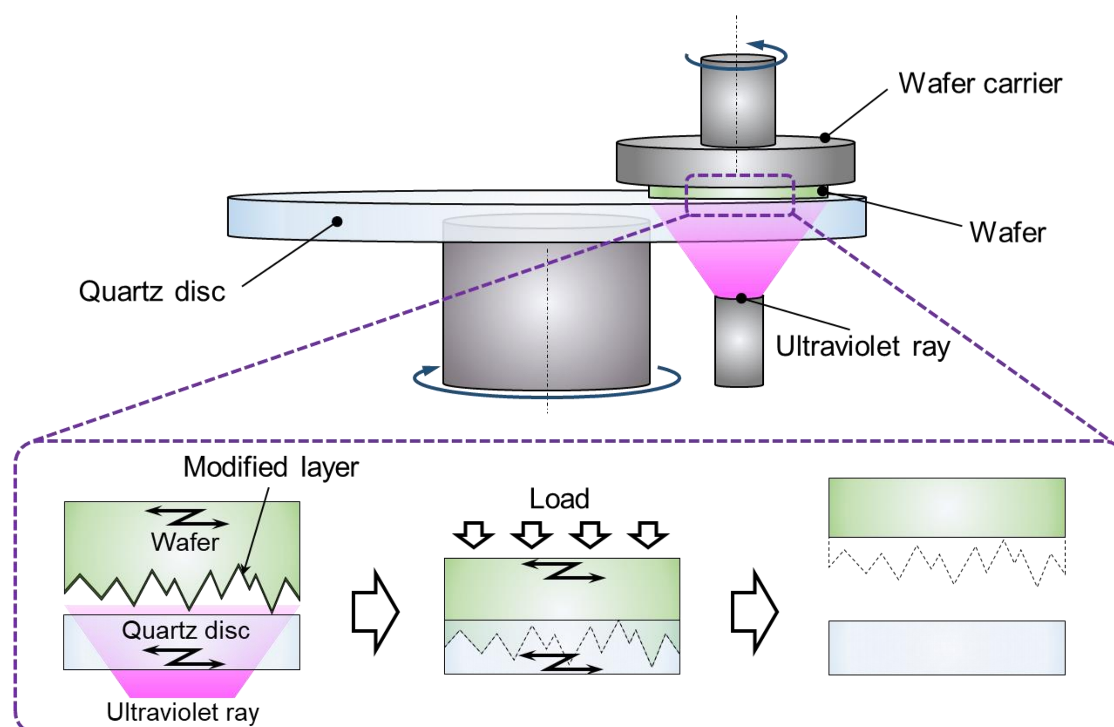

Figure 2.7 Schematic representation of a typical setup and polishing mechanism of UV-assisted polishing.

applied for the polishing of SiC substrate. The ultraviolet ray penetrated through the quartz disk and irradiated directly to the polishing area. SiC has a band gap energy of 3.26 eV and thus can be excited by UV irradiation with a wavelength shorter than 380 nm [50)]. Holes and electron pairs can be generated by photoexcitation under UV irradiation and can bond immediately with oxygen and water molecules in the atmosphere. The bonding reactions generate many atomic oxygens and OH radicals, which are highly active species with high oxidation potentials, and result in the oxidation of the topmost surface of SiC [51,52)]. Since SiC substrate was contacted with the quartz disc directly, the increased temperature induced by the rubbing in the mechanical-chemical polishing between SiC substrate and quartz disc could also contribute to the oxidation reaction [53)]. Finally, the oxide layer on SiC substrate was removed by quartz glass and a surface roughness of less than 0.5 nm *S*a for a 4°-off SiC substrate was obtained. The MRR was proven to have improved from 0.86 μm/h to 1.487 μm/h under an O_2 atmosphere instead of air [50)]. In recent years, UV-assisted polishing has also been successfully applied to the polishing of diamond and its related materials. A surface roughness of 2.7 nm *S*a for polycrystalline diamond (PCD) [53)], and a surface roughness of less than 0.2 nm *S*a for single-crystal diamond (SCD) [54, 55)] was obtained.

2.3.4 Electrochemical mechanical polishing

Electrochemical Mechanical Polishing (ECMP), which combines surface anodic oxidation and mechanical polishing, has been proposed for the highly efficient polishing of copper [56, 57)], stainless steel [58)], NiP substrate of hard disks [59)] and so forth. In 2004, a two-step ECMP was firstly applied to a single-crystal SiC by Li *et al.* [60)]. In their study, a 4H-SiC substrate was first oxidized by a mixture of H_2O_2 and KNO_3 electrolytes, then the oxide layer was removed by polishing using colloidal silica slurry. After several cycles of anodic oxidation and slurry polishing, a smooth surface with surface roughness of 0.27 nm *S*q was obtained. However, as mentioned in section 2.3.1, the use of slurry led to many problems such as high cost and agglomeration of the abrasive particles. Therefore, a slurry less ECMP process for N-type SiC substrate was proposed by X. Yang *et al.* [61, 62)]. Figure 2.8 shows a schematic representation of a setup and polishing mechanism of slurry less ECMP. SiC wafer was fixed on a wafer carrier and pressed face-down on the grinding stone. The grinding stone was placed on a metal plate with many fan-shaped openings. The SiC wafer, grinding stone, and metal plate were immersed in an electrolyte, and the wafer holder, SiC surface, electrolyte, and metal plate formed an electric circuit. SiC surfaces can be anodically oxidized by the applied positive potential, and the oxidation rate can be adjusted by controlling the potential. Subsequently, the modified layer is removed by the grinding stone and a smooth surface can be obtained. X. Yang *et al.* proposed a three-step N-type SiC wafer manufacturing process using slurry less ECMP. At the first step, after the slurry less ECMP for 20

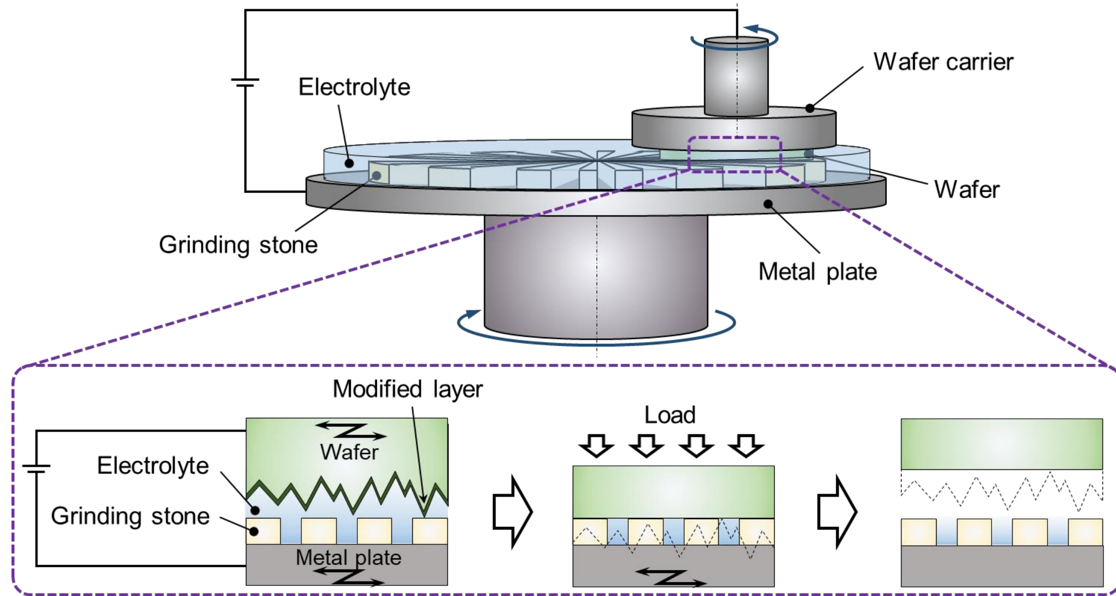

Figure 2.8 Schematic representation of a typical setup and polishing mechanism of slurry less ECMP.

min, at a current density of 20 mA/cm^2 in sodium chloride aqueous solution (NaCl aq.) using a #8000 diamond vitrified grinding stone, the *S*q surface roughness decreased from 163.33 to 25.45 nm with an MRR of 62 µm/h. At the second step, after the slurry less ECMP for 30 min, at a current density of 10 mA/cm^2 in NaCl aq. using a #8000 ceria vitrified grinding stone, the *S*q surface roughness further decreased to 0.82 nm with a MRR of 11 µm/h. Finally, at the third step, after the slurry less ECMP for 60 min, at a passivation potential (3V) in NaCl aq. using a #8000 ceria vitrified grinding stone, a scratch-free atomically smooth surface with a *S*q surface roughness of 0.11 nm was obtained. Slurry less ECMP was considered an excellent processing method for N-type SiC wafer due to its high MRR and high polishing quality. However, due to the processing mechanism, ECMP can only be applied to process conductive materials, but cannot be used to process insulating materials such as semiinsulating SiC, ceramics and so forth.

2.3.5 Magnetorheological finishing

Magnetorheological finishing (MRF) was firstly proposed by W. I. Kordonski *et al.* [64)]. The principle of this technique lies in the fact that conditions for successful noncontact polishing are created and controlled by utilizing the state of flow of an MR polishing fluid in a magnetic field [65)]. Figure 2.9 shows a schematic representation of a setup and polishing mechanism of MRF. The MR polishing fluid, which consists of abrasive particles, magnetic particles, and water, plays an important role in MRF. As shown in Fig. 2.9, the MR polishing fluid is continuously applied to a rotating wheel via a nozzle. Below the wheel surface is an electromagnet for generating a

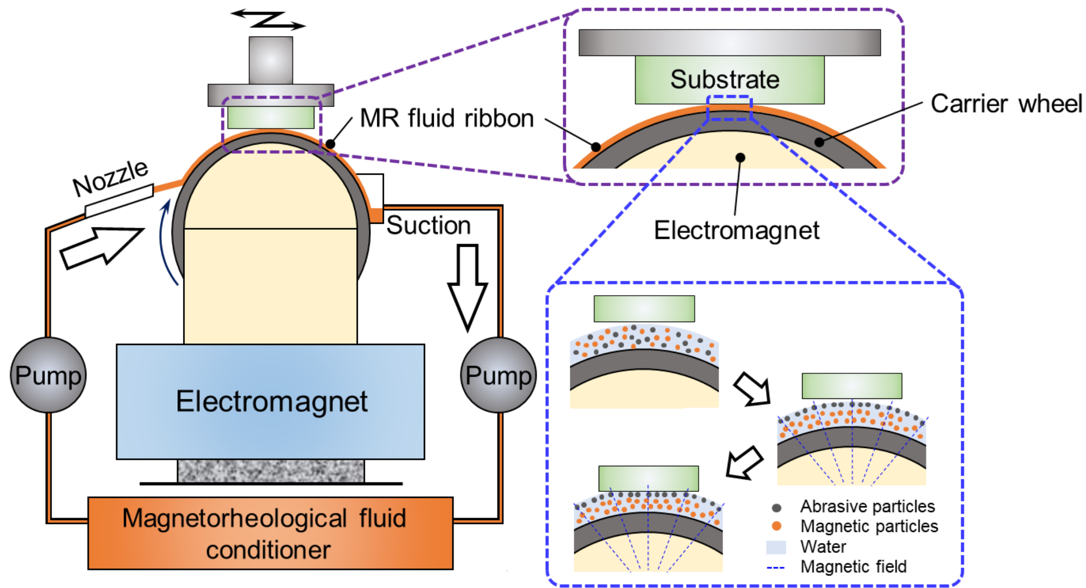

Figure 2.9 Schematic representation of a typical setup and polishing mechanism of MRF.

magnetic field that changes the viscosity of MR polishing fluid. The magnetic field gradient is normal to the top of the carrier wheel and the magnetic field force lines penetrate the gap between the wheel and the part surface of substrate in the direction that is perpendicular to the direction of the wheel motion. The MR polishing fluid is delivered to the wall in the vicinity of the electromagnet. Magnetic particles are pressed by the magnetic field gradient against the wall and acquires the wall velocity and becomes a plastic Bingham medium [66)] before it enters the gap between wheel and the substrate. Abrasive particles are separated from the MR polishing fluid due to nonmagnetic repulsion by the magnetic field and are embedded in the surface layer of the MF polishing fluid. Thereafter, a shear flow of plastic MR polishing fluid occurs through the gap resulting in material removal from the surface of substrate [65, 67)]. As a well-developed polishing technique, MRF has been applied to the finishing of quartz glass [68)], silicon substrate [69)], titanium [70)] and so forth. H. Cheng *et al.* also applied MRF to reaction-bonded SiC for the processing of an aspheric mirror [71)]. They confirmed that the surface roughness with an initial value of 26.74 nm *S*a reached 1.14 nm *S*a after 50 hours of using oil host MR polishing fluid and a nonmagnetic diamond powder. However, the limitation of the MRR of MRF is the small working area of the stiffened MR polishing fluid ribbon.

2.4 Plasma nanomanufacturing process proposal

2.4.1 Introduction

The above-introduced figuring and polishing techniques have shown their respective

advantages in different application fields. However, for difficult-to-machine brittle functional materials with brittleness, high hardness, and chemical inertness, the above-introduced processing methods also have their own limitations. For example, it is difficult to maintain high MRR while ensuring high-quality polishing. Furthermore, due to the different properties of different components, it is difficult to obtain an ultrasmooth surface of a multicomponent material. The use of polishing slurry usually leads to an increase in processing costs and has been reported that the use, management, and posttreatment of slurry account for about 50% of the total cost of CMP [72). Therefore, the dry polishing method that does not use polishing slurry is an advantageous choice for reducing processing costs.

As an efficient processing method, conventional mechanical manufacturing process is still the first choice for primary processing. However, for finishing, how to quickly remove the SSD layer formed during the conventional mechanical manufacturing process and to complete the final polishing without complicated process conversion is a challenge in the field of ultraprecision machining. Owing to the different processing requirements of different difficult-to-machine brittle functional materials, plasma nanomanufacturing process, which combines PCVM [73) for figuring without forming SSD layer and PAP [74) for obtaining an atomically smooth surface, was proposed and developed in this study.

2.4.2 Basics of plasma for processes

Plasma, which is often called the fourth state of matter, along with solid, liquid and gas, has unique physical and scientific properties. The kinetic energy of its particles is large due to high temperature. It conductive because of its group of charged particles and is chemically active and highly reactive. Because of its light emitting nature, plasma can be used as a light source. As a processing tool, the large kinetic energy and high reactivity of plasma are mainly utilized in plasma processing.

2.4.2.1 Collision between electrons and molecules/atoms in plasma

The properties of electrons and molecules/atoms in plasma can be determined from the collision between electrons in the plasma and gas molecules/atoms. Considering the case where the electron, e^-, collides with the molecule XY with a small collision energy, the product is an elastic collision, and the kinetic energy of the electron hardly changes. However, when the collision energy becomes higher, the orbital electrons orbiting around the nucleus in the molecule receive energy at the time of collision and orbit the large energy level above (excitation).

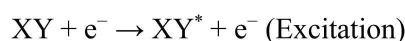

$$XY + e^- \rightarrow XY^* + e^- \text{ (Excitation)}$$

Molecules in such a high-energy state are called excited molecules and are represented by XY^*.

The electrons in the orbit of the excited state fall back into the orbit of the lower energy level in a short time, so that the excess energy is emitted as photon.

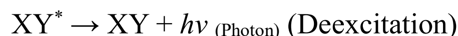

$$XY^* \rightarrow XY + h\nu_{\text{(Photon)}} \text{ (Deexcitation)}$$

On the other hand, when the energy of the colliding electron becomes much higher, the electron e^- in the molecule is emitted and ionization occurs (ionization).

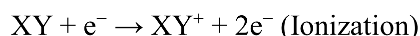

$$XY + e^- \rightarrow XY^+ + 2e^- \text{ (Ionization)}$$

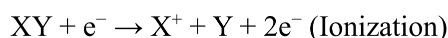

$$XY + e^- \rightarrow X^+ + Y + 2e^- \text{ (Ionization)}$$

However, the bond of the molecule XY may be broken and dissociated into X and Y (dissociation).

$$X{:}Y + e^- \rightarrow X\cdot + Y\cdot + e^- \text{ (Dissociation)}$$

When the electron pair involved in the bond is represented by ":", the dissociation can be written as given in the equation above. Since X・ and Y・ have unpaired electrons, they are likely to cause a chemical reaction and thus, are called radicals. They are also called a neutral radical because they do not have electric charges. The existence of many radicals with high kinetic energy is considered to be the reason for the strong reactivity of the plasma [75].

2.4.2.2 Spectroscopic measurements of plasma emission light

Along with the collision between electrons and gas molecules in the plasma, the excitation and deexcitation of electrons around the gas molecules occur continuously. When the electron falls back from the excited state to the ground state, the excess energy is emitted as photons. Since the released energy is related to the inherent properties of each atom or molecule, the properties of the plasma can be analyzed by measuring the emitted light of the plasma [76-78]. The visible range is only a very small part between 380 to 780 nm. However, common extensions are possible for the ultraviolet and the infrared, resulting roughly in a range from 200 nm to 1 μm. Experimentally, this wavelength region is the first choice in plasma spectroscopy. Since air is transparent, quartz windows can be used, and a variety of detectors and light sources are available. Below 200 nm, quartz glass is no longer transparent and the oxygen in the air starts to absorb light resulting in the need for an evacuated light path. Above 1 μm the thermal background noise becomes stronger which can only be compensated for using expensive detection equipment. The emission spectrum in the visible range can be easily obtained by a very simple and reliable experimental device. The method itself is noninvasive, which means that the plasma is not affected. In addition, the recording of spectra is not disturbed by the presence of radio frequency fields, magnetic fields, high potentials, etc. The experimental setup is very simple and requires only a diagnostic port through the line of sight of the plasma. Therefore, plasma spectroscopy is an established

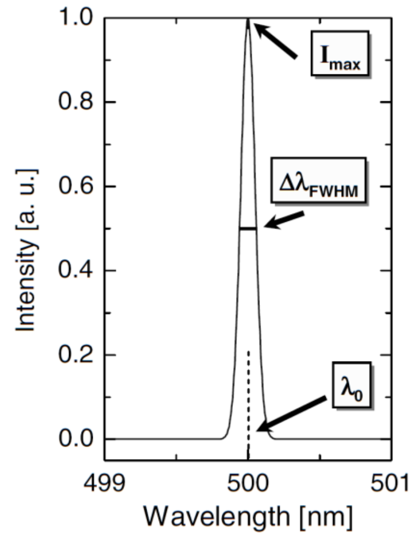

Figure 2.10 Line radiation and its characteristics [79].

diagnostic technique in plasma processing and technology and basic research [79].

In general, plasma spectroscopy is subdivided into two types of measurements: the passive method of emission spectroscopy (Analyze by measuring the energy emitted in deexcitation process) and the active method of absorption spectroscopy (Analyze by measuring the energy absorbed in excitation process). However, absorption techniques need much more experimental effort than emission spectroscopy. Since some principles of emission spectroscopy apply also to absorption and, since emission spectroscopy provides a variety of plasma parameters and is a passive and very convenient diagnostic tool, emission spectroscopy is more widely used [79].

In the case of emission spectroscopy, light emitted from the plasma itself is recorded. Here one of the basic underlying processes is the excitation of particles (atoms, molecules, ions) by electron impact from level q to level p and the decay into level k by spontaneous emission, with the transition probability A_{pk} resulting in line emission $\varepsilon_{\mathrm{pk}}$. The two axes of a spectrum are the wavelength axis and the intensity axis as shown in Fig. 2.10. The central wavelength of line emission λ_0 is given by the photon energy $E = E_{\mathrm{p}}–E_{\mathrm{k}}$ corresponding to the energy gap of the transition from level p with energy E_{p} to the energetically lower-level k. Here, Planck constant is h, and speed of light is c:

$$\lambda_0 = \frac{hc}{E_{\mathrm{P}} - E_{\mathrm{k}}} \tag{2-1}$$

Since the energy of transition is characteristic of the particle species, the central wavelength is an identifier for the radiating particle, unless the wavelength is shifted by the Doppler effect. As a principle, the wavelength axis λ is easy to measure, to calibrate and to analyze. This changes to

the opposite for the intensity axis. The line intensity is quantified by the line emission coefficient:

$$\varepsilon_{\mathrm{pk}} = n(p) A_{\mathrm{pk}} \frac{hc}{4\pi\lambda_0} = \int_{line} \varepsilon_\lambda \, d\lambda \tag{2-2}$$

The unit is given as W $(m^2sr)^{-1}$, where 4π represents the solid angle $d\Omega$ (isotropic radiation), measured in steradian (sr). The line profile P_λ correlates the line emission coefficient with the spectral line emission coefficient ε_λ:

$$\varepsilon_\lambda = \varepsilon_{\mathrm{pk}} P_\lambda \quad \text{with} \quad \int_{line} P_\lambda \, d\lambda = 1 \tag{2-3}$$

A characteristic of the line profile is the full width at half maximum (FWHM) of the intensity, $\Delta\lambda_{\mathrm{FWHM}}$, as indicated in Fig. 2.10. The line profile depends on the broadening mechanisms [77]. In the case of Doppler broadening, the profile assumes a Gaussian curve, and the line width correlates with the particle temperature. A convenient alternative to the line emission coefficient is the absolute line intensity in units of photos $(m^3s)^{-1}$:

$$I_{\mathrm{pk}} = n(p) A_{\mathrm{pk}} \tag{2-4}$$

This relationship reveals that the line intensity depends only on the population density of the excited level $n(p)$ which, in turn, depends strongly on the plasma parameters $n(p) = f\,(T_e, n_e, T_n, n_n, \ldots)$.

2.4.2.3 Difference between atmospheric-pressure plasma and vacuum plasma

Mean free path, which is used to define the average traveled distance of a particle between two collisions with other particles, is a very important physical quantity in plasma physics. As shown in Fig. 2.11, particle A with a radius of R_1, collides with a stationary particle B, with a radius of R_2 at a certain speed. When particle B enters the zone with the center of particle A as the center and R_1+R_2 as the radius, it is considered that particle A is sure to collide with particle B. The cross-sectional area of this zone is called the effective collision area S [80]:

$$S = \pi(R_1 + R_2)^2 \tag{2-5}$$

When particle A moves linearly at speed v for a period t, and all particles B, contained in the effective volume (cylinder) which are affected by the effective collision area S are considered to collide with particle A. And the number of collisions can be estimated from the number of particle B that were in that volume. According to the definition, mean free path λ_{mfp} can be taken as the length of the path divided by the number of collisions:

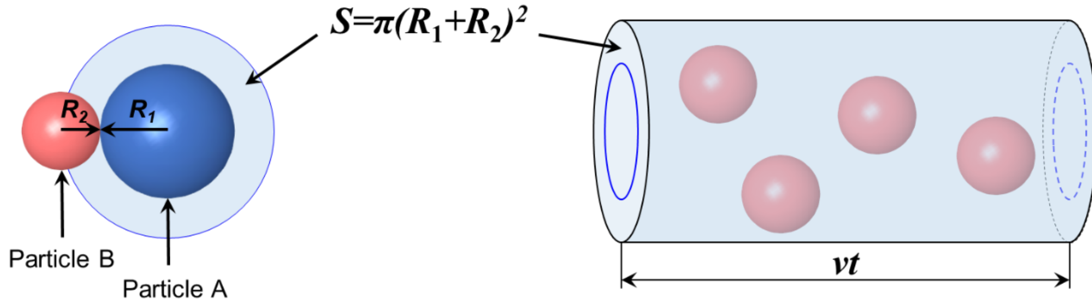

Figure 2.11 Model for solving mean free path.

$$\lambda_{\mathrm{mfp}} = \frac{vt}{\pi(R_1 + R_2)^2 vtn_V} = \frac{1}{\pi(R_1 + R_2)^2 n_V} \tag{2-6}$$

where the n_V is the number of particles B per unit volume. The expression of the mean free path above expression suffers from a significant flaw - it assumes that the B particles are at rest when in fact they are also moving. The frequency of collisions depends upon the average relative velocity of the randomly moving particles. The magnitude of the relative velocity can be expressed as the square root of the scalar product of the velocity with itself. If assume that the particles in the plasma are all moving at the same speed, the average relative velocity v_{rel} can be written as:

$$v_{\mathrm{rel}} = \sqrt{2}v \tag{2-7}$$

therefore, the effective volume V of swept out in time t becomes to:

$$V = \pi(R_1 + R_2)^2\sqrt{2}vt \tag{2-8}$$

The number of particles B per unit volume n_V can be determined from Avogadro constant N_A and the ideal gas law, leading to:

$$n_{\mathrm{V}} = \frac{nN_{\mathrm{A}}}{V} = \frac{nN_{\mathrm{A}}}{\frac{nRT}{P}} = \frac{N_{\mathrm{A}}P}{RT} \tag{2-9}$$

where P, V, T are the pressure, volume, and temperature respectively, and R is the ideal gas constant. The resulting mean free path λ_{mfp} is:

$$\lambda_{\mathrm{mfp}} = \frac{RT}{\sqrt{2}\pi(R_1 + R_2)^2 N_{\mathrm{A}}P} \tag{2-10}$$

The mean free path λ_{mfp} of particles is inversely proportional to gas pressure [81]. That means, the mean free path of particles in vacuum plasma is larger than that in atmospheric-pressure plasma.

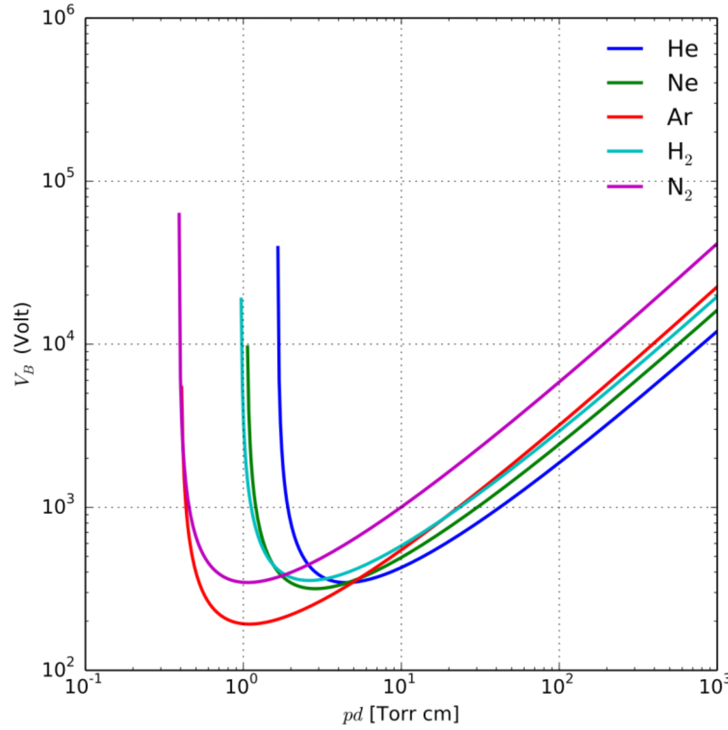

Figure 2.12 Paschen curves obtained for different gas [83].

As a typical way of plasma generation, in capacitively coupled plasma, conditions for breakdown at different gas pressures were first studied by Paschen *et al.* [82]. The result is the well-known Paschen curve describing the dependence of the breakdown voltage V_B on the distance d between electrodes and the gas pressure P (Fig. 2.12). Based on the Townsend criterion, the Paschen equation can be written as follow:

$$V_B = \frac{BPd}{ln(APd) - ln\left[ln\left(1 + \frac{1}{\gamma}\right)\right]} \tag{2-11}$$

where γ is the secondary-electron-emission coefficient, and A and B are constants dependent on the type of gas. The Paschen curve can be explained thus: in a discharge system in which the electrode distance (d) is constant, an increase in pressure (p) leads to a small mean free path and electrons cannot acquire sufficient energy to ionize. Thus, plasma generates easier in a relatively lower gas pressure. In addition, as the gas pressure increases, the number of gas molecules also increases, and the frequency of collisions between molecules increases. High-frequency molecular collisions increase the possibility of arc discharge, which will cause damage to the surface of the substrate due to its huge electric current density. Therefore, as a processing tool, when it is desired to use high-density radicals for figuring with high accuracy, atmospheric-pressure plasma is generally selected, and when it is desired to generate a large area stable plasma

to simultaneously irradiate a large size substrate to improve the modification efficiency, vacuum plasma is the better choice.

2.4.3 Plasma chemical vaporization machining (PCVM)

Plasma-assisted etching technique using radicals, which are more chemically reactive than most molecules, was proposed in 1960s and applied to etch solid [84, 85]. Till date, plasma-assisted etching has been widely used in the semiconductor industry. In conventional low-pressure plasma processing, the material is etched by the reaction with chemically active radicals formed in a glow discharge, and the entire surface of the sample is exposed to the plasma and the solid to be etched form volatile products [86-88]. In the application of pattern definition in IC fabrication, the etching of a photoresist mask layer on underlying layers is necessary. The material to be removed must be etched significantly faster than the underlying material. The underlying layer serves as a partial etch stop so that the etching layer can be etched uniformly [89-92]. However, the use of photoresist mask not only complicates the process, but also increases the cost. In 1993, Y. Mori *et al.* proposed the atmospheric-pressure plasma chemical vaporization machining (AP-PCVM) [73]. Since AP-PCVM is a noncontact chemical figuring technique that does not require a mechanical load on the substrates, an SSD layer is not formed during the removal process. A similar machining process has already been utilized in plasma etching in LSI manufacturing [89]. However, the removal rate was very low since it was carried out under a low-AP. In contrast, a high removal rate (larger than 200 μm/min for Si) and high machining resolution of 200 μm was achieved by generating reactive radicals of high density and high-pressure plasma in AP-PCVM [73]. A surface

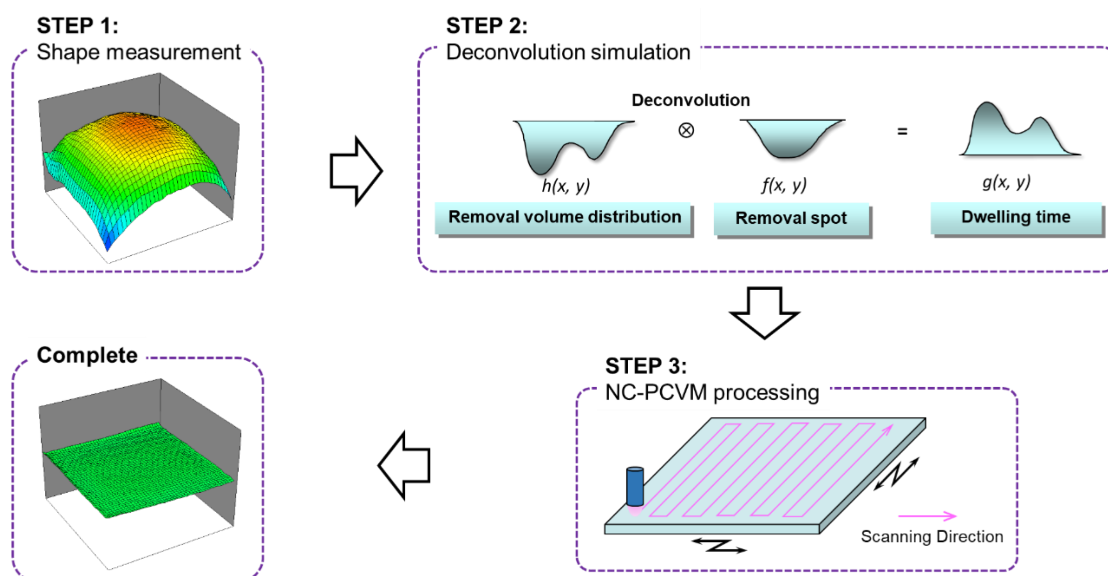

Figure 2.13 Processing theory of figure correction by AP-PCVM.

roughness of 0.5 nm for Si was also obtained. Since local dry chemical etching is performed in AP-PCVM instead of full-surface etching. Thus, AP-PCVM can achieve local processing without modifying the other locations and plasma-etch-resistant masks were not necessary. Figure 2.13 shows the processing theory of figure correction by AP-PCVM. Before AP-PCVM process, the initial surface shape of substrate is measured, and the initial shape data is used in the step 2 of the deconvolution calculation. On the other hand, the volumetric distribution of the footprint formed in a unit removal time is expressed by the "removal spot" data. It has been confirmed that the removal volume of the footprint is proportional to the removal time. Therefore, the local removal volume at a certain position can be controlled by controlling the dwelling time of the plasma during scanning. the dwelling time distribution of plasma can be obtained through the deconvolution simulation using the initial shape data and removal spot data. NC scanning is performed by raster scanning controlled by the dwelling time distribution data and AP-PCVM enables the plasma figuring of freeform surfaces without a mask. In recent years, AP-PCVM has been widely used for the figuring of X-ray mirrors made of Si [93)], thinning of 6-inch silicon-on-insulator substrate [94, 95)], and the thickness correction of quartz crystal wafers [96)]. Nanometer-order shape accuracy and thickness uniformity have also been achieved. Although AP-PCVM has been successfully applied for the figuring of single-component materials, there have been no reports of its application to multicomponent materials.

2.4.4 Plasma-assisted polishing (PAP)

Plasma-assisted polishing (PAP), which combines surface modification by plasma irradiation and removal of the modified layer by ultralow polishing pressure or using a soft abrasive, was proposed by K. Yamamura *et al.* in 2011 [74)]. Figure 2.14 shows a schematic diagram of a setup and polishing mechanism of PAP. Since PAP is a dry polishing technique that does not use polishing slurry, the processing cost can be greatly reduced rather than CMP. Furthermore, a soft abrasive with an intermediate hardness between the modified layer and the base substrate material or an ultralow polishing pressure is used in PAP, therefore a damage-free surface can be obtained. As a new polishing technology that combines chemical modification and physical removal, PAP has broken the limits of traditional mechanical processing and been successfully applied to many single crystal difficult-to-machine materials [74, 97-99)]. For single-crystal SiC, after the irradiation of water-vapor plasma, the average hardness of SiC was reduced from 37.4 GPa to 4.5 GPa due to an oxide layer was formed on SiC substrate surface. Through the subsequent polishing using CeO_2 polishing film, an atomically smooth SiC surface with a step and terrace structure without subsurface damage was obtained (0.14 nm *S*q) [74)]. For single-crystal GaN, CF_4 plasma irradiation was confirmed very efficient to soften the surface of GaN, and the modified layer (GaF_3) was removed by polishing using a resin-bonded CeO_2 grinding stone. Finally, a scratch-free and pit-

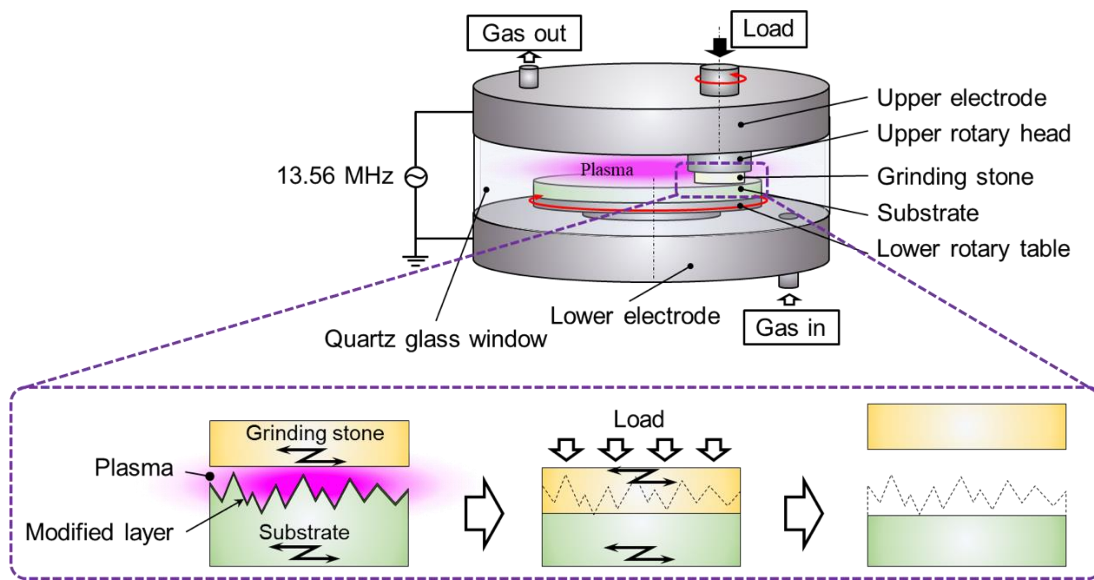

Figure 2.14 Schematic diagram of a typical setup and polishing mechanism of PAP.

free surface with a well-ordered step-terrace structure was obtained (0.08 nm *S*q) [98]. In addition, by applying PAP to a single-crystal diamond wafer, a MRR of 2.1 μm/h that was 20 times greater than that without plasma irradiation, was also obtained [99].

2.4.5 Strategies of plasma nanomanufacturing process

PCVM has been developed for nearly 30 years and has been widely used in a variety of single-crystal materials in industry application. However, PCVM is a processing technique based on pure chemical reaction, since the reaction characteristics of different composition components for plasma is different, it is difficult to obtain a smooth surface for multicomponent materials by PCVM. In addition, plasma etching is an isotropic processing process. Although a raster scanning processing was performed instead of full-surface etching in PCVM, the low spatial frequency roughness (LSFR) components of the substrate can be successfully removed by controlling the dwelling time, but the mid spatial frequency roughness (MSFR) and high spatial frequency roughness (HSFR) components are still difficult to be removed, owing that the spatial wavelength is shorter than the that of the plasma tool. Therefore, PCVM has so far been regarded as a figuring technique rather than a finishing technique, owing that it can efficiently remove the SSD layer formed in the conventional mechanical process and creates a low spatial frequency shape without damage. The positioning of PAP is a finishing technique that can obtain atomically smooth surfaces without damage. Different from PCVM, since the surface of grinding stone provide a reference surface in PAP, LSFR, MSFR, and HSFR can all be effectively removed through PAP. As introduced in 2.4.4, PAP has been successfully applied to a variety of difficult-to-process materials with excellent results. But the relatively low MRR is a shortcoming of PAP. It is

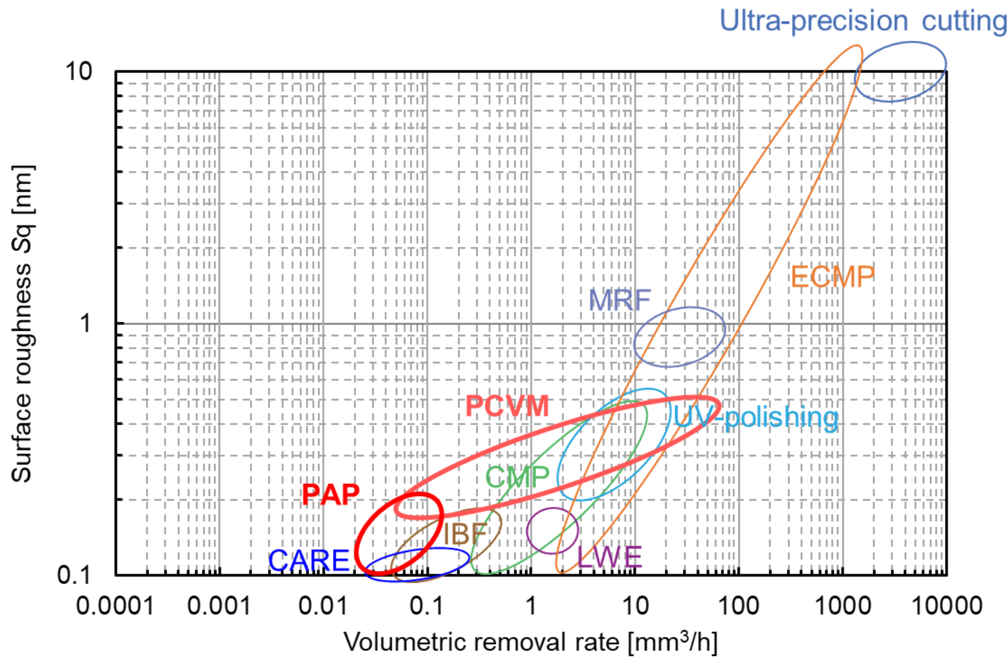

Figure 2.15 Relationship between the volumetric removal rate and the surface roughness *S*q of the various processing techniques.

believed that there are two main factors that lead to the relatively low MRR of PAP. One is the low modification rate. Since it is difficult for the radicals in the plasma to diffuse deeply into the substrate, the plasma modification only stays on the outermost surface of the substrate. The other one is the wear of the grindstone. Polishing film and resin-bonded grinding stones have been used in the PAP process until now [74, 97, 98)]. The surface of them got worn out easily during the PAP process and lose their original removal ability [100)]. If the grinding stone cannot be replaced or dressed in time, the polishing process will be hindered.

Figure 2.15 shows the relationship between the volumetric removal rate and the surface roughness *S*q of the various figuring techniques and polishing techniques that were introduced in section 2.2 and 2.3 [101)]. Each technique has its own advantages, but also has its own shortcomings. As the development goal of ultraprecision manufacturing technique, lower surface roughness at higher MRR is expected (the lower right area in Fig. 2.15). At present, for N-type SiC substrates, ECMP has achieved this goal well and has become the preferred method for SiC processing. But ECMP cannot process semiinsulating SiC and some other nonconductive ceramic materials. To develop an ultraprecision manufacturing technique for different application field of different difficult-to-machine brittle functional materials, plasma nanomanufacturing process, which combine PCVM and PAP, is proposed in this study. Plasma nanomanufacturing process combines the high MRR of PCVM and the high finishing quality of PAP and makes up the shortcomings of

each other. Since PCVM and PAP are both plasma-based dry processing techniques, the conversion of the two processes can be easily achieved. Taking the manufacturing of SiC as an example, in the PCVM stage, F-based plasma is generally used for etching to remove the SSD layer. After that, only need to change the process gas from F-based gas (CF_4 *et al.*) to O_2 gas or water vapor, and add a grinding stone tool, PCVM can be simply replaced to PAP.

2.5 Summary

To realize the highly efficient, cost effective, and damage-free nanoscale manufacturing of different difficult-to-machine brittle functional materials for different target, a review of the current figuring and polishing technique was conducted and the advantages and disadvantages of them were summarized. Plasma nanomanufacturing process, which combines PCVM and PAP, was proposed. In this chapter, the basics of plasma for processes, and the concepts and strategies of plasma nanomanufacturing are described.

(1) The high efficiency, low-cost and high-quality damage-free ultraprecision manufacturing of difficult-to-machine brittle functional materials is difficult owing to their high hardness and chemical inertness. In recent years, several figuring and polishing techniques were developed for these materials. However, there are still several challenges associated with these polishing techniques such as the low polishing efficiency, high cost, and limitation of applicable materials.

(2) Due to its chemical activity and high reactivity, plasma was a low-cost and effective processing tool for difficult-to-machine brittle functional materials. Frequent collisions between electrons and gas molecules/atoms in plasma can cause the reactions such as excitation, deexcitation, ionization, and dissociation. Since the released energy is related to the inherent properties of each atom or molecule, by measuring the characteristic emission light during the deexcitation process, the properties of the plasma can be monitored, and making the plasma become a controllable processing tool.

(3) As an efficient noncontact figuring technique with good form accuracy, PCVM has been successfully applied for the ultraprecision figuring of Si-based materials. However, PCVM cannot be used for finishing because of the isotropy of the etching process. As an excellent dry polishing technique, PAP has been proven to achieve damage-free finishing of a variety of difficult-to-machine brittle functional materials and obtain an atomically smooth surface. However, the problem of low MRR still needs to be resolved.

(4) Plasma nanomanufacturing process, which combines PCVM and PAP, was proposed in this study. Plasma nanomanufacturing process combines the advantages of the two technique and make up the shortcomings of each other, is expected to realize the highly efficient, cost effective, and damage-free nanoscale manufacturing of different difficult-to-machine brittle functional materials for different target.

References

1) G. Chapman, Ultra-precision machining systems; an enabling technology for perfect surfaces. *Moore Nanotechnology Systems*. (2004). http://www.nanotechsys.com/technology/technical-papers/

2) G. E. Davis, J. W. Roblee, A. R. Hedges, Comparison of freeform manufacturing techniques in the production of monolithic lens arrays, *Proceedings of the SPIE.* **7426** (2009) 742605.

3) S. R. Patterson, E. B. Magrab, Design and testing of a fast tool servo for diamond turning, *Precision Engineering.* **7** (1985) 123-128.

4) Y. Tohme, R. M. Principles, Applications of the slow slide servo, *Moore Nanotechnology Systems White Paper.* (2005).

5) F. Fang, X. Zhang, A. Weckenmann, G. Zhang, C. Evans, Manufacturing and measurement of freeform optics, *CIRP Annals- Manufacturing Technology.* **62** (2013) 823-846.

6) K. Mizutani, T. Kawano, Y. Tanaka, A piezoelectric-drive table and its application to micro-grinding of ceramic materials, *Precision Engineering.* **12** (1990) 219-226.

7) J. Yan, Z. Zhang, T. Kuriyagawa, Mechanism for material removal in diamond turning of reaction-bonded silicon carbide, *International Journal of Machine Tools & Manufacture.* **49** (2009) 366-374.

8) Y. Dai, L. Zhou, X. Xie, W. Liao, Y. Shen, Ion beam figuring technology, *Journal of Applied Optics.* **32** (2011) 753-760 (in Chinese).

9) Z. Xia, F. Fang, E. Ahearne, M. Tao, Advances in polishing of optical freeform surfaces: A review, *Journal of Materials Processing Technology.* **286** (2020) 116828.

10) A. Thomas, B. Jens, P. Fred, Advancements in ion beam figuring, *Optical Design and Fabrication 2019 (Freeform, OFT). OSA Technical Digest (Optical Society of America)* (2019) OM4A.6.

11) Z. Insepov, A. Hassanein, J. Norem, D. R. Swenson, Advanced surface polishing using gas cluster ion beams, *Nuclear Instruments and Methods in Physics Research B*. **261** (2007) 664-668.

12) A. B. Meinel, S. Bashkin, D. A. Loomis, Controlled figuring of optical surfaces by energetic ionic beams, *Applied Optics*. **4** (1965) 1674.

13) M. Weiser, Ion beam figuring for lithography optics, *Nuclear Instruments and Methods in Physics Research B*. **267** (2009) 1390-1393.

14) L. Zhou, Y. Dai, X. Xie, S. Li, Optimum removal in ion-beam figuring, *Precision Engineering.* **34**

(2010) 474-479.

15) P. Gailly, J. P. Collette, K. F. Frenette, C. Jamar, Ion beam figuring of CVD silicon carbide mirrors, *Proceedings of SPIE*. **10568** (2017) 105681G.

16) M. C. Rushford, J. A. Britten, S. N. Dixit, C. R. Hoaglan, M. D. Aasen, L. J. Summers, Wet-etch figuring for precision optical contouring, *Applied Optics.* **42** (2003) 5706-5713.

17) M. C. Rushford, J. A. Britten, C. R. Hoaglan, I. M. Thomas, L. J. Summers, S. N. Dixit, Wet-etch figuring: Optical surfacing by controlled application of etchant solution using the Marangoni effect, *Proceedings of SPIE.* **4451** (2001) 249-258.

18) K. Yamamura, Fabrication of ultra-precision optics by numerically controlled local wet etching, *Annals of the CIRP.* **56(1)** (2007) 541-544.

19) K. Yamamura, M. Nagano, H. Takai, N. Zettsu, D. Yamazaki, R. Maruyama, K. Soyama, S. Shimada, Figuring of plano-elliptical neutron focusing mirror by local wet etching, *Optics Express.* **17** (2009) 6414-6420.

20) K. Yamamura, Development of numerically controlled local wet etching, *Science and Technology of Advanced Materials.* **8** (2007) 158-161.

21) B. Davari, C. Koburger, T. Furukawa, *et al.*, A variable-size shallow trench isolation (STI) technology with diffused sidewall doping for submicron CMOS, *Technical Digest., International Electron Devices Meeting.* (1988) 92-95.

22) B. Davari, C. W. Koburger, R. Schulz, *et al.*, A new planarization technique, using a combination of RIE and chemical mechanical polish (CMP), *International Technical Digest on Electron Devices Meeting.* (1989) 61-64.

23) Y. Moon, Chemical and physical mechanisms of dielectric chemical mechanical polishing (CMP), *Advances in Chemical Mechanical Planarization (CMP). Woodhead Publishing.* (2016) 3-26.

24) X. Bi, R. Reed, P. Westerhoff, Control of nanomaterials used in chemical mechanical polishing/planarization slurries during on-site industrial and municipal biological wastewater treatment, *Frontiers of Nanoscience.* **8** (2015) 247-265.

25) J. Luo, D. A. Dornfeld, Material removal mechanism in chemical mechanical polishing: theory and modeling, *IEEE Transactions on Semiconductor Manufacturing.* **14** (2001) 112-133.

26) P. B. Zantye, A. Kumar, A. K. Sikder, Chemical mechanical planarization for microelectronics applications, *Materials Science and Engineering R.* **45** (2004) 89-220.

27) G. Pan, Y. Zhou, G. Luo, *et al.*, Chemical mechanical polishing (CMP) of on-axis Si-face 6H-SiC wafer for obtaining atomically flat defect-free surface, *Journal of Materials Science: Materials in Electronics.* **24** (2013) 5040-5047.

28) M. Forsberg, Effect of process parameters on material removal rate in chemical mechanical polishing of Si (100), *Microelectronic Engineering.* **77** (2005) 319-326.

29) Y. Wang, L. Zhang, A. Biddut, Chemical effect on the material removal rate in the CMP of silicon

wafers, *Wear.* **270** (2011) 312-316.

30) P. G. Neudeck, Progress in silicon carbide semiconductor electronics technology, *Journal of Electronic Materials.* **24** (1995) 283-288.
31) T. Kimoto, Material science and device physics in SiC technology for high-voltage power devices, *Japanese Journal of Applied Physics.* **54** (2015) 040103.
32) C. L. Neslen, W. C. Mitchel, R. L. Hengehold, Effects of process parameter variations on the removal rate in chemical mechanical polishing of 4H-SiC, *Journal of Electronic Materials.* **30** (2001) 1271-1275.
33) X. Shi, G. Pan, Y. Zhou, *et al.*, Characterization of colloidal silica abrasives with different sizes and their chemical-mechanical polishing performance on 4H-SiC (0001), *Applied Surface Science.* **307** (2014) 414-427.
34) Y. Zhou, G. Pan, X. Shi, *et al.*, Chemical mechanical planarization (CMP) of on-axis Si-face SiC wafer using catalyst nanoparticles in slurry, *Surface & Coatings Technology.* **251** (2014) 48-55.
35) S. Kurokawa, T. Doi, O. Ohnishi, *et al.*, Characteristics in SiC-CMP using MnO2 slurry with strong oxidant under different atmospheric conditions, *Materials Research Society Symposium Proceedings.* **1560** (2013) mrss13-1560-bb03-01.
36) H. S. Lee, D. I. Kim, J. H. An, *et al.*, Hybrid polishing mechanism of single crystal SiC using mixed abrasive slurry (MAS), *CIRP Annals - Manufacturing Technology.* **59** (2010) 333-336.
37) V. D. Heydemann, W. J. Everson, R. D. Gamble, *et al.*, Chemi-mechanical polishing of on-axis semi-insulating SiC substrates, *Materials Science Forum.* **457-460** (2004) 805-808.
38) C. G. Kim, W. S. Kim, Method for forming isolation layer of semiconductor device, United States Patent Application Publication. (2002) US2002/0137307 A1.
39) H. Hara, Y. Sano, H. Mimura, *et al.*, Novel abrasive-free planarization of 4H-SiC (0001) using catalyst, *Journal of Electronic Materials.* **35** (2006) L11-L14.
40) K. Arima, H. Hara, J. Murata, *et al.*, Atomic-scale flattening of SiC surfaces by electroless chemical etching in HF solution with Pt catalyst, *Applied Physics Letters.* **90** (2007) 202106.
41) H. Hara, Y. Morikawa, Y. Sano, K. Yamauchi, Termination dependence of surface stacking at 4H-SiC (0001) -1×1: Density functional theory calculations, *Physical Review B.* **79** (2009) 153306.
42) P. V. Bui, Y. Sano, Y. Morikawa, K. Yamauchi, Characteristics and mechanism of catalyst-referred etching method: Application to 4H-SiC, *International Journal of Automation Technology.* **12** (2018) 154-159.
43) T. Okamoto, Y. Sano, K. Tachibana, *et al.*, Dependence of process characteristics on atomic-step density in catalyst-referred etching of 4H-SiC (0001) surface, *Journal of Nanoscience and Nanotechnology.* **11** (2011) 2928-2930.
44) T. Okamoto, Y. Sano, K. Tachibana, *et al.*, Improvement of removal rate in abrasive-free planarization of 4H-SiC substrates using catalytic platinum and hydrofluoric acid, *Japanese Journal of Applied*

Physics. **51** (2012) 046501.

45) D. Toh, P. V. Bui, K. Yamauchi, Y. Sano, Photoelectrochemical oxidation assisted catalyst-referred etching for SiC (0001) surface, *International Journal Automation Technology.* **15** (2021) 74-79.

46) P. V. Bui, A. Isohashi, H. Kizaki, *et al.*, Study on the mechanism of platinum-assisted hydrofluoric acid etching of SiC using density functional theory calculations, *Applied Physics Letters.* **107** (2015) 201601.

47) A. Isohashi, P. V. Bui, D. Toh, *et al.*, Chemical etching of silicon carbide in pure water by using platinum catalyst, *Applied Physics Letters.* **110** (2017) 201601.

48) P. V. Bui, D. Toh, A. Isohashi, *et al.*, Platinum-catalyzed hydrolysis etching of SiC in water: A density functional theory study, *Japanese Journal of Applied Physics.* **57** (2018) 055703.

49) S. Hong, J. Watanabe, M. Touge, Precision polishing technology of SiC single crystal under ultraviolet-ray irradiation, *International Journal for Manufacturing Science & Technology.* **9** (2007) 23-28.

50) T. Sakamoto, T. Inaki, K. Oda, *et al.*, Ultraviolet-assisted polishing of 4 inch SiC substrate, *Journal of the Japan Society for Abrasive Technology.* **58** (2014) 235-240.

51) J. Watanabe, M. Touge, T. Sakamoto, Ultraviolet-irradiated precision polishing of diamond and its related materials, *Diamond & Related Materials.* **39** (2013) 14-19.

52) Y. Ishikawa, Y. Matsumoto, Y. Nishida, *et al.*, Surface treatment of silicon carbide using TiO_2 (IV) photocatalyst, *Journal of the American Chemical Society.* **125** (2003) 6558-6562.

53) M. Touge, T. Nakano, K. Yamaguchi, *et al.*, Study on precision finishing of PCD by constant-pressure grinding and UV-polishing, *Key Engineering Materials.* **407-408** (2009) 388-391.

54) A. Anan, M. Touge, A. Kubota, J. Watanabe, Study on ultra precision polishing of single crystal diamond substrates under ultraviolet irradiation, *Key Engineering Materials.* **407-408** (2009) 355-358.

55) T. Tagawa, M. Touge, T. Sakamoto, *et al.*, Study on UV-assisted polishing of diamond wafer for power electric devices, *Journal of the Japan Society for Precision Engineering.* **80** (2014) 587-591.

56) J. Huo, R. Solanki, J. McAndrew, Electrochemical planarization of patterned copper films for microelectronic applications, *Journal of Materials Engineering and Performance.* **13** (2004) 413-420.

57) N. Kulyk, C. Y. An, J. H. Oh, *et al.*, Study on electrochemical mechanical polishing process of copper circuit on PCB, *Korean Journal of Chemical Engineering.* **27** (2010) 310-314.

58) S. J. Lee, Y. M. Lee, M. Y. Chung, Metal removal rate of the electrochemical mechanical polishing technology for stainless steel – the electrochemical characteristics, *Proceedings of the Institution of Mechanical Engineers, Part B: Journal of Engineering Manufacture.* **220** (2006) 525-530.

59) X. Chu, L. Bai, T. Chen, Investigation on the electrochemical-mechanical polishing of NiP substrate of hard disk, *Rare Metal Materials and Engineering.* **40(11)** (2011) 1906-1909.

60) C. Li, I. B. Bhat, R. Wang, J. Seiler, Electro-chemical mechanical polishing of silicon carbide, *Journal of Electronic Materials.* **33** (2004) 481-486.

61) X. Yang, X. Yang, K. Kawai, *et al.*, Highly efficient planarization of sliced 4H-SiC (0001) wafer by slurryless electrochemical mechanical polishing, *International Journal of Machine Tools and Manufacture.* **144** (2019) 103431.

62) X. Yang, X. Yang, R. Sun, *et al.*, Obtaining atomically smooth 4H-SiC (0001) surface by controlling balance between anodizing and polishing in electrochemical mechanical polishing, *Nanomanufacturing and Metrology.* **2** (2019) 140-147.

63) X. Yang, X. Yang, K. Kawai, Novel SiC wafer manufacturing process employing three-step slurryless electrochemical mechanical polishing, *Journal of Manufacturing Process.* **70** (2021) 350-360.

64) W. I. Kordonski, Adaptive structures based on magnetorheological fluids, *Third International Conference on Adaptive Structure.* (1992) 13-17.

65) W. I. Kordonski, S. D. Jacobs, Magnetorheological finishing, *International Journal of Modern Physics B.* **10** (1996) 2837-2848.

66) Z. P. Shulman, V. I. Kordonsky, E. A. Zaltsgendler, *et al.*, Structure, Physical properties and dynamics of magnetorheological suspensions, *International Journal of Multiphase Flow.* **12** (1986) 935-955.

67) S. D. Jacobs, D. Golini, Y. Hsu, *et al.*, Magnetorheological finishing: a deterministic process for optics manufacturing, *Proceedings of SPIE.* **2576** *International Conference on Optical Fabrication and Testing* (1995) 372-382.

68) Y. Wang, S. Yin, H. Huang, F. Chen, G. Deng, Magnetorheological polishing using a permanent magnetic yoke with straight air gap for ultra-smooth surface planarization, *Precision Engineering.* **40** (2015) 309-317.

69) K. Saraswathamma, J. Sunil, R. P. Venkateswara, Rheological behavior of magnetorheological polishing fluid for Si polishing, *Materials Today: Proceedings.* **4** (2017) 1478-1491.

70) W. Song, Z. Peng, P. Li, *et al.*, Annular surface micromachining of titanium tubes using a magnetorheological polishing technique, *Micromachines.* **11(3)** (2020) 314.

71) H. Cheng, Z. Feng, Y. Wang, S. Lei, Magnetorheological finishing of SiC aspheric mirrors, *Materials and Manufacturing Processes.* **20** (2005) 917-931.

72) A. Philipossian, E. Mitchell, Slurry utilization efficiency studies in chemical mechanical planarization, *Japanese Journal of Applied Physics.* **42** (2003) 7259-7264.

73) Y. Mori, K. Yamamura, K. Yamauchi, *et al.*, Plasma CVM (chemical vaporization machining): an ultra precision machining technique using high-pressure reactive plasma, *Nanotechnology.* **4** (1993) 225-229.

74) K. Yamamura, T. Takiguchi, M. Ueda, *et al.*, Plasma assisted polishing of single crystal SiC for obtaining atomically flat strain-free surface, *CIRP Annals – Manufacturing Technology*. **60** (2011) 571-574.

75) H. Sugai, Inter university – Plasma electronics, *Ohmsha*, 2016.

76) H. R. Griem, Principles of plasma spectroscopy, *Fast Electrical and Optical Measurements.* **108/109**

(1986) 885-910.

77) A. Thorne, U. Litzen, S. Johansson, Spectrophysics: Principles and applications, Springer, 1999.

78) A. J. M. Mackus, S. B. S. Heil, E. Langereis, *et al.*, Optical emission spectroscopy as a tool for studying, optimizing, and monitoring plasma-assisted atomic layer deposition processes, *Journal of Vacuum Science & Technology A.* **28** (2010) 77-87.

79) U Fantz, Basics of plasma spectroscopy, *Plasma Sources Science and Technology.* **15** (2006) S137-S147.

80) Collisional Cross Section. (2021, June 20). *https://chem.libretexts.org/@go/page/1403*

81) Mean Free Path, Molecular Collisions. (Retrieved 2011-11-08). *http://hyperphysics.phy-astr.gsu.edu/hbase/Kinetic/menfre.html*

82) H. Eichhorn, K. H. Schoenbach, T. Tessnow, Paschen's law for a hollow cathode discharge, *Applied Physics Letters.* **63** (1993) 2481-2483.

83) M. A. Lieberman, A. J. Lichtenberg, Principles of plasma discharges and materials processing (2nd edition), *Wiley-Interscience.* 2005.

84) S. M. Irving, K. E. Lemons, G. E. Bobos, Gas plasma vapor etching process, *U. S. Patent No. 3,615,956.* (filed 1969)

85) S. M. Irving, A plasma oxidation process for removing photoresist films, *Solid State Technology.* **14** (1971) 47-51.

86) H. F. Winters, J. W. Coburn, Surface science aspects of etching reactions, *Surface Science Reports.* **14** (1992) 161-269.

87) J. W. Coburn, H. F. Winters, Plasma etching – A discussion of mechanisms, *Journal of Vacuum Science & Technology.* **16** (1979) 391-403.

88) J. W. Coburn, Plasma-assisted etching, *Plasma Chemistry and Plasma Processing.* **2** (1982) 1-41.

89) R. G. Poulsen, Plasma etching in integrated circuit manufacture – A review, *Journal of Vacuum Science & Technology.* **14** (1977) 266-274.

90) B. Wu, Photomask plasma etching: A review, *Journal of Vacuum Science & Technology B: Microelectronics and Nanometer Structures Processing, Measurement, and Phenomena.* **24** (2006) 1-15.

91) V. M. Donnelly, A. Kornblit, Plasma etching: Yesterday, today, and tomorrow, *Journal of Vacuum Science & Technology A.* **31** (2013) 050825.

92) G. S. Oehrien, R. J. Phaneuf, D. B. Graves, Plasma-polymer interactions: A review of progress in understanding polymer resist mask durability during plasma etching for nanoscale fabrication, *Journal of Vacuum Science & Technology B.* **29** (2011) 010801.

93) K. Yamamura, K. Yamauchi, H. Mimura, et al., Fabrication of elliptical mirror at nanometer-level accuracy for hard x-ray focusing by numerically controlled plasma chemical vaporization machining, *Review of Scientific Instruments.* **74** (2003) 4549-4553.

94) Y. Mori, K. Yamamura, Y. Sano, Thinning of silicon-on-insulator wafers by numerically controlled plasma chemical vaporization machining, *Review of Scientific Instruments.* **75** (2004) 942-946.

95) Y. Sano, K. Yamamura, H. Mimura, et al., Fabrication of ultrathin and highly uniform silicon on insulator by numerically controlled plasma chemical vaporization machining, *Review of Scientific Instruments.* **78** (2007) 086102.

96) K. Yamamura, S. Shimada, Y. Mori, Damage-free improvement of thickness uniformity of quartz crystal wafer by plasma chemical vaporization machining, *CIRP Annals – Manufacturing Technology.* **57** (2008) 567-570.

97) H. Deng, K. Yamamura, Atomic-scale flattening mechanism of 4H-SiC (0001) in plasma assisted polishing, *CIRP Annals – Manufacturing Technology.* **62** (2013) 575-578.

98) H. Deng, K. Endo, K. Yamamura, Plasma-assisted polishing of gallium nitride to obtain a pit-free and atomically flat surface, *CIRP Annals – Manufacturing Technology.* **64** (2015) 531-534.

99) K. Yamamura, K. Emori, R. Sun, et al., Damage-free highly efficient polishing of single-crystal diamond wafer by plasma-assisted polishing, *CIRP Annals – Manufacturing Technology.* **67** (2018) 353-356.

100) H. Deng, Development of plasma-assisted polishing for highly efficient and damage-free finishing of single-crystal SiC, GaN and CVD-SiC, *Doctoral Dissertation, Osaka University Knowledge Archive*, 2016.

101) K. Yamamura, Research on ultra-precision machining with PCVM, *Doctoral Dissertation, Osaka University Knowledge Archive*, 2000.

Chapter 3

Optimization of AP-PCVM technique for processing ultrathin quartz crystal wafer

3.1 Introduction

As a part of plasma nanomanufacturing process, AP-PCVM is a technique that can efficiently remove low spatial frequency components and has been successfully applied to improve the thickness uniformity of ultrathin quartz crystal wafer [1)]. However, helium (He) gas has been used as the carrier gas in AP-PCVM until now. The He gas used in industry is mostly produced from natural gas. Problems such as the depletion of natural resources and a high cost are of wide concern. It is necessary to find a cost effective and renewable gas to replace He as the carrier gas for AP-PCVM. In this chapter, the optimization of processing conditions in AP-PCVM for ultrathin quartz crystal wafers was carried out. As a result, through the optimization of the gas composition used in AP-PCVM, argon (Ar) was successfully used instead of helium, and the same etching rate as that using He was obtained. It is considered that using Ar instead of He as the carrier gas in AP-PCVM will effectively solve problems such as the depletion of natural resources and high cost.

3.2 AP-PCVM setup

Figure 3.1 shows a schematic diagram of the AP-PCVM setup used in correction of thickness distribution for ultrathin quartz crystal wafer. Three flow paths exist, one for the carrier gas, and two for the process gases (CF_4 and O_2). The flow rates of the carrier gas and process gases were controlled using mass flow controllers (MFCs). The mixture gas was supplied from the center of the electrode and flowed through the space between the aluminum alloy electrode and the alumina ceramic cover arranged coaxially with the electrode. The size of the AT-cut ultrathin quartz crystal wafers used in the experiment was 54 mm × 50 mm × 30 ~ 90 μm^t. All the AP-PCVM experiments in this paper were conducted at room temperature (23.3°C) without substrate heating. The quartz crystal wafer was held on a *XY* worktable by a vacuum chuck. The relative position and speed between the electrode and the wafer are controlled using the *XY* worktable (*X*- and *Y*-axes) and the electrode (*Z*-axis) driven by AC servo motors. The distance between the tip of the electrode and the quartz crystal wafer was 3.5 mm, and the gap between the tip of the ceramic cover and

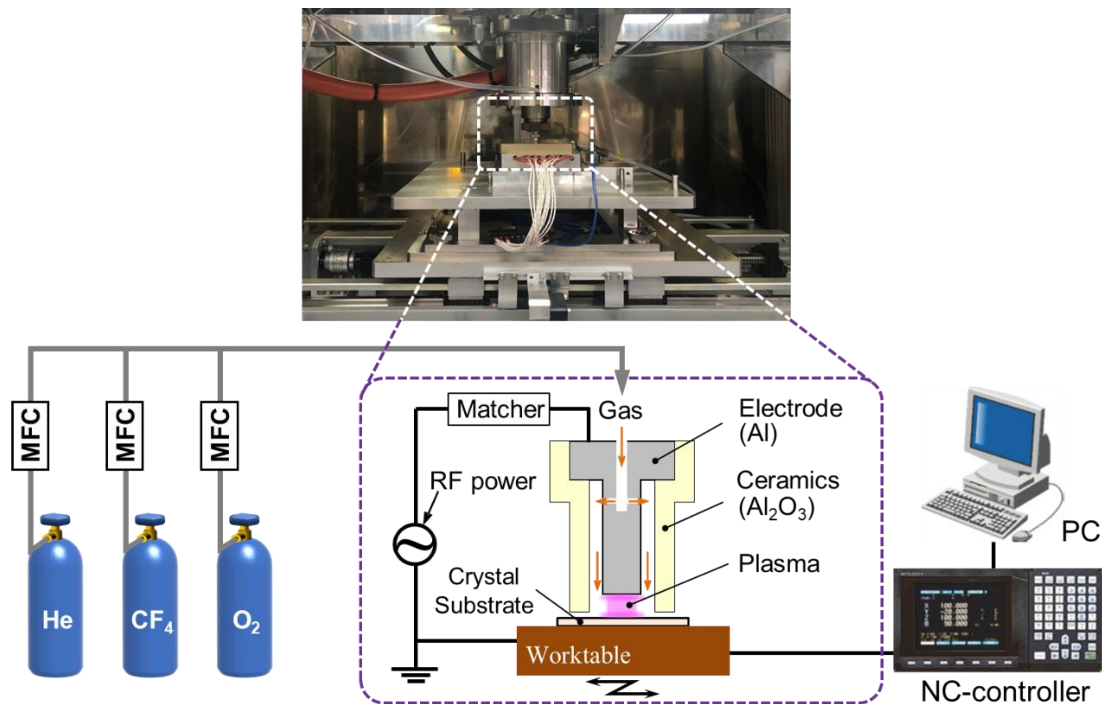

Figure 3.1 Schematic diagram of the AP-PCVM setup.

the quartz crystal wafer was 0.5 mm. The diameter of the powered electrode was 3 mm. Atmospheric-pressure Ar-based CF_4 plasma was generated by applying 13.56 MHz radio frequency (RF) power between the electrode and the worktable. Fluorine radicals, which are the reactive species that etch the quartz crystal, were generated by the dissociation of CF_4 in the atmospheric-pressure Ar plasma.

3.3 Current application of AP-PCVM to ultrathin quartz crystal wafer

To increase the communication speed, the resonance frequency of the quartz crystal unit should be increased by reducing the thickness of the quartz crystal blank. For a 80 MHz crystal unit, the thickness is only around 20 μm. Figure 3.2 shows the thickness comparison between a coin and a quartz crystal wafer. Such a thin wafer is easily broken due to the application of mechanical external force in conventional contact processing. In addition, with the continuous miniaturization of various electronic products, the size of the crystal oscillator must also be miniaturized. Although the wafer process has been successfully applied in the field of chip manufacturing, the brittleness of quartz wafers poses a challenge to the wafer process for quartz units. In addition, technique to process the thickness of the wafer uniformly is indispensable for the realization of miniaturization of the crystal unit. AP-PCVM is an ultraprecise figuring technique that uses

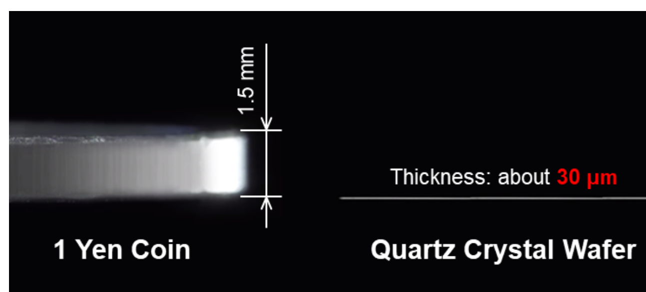

Figure 3.2 Thickness comparison between a coin and a quartz crystal wafer.

fluorine radicals generated by atmospheric-pressure plasma to change the surface atoms of a substrate into volatile reaction products to form the desired shape. Since AP-PCVM is a noncontact chemical figuring technique that does not apply a mechanical load to substrates, the breakage of thin brittle materials is prevented and no subsurface damage (SSD) layer is formed during the chemical removal process [2, 3)]. Moreover, as AP-PCVM is an atmospheric-pressure process, no vacuum chamber is required. Until now, the most widely used methods for plasma generation at AP have mainly included inductively coupled plasma (ICP) [4, 5)], capacitively coupled plasma (CCP) [3)], and microwave plasma (plasma jet) [2, 6)]. Since ICP and microwave plasma produce high temperatures exceeding 200ºC, the possibility of both crystal twinning and breaking of the quartz crystal wafer increases. Therefore, AP-PCVM use CCP is the preferred method for the thickness uniformization of ultrathin quartz crystal wafer.

K. Yamamura *et al.* has proved that [7)], by applying AP-PCVM for improving the thickness uniformity of a commercially available ultrathin quartz crystal wafer, as shown in Fig. 3.3, the thickness uniformity was improved from 122.6 to 14.9 nm, and the standard deviation of the thickness variation was improved from 33.2 to 3.2 nm within only 107 s without inducing subsurface crystallographic damage [7)]. As shown in Fig. 3.4, KYOCERA has developed the

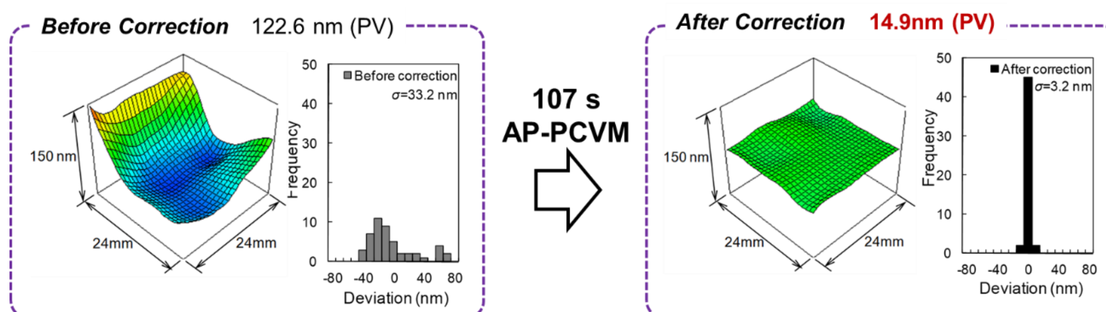

Figure 3.3 Correction results for the thickness distribution of the ultrathin quartz crystal wafer by AP-PCVM [7)].

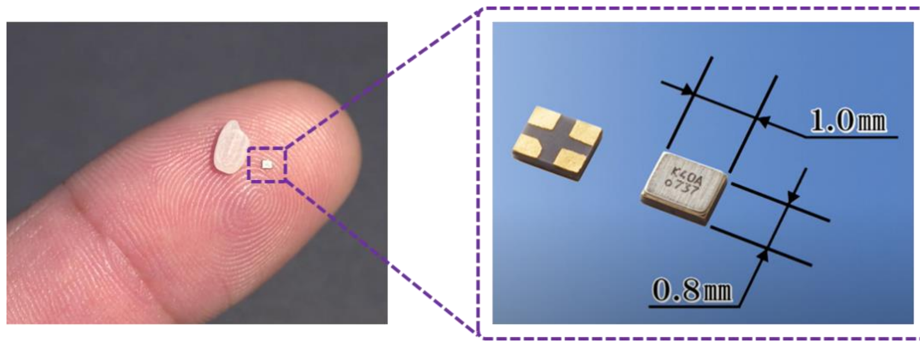

Figure 3.4 The world's smallest quartz crystal unit (CX1008) developed by KYOCERA [8].

world's smallest crystal unit CX1008 (1.0 × 0.8 mm) for smartphones, wearables, and other electronic devices by applying AP-PCVM.

3.4 Challenge of using Ar instead of He as the carrier gas in AP-PCVM

Although in the processing of ultrathin quartz crystal wafers, AP-PCVM has achieved excellent results and has been industrially applied. However, helium gas has been used as the carrier gas in AP-PCVM until now. The helium gas used in the industry is mostly produced from natural gas. Problems such as the depletion of natural resources and high cost are of wide concern [9]. To solve these problems, research on the use of argon gas instead of helium gas as a carrier gas has been proposed, as it can be industrially produced by the fractional distillation of liquid air, in the generation of atmospheric-pressure plasma. Although the operation cost can be reduced by using argon instead of helium, the breakdown voltage for argon is much higher than that for helium [10]. Figure 3.5 shows the plasma generated on ultrathin quartz crystal wafer using Ar as the carrier gas. As is well known, the higher breakdown voltage may cause the rapid multiplication of electrons after breakdown, leading to the formation of filamentary arc streamers [11]. And the

Figure 3.5 Photograph of plasma generated on ultra-thin quartz crystal wafer using Ar as the carrier gas.

ultrathin quartz crystal wafer will be easily broken because of the locally high temperature due to the localized filamentary arc streamers.

3.5 Penning effect caused by adding ethanol to Ar plasma

Many researchers have made many efforts to generate an atmospheric-pressure stable glow discharge Ar plasma, and the addition of ethanol to Ar has been proven to be very useful, as reported by Sun *et al.* [12]. The reason for the stable glow discharge produced by adding ethanol was the Penning effect [13] that occurred inside the plasma. Before explaining the Penning effect, we must first understand the energy transfer inside the atom in plasma. In section 2.4.2.1, the energy transfer caused by the collision between electrons and atoms/molecules in the plasma has been briefly introduced. Here, taking the simple Ne atom as an example, the energy state of the electrons inside the atom will be explained in detail.

Considering the classical mechanics that regards electrons as particles, a model was established in which negatively charged electrons are circularly moving around a positively charged heavy nucleus in an atom, and centrifugal and Coulomb forces were balanced. When an electron collides with this atom from outside, the nucleus receives momentum and the velocity of translational motion of the atom also changes. In addition, if kinetic energy is directly given to the electrons orbiting the nucleus at the time of collision, the electrons will draw a larger circle than before (Excited collision). The larger the collision energy, the electron in the atom draws a larger circle, and finally cuts off the Coulomb attraction and leaves the atom to separate into free electrons and positive ion (Ionization collision). According to it, the arrangement of electrons in an atom is determined by four quantum numbers (energy (n), angular momentum (l), magnetic moment (m_l), and spin (m_s)), and the internal energy state allows only a specific discrete energy level. Since it is not allowed for two electrons to occupy the same energy level at the same time, the state of the atom with the lowest energy and stability (Ground state) will have a structure in which electrons are filled in the order from the orbit of the lower energy. In the ground state of Ne, 10 electrons satisfy all three orbitals (1s, 2s, 2p) up to the principal quantum number n = 2, and the electron configuration is expressed as $1s^2 2s^2 2p^6$. Figure 3.6 shows the energy-level diagram of the state with higher energy (Excited state) using the ground state as the energy reference (zero). As shown in the figure, the 3s orbital has four excited states, and the 3p orbital above has six excited levels. Further increasing the quantum number, such as to 3d, 4s, 4p, etc., and to the highest energy level of 21.55eV. This energy indicates the minimum energy (Ionization energy) required to ionize a Ne atom from the base state, and ionization occurs when the kinetic energy of an electron colliding with Ne exceeds the ionization energy.

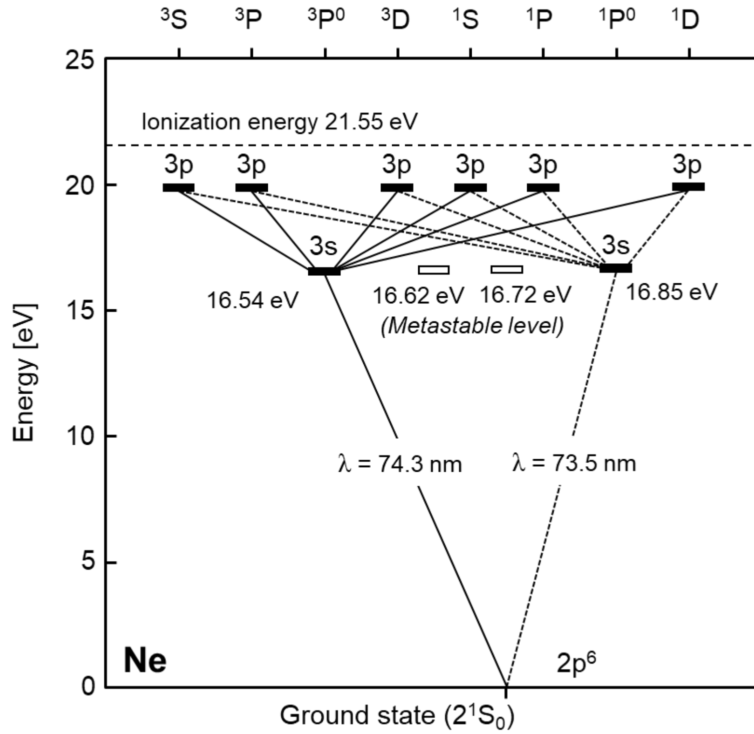

Figure 3.6 Energy-level diagram of atomic Ne [14].

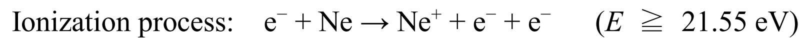

Ionization process: $e^- + Ne \rightarrow Ne^+ + e^- + e^-$ $(E \geqq 21.55\ \text{eV})$

The Penning effect mainly considers the excitation process below the ionization process.

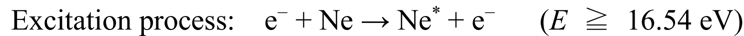

Excitation process: $e^- + Ne \rightarrow Ne^* + e^-$ $(E \geqq 16.54\ \text{eV})$

Normally, the excited state is unstable and causes electric dipole radiation in a short time (~ 50 ns) to return to the ground state (Deexcitation). In the above example, with Ne^* from the excited state back to the ground state, a light with a wavelength of λ = 74.3 nm, corresponding to the energy of 16.54 eV in the excited state of Ne^*, is spontaneously emitted.

$$\lambda = \frac{hc}{\Delta E_{(16.54\ \text{eV})}} = 74.3\ nm \tag{3-1}$$

This light is invisible because it is ultraviolet light, but since the energy difference is small when falling from the 3p orbital to the 3s orbital, a red light with a wavelength around 700 nm is emitted.

Changing of the energy level by absorbing or emitting light as described above is generally called transition. Transitions are not allowed between arbitrary levels, and the case where the transition is allowed by satisfying the selection rule is called allowable transition, and the case where the transition is not allowed is called forbidden transition [14]. As shown in Fig. 3.6,

transition is not allowed to fall from the 16.62 eV level (3^3p_2) and 16.72 eV level (3^3P_0) to the ground state through the emission of light. It is also not allowed to absorb light and rise from the ground state. Such an excited level at which the transition to the ground state is optically prohibited is called metastable level. The transition from the ground state to the metastable state is impossible with light absorption, but it is possible in the case of electron collision.

Excitation process to metastable state: $e^- + Ne \rightarrow Ne^m + e^-$ $(E \geqq 16.62 \text{ eV})$

The generated atom at metastable state is written as Ne^m. Once excited to the metastable state, it is forbidden to fall to the ground state naturally, so the life of the metastable state is significantly longer ($10^{-4} \sim$ s). For back to the ground state, it is possible to escape from the metastable state by colliding with other particles or absorbing photons and then releasing it after rising to the normal excited level. Or inelastically colliding with other atoms/molecules, or with the vessel wall.

Atoms at metastable state often play an important role in plasma. A famous example of this is the Penning effect, which was named after Penning's discovery in 1937 [15)]. According to the experiments conducted by F. M. Penning *et al.*, igniting a DC discharge of Ne gas at 50 mTorr required a high voltage of about 800 V, but breakdown voltage can be reduced by a factor of four by adding only 0.1% argon into Ne gas. This result is believed to be due to the Penning effect, which is due to the metastable atom of Ne. This concept is explained with the ionization process of Ne, for which electron collision does not occur unless the kinetic energy of electrons exceeds 21.55 eV, so it does not discharge unless a high voltage is applied to strengthen the electric field. However, the process of forming metastable atoms is possible at a lower energy of E_m = 16.62 eV. Furthermore, when these metastable Ne atoms with high internal energy collides with Ar, E_m is higher than the ionization voltage of Ar (15.75 eV).

Ionization process with metastable state: $Ne^m + Ar \rightarrow Ne + Ar^+ + e^-$

The above reaction occurred, and Ar was easily ionized. Therefore, even if only a small amount of Ar was added, the plasma will be easily discharged.

After understanding the principle of Penning effect, the topic will be brought back to the plasma used in AP-PCVM. In the research of K. Yamamura *et al.*, He gas was used as the carrier gas in AP-PCVM. However, filamentary arc streamers were formed easily in the plasma generated using pure Ar as the carrier gas. To investigate the difference between He-based and Ar-based CF_4 plasmas, a comparative experiment was conducted using the setup shown in Fig. 3.1. The RF power was 60 W. The carrier gas was He/Ar (600 sccm) and the process gases were CF_4 (10 sccm) and O_2 (4 sccm). Figure 3.7 shows photographs and optical emission spectroscopy (OES) spectra of plasma generated on quartz crystal wafer using He as the carrier gas. Table 3.1 shows

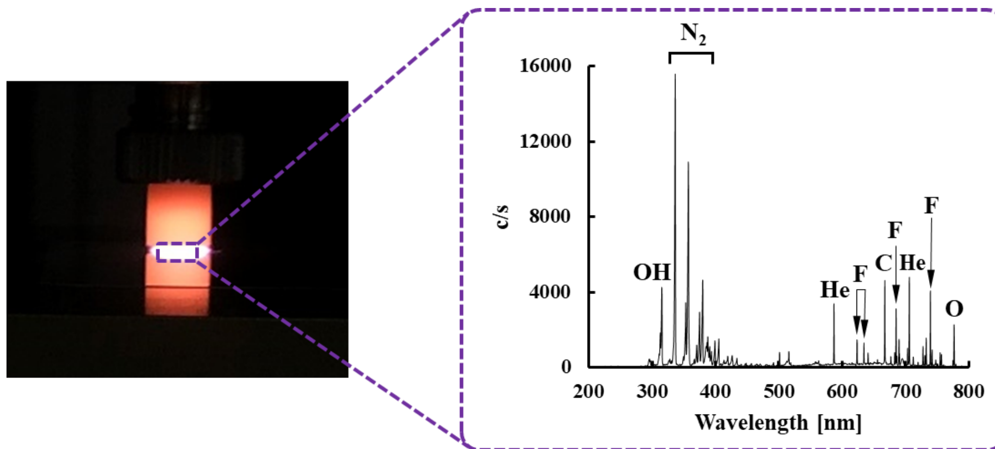

Figure 3.7 Photographs and OES spectra of plasma generated on quartz crystal wafer using He as the carrier gas.

Table 3.1 State energy of some related atoms and molecules [16-18].

Gas	He		Ar		N_2	C_2H_5OH	CF_4	O_2
Ionization energy [eV] (State lifetime [ns]) [19]	24.6 (0.1 ~ 9.9)		15.8 (0.3 ~ 9.6)		15.58	10.5	15.9	12.2
Metastable energy [eV] (State lifetime [s]) [19]	19.82 (7900)	20.6 (0.02)	11.72 (50)	11.55 (60)				

the ionization energy and metastable energy of some related atoms or molecules. Since the ionization energy of He is 24.6 eV, and two high-energy metastable states He (2^3S_1), 19.82 eV, He (2^1S_0), 20.6 eV can be formed in the discharge [16]. Because plasma was generated in atmospheric-pressure and the ionization energy of N_2 (15.58 eV) is lower than the potential energy of the two high-energy metastable states of He atoms.

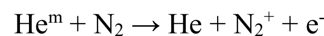

$$He^m + N_2 \rightarrow He + N_2^+ + e^-$$

It is easy for He atoms in the high-energy metastable states to ionize N_2 molecules to generate N_2^+ ions at the He/air interface via Penning effect as above. The OES spectra of the plasma using He as the carrier gas also confirmed this. Strong peaks corresponding to N_2 was observed. Figure 3.8 shows photographs and OES spectra of plasma using ethanol-added Ar as the carrier gas. The other experimental conditions were the same and the ethanol flow rate was 0.003 g/min controlled using a liquid mass flow controller. In the case of using pure Ar as the carrier gas, the ionization energy for Ar is 15.8 eV, and Ar atom has two metastable levels at 11.72 and 11.55 eV [17, 18], which

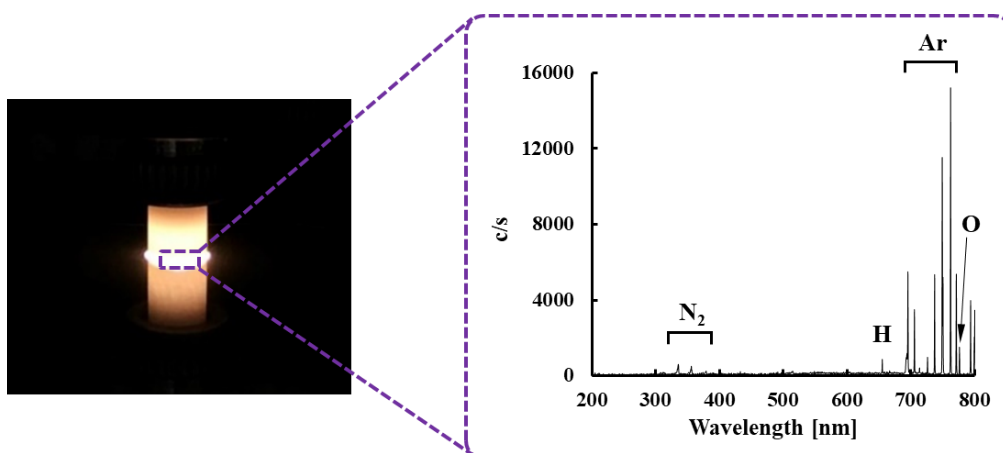

Figure 3.8 Photographs and OES spectra of plasma generated on quartz crystal wafer using ethanol-added Ar as the carrier gas.

is lower than the ionization energy of N_2, CF_4, and O_2. Penning effect cannot occur at the Ar/air, Ar/CF_4, or Ar/O_2 combination. As shown in Fig. 3.5, the energy cannot be transferred continues to accumulate result in the formation of filamentary arc streamers, and the ultrathin quartz crystal wafer was easily broken. When a small amount of ethanol was added into Ar, because the ionization energy 10.47 eV for ethanol is lower than the potential energy of the high-energy metastable states Ar atoms [20].

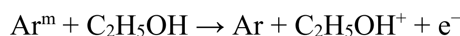

$$Ar^m + C_2H_5OH \rightarrow Ar + C_2H_5OH^+ + e^-$$

Penning effect occurred and the breakdown voltage was significantly reduced, a stable glow discharge plasma was generated as shown in Fig. 3.8. Since Penning effect cannot occur at the Ar/air combination, there was no strong N_2 peak was observed in OES spectra.

3.6 Different etching characteristics using ethanol-added Ar and He as the carrier gas in AP-PCVM

In the previous section, it has been confirmed that adding a small amount of ethanol to Ar can avoid the formation of filamentary arc streamers and generate a stable atmospheric-pressure plasma. In this section, the investigation of the different etching characteristics was conducted on ultrathin quartz crystal wafers using He or ethanol-added Ar as the carrier gas. To provide a stable flow of ethanol vapor and mix it fully with other gases, the gas supply system of the setup shown in Fig. 3.1 has been modified, and the schematic diagram was shown in Fig. 3.9. Ethanol vapor was introduced using the gas–liquid mixture vaporization method. The carrier gas (Ar) and liquid ethanol (concentration 99.5%), where the latter was controlled using liquid mass flow controllers

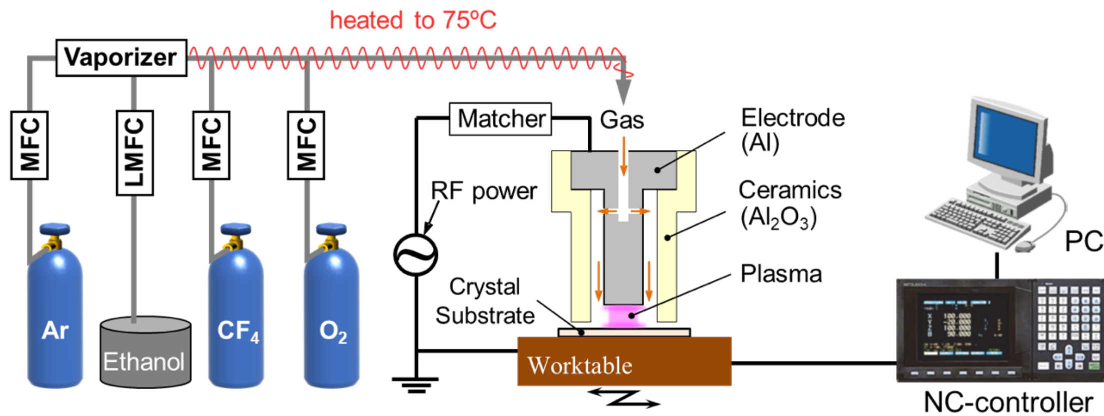

Figure 3.9 Schematic diagram of the AP-PCVM setup using ethanol-added Ar as the carrier gas.

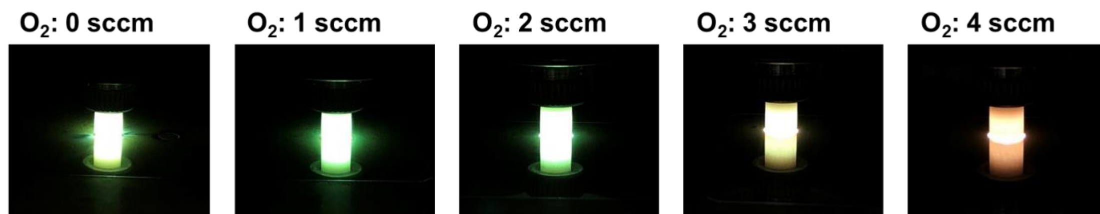

Figure 3.10 Photographs of plasma at various oxygen flow rates.

(LMFCs), were heated, and mixed in the vaporizer. The gas tube from the vaporizer to the electrode was heated to 75ºC with a heater to avoid the ethanol liquefaction.

At first, experiments were conducted on quartz crystal wafers in which different oxygen flow rates were applied. The RF power was 60 W and the ethanol flow was 0.003 g/min. The carrier gas was Ar (600 sccm) and the process gases were CF_4 (10 sccm) and O_2 (0–8 sccm). Figure 3.10 shows the photographs of plasma in each condition. Different wavelengths of light show different colors, which means that the types of radicals in plasma with different oxygen flow rates were different. Figure 3.11 shows photographs of removal spots on quartz crystal wafers formed by AP-PCVM using ethanol-added argon as the carrier gas, OES spectra of the plasma, and X-ray photoelectron spectroscopy (XPS) measurement results of the processed area at various oxygen flow rates. Firstly, no oxygen was added to the process gas. Under this condition, a concentrated black deposit was formed in the area surrounding the removal spot as shown in Fig. 3.11(a). From the OES spectrum of the plasma shown in Fig. 3.11(f), a strong emission of C_2 Swan band peaks was observed [21]. In addition, as described in section 3.5, since the plasma was generated at AP,

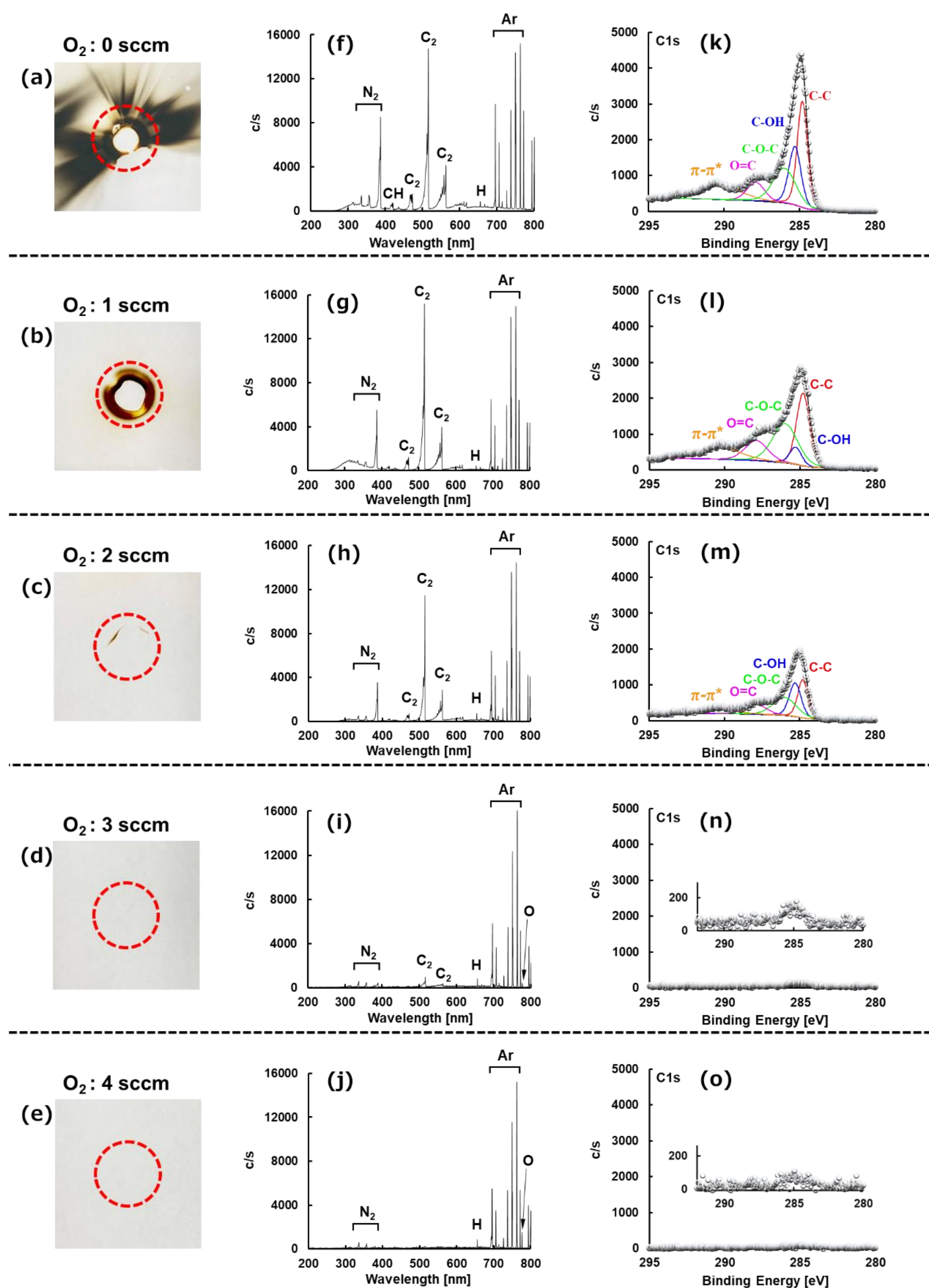

Figure 3.11 Photographs (a)–(e) of removal spots formed by AP-PCVM on quartz crystal wafers using ethanol-added argon as the carrier gas, optical emission spectroscopy (OES) spectra of the plasma used in AP-PCVM (f)–(j), and X-ray photoelectron spectroscopy (XPS) measurements (k)–(o).

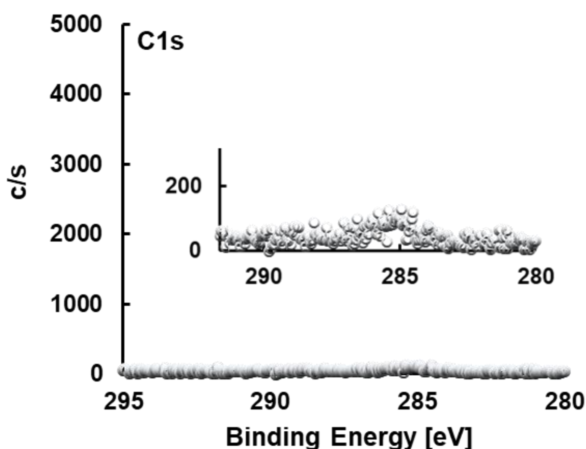

Figure 3.12 X-ray photoelectron spectroscopy (XPS) measurements of the sample surface before the plasma treatment.

N_2 mixed into the plasma from the ambient was also dissociated and excited, so emissions from N_2 were observed in the OES spectrum [22, 23]. Next, the XPS measurement of the area with the black deposit was conducted (Fig. 3.11(k)). A strong peak was observed in the C1s spectrum obtained from the area with the black deposit. To elucidate and discuss the composition of the black deposit, the deconvolution spectra of C1s were evaluated from the chemical shifts relative to the C–C peak at 284.8 eV [24]. Four peaks in addition to the C–C peak, which were attributed to C–OH (285.3 eV), C–O–C (286.0 eV), C=O (287.9 eV), and π–π* (290.4 eV), were observed [24, 25]. The shake-up satellite peak (π–π*, 290.4 eV) assigned to π-electrons was delocalized at the aromatic network in graphite and disappeared with increasing oxidation [26]. Jimenez *et al*. also observed the C_2 Swan band from ethanol-added argon plasma in addition to a carbon deposit [27]. Research on the production of graphene by ethanol chemical vapor deposition has also been reported by G. Faggio *et al.* [28]. Thus, it is considered that the black deposit originated from incompletely decomposed carbon from ethanol. Next, 1 sccm of oxygen was added to the process gas. A carbon deposit still existed, but its color was lighter and the deposition area became smaller. Compared with the OES spectrum of the plasma without adding oxygen, the emission of the C_2 Swan band was weaker. From the XPS measurement result, it was found that the C–C peak became weaker. It was considered that through the addition of oxygen to the process gas, part of the incompletely decomposed carbon was oxidized. Thus, it is predicted that the addition of oxygen can suppress the formation of the carbon deposit on the quartz crystal surface. As shown in the OES spectra in Fig. 3.11, by increasing the oxygen flow rate from 0 to 4 sccm, the optical emission from atomic oxygen became stronger and the emission from the C_2 Swan band became weaker. When the oxygen flow rate was increased to 4 sccm, the optical emission from the C_2 Swan band of the plasma almost disappeared. Also, there was no C peak in the XPS spectrum (the

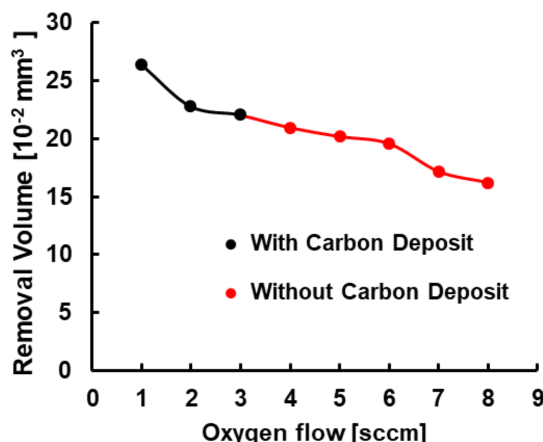

Figure 3.13 Removal volume of quartz crystal wafer in 60 s with different O_2 fractions.

same as the sample before the plasma treatment as shown in Fig. 3.12). Thus, the results proved that the addition of oxygen to the process gas can suppress the formation of the carbon deposit on a quartz crystal wafer. The relationship between the etching rate of the quartz crystal wafer and the oxygen flow rate is shown in Fig. 3.13. The carbon deposit disappeared with the addition of 4 sccm O_2. However, the etching rate decreased as the oxygen flow increased. It is considered that as the oxygen itself did not contribute to the etching reaction of the quartz crystal, and the generation of O and F radicals both require energy from argon in the active state, the competition between O_2 and CF_4 led to a decrease in etching rate at high oxygen fractions.

3.6.1 Shape of removal spot

Since the highest MRR can be obtained without carbon deposition, 4 sccm was considered the optimal oxygen flow rate. To investigate the difference between He and Ar-based CF_4 plasmas, a

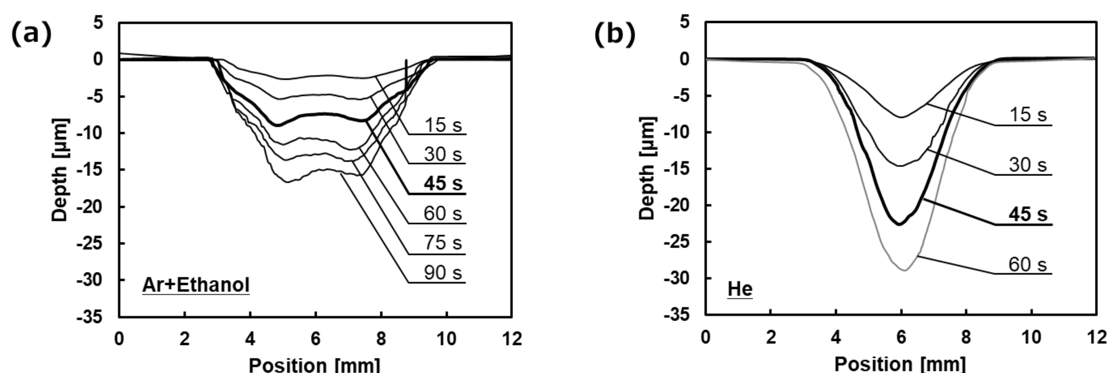

Figure 3.14 Cross-sectional profiles of removal spots formed on the quartz crystal wafers by AP-PCVM in different processing time using (a) ethanol-added Ar and (b) He as the carrier gas.

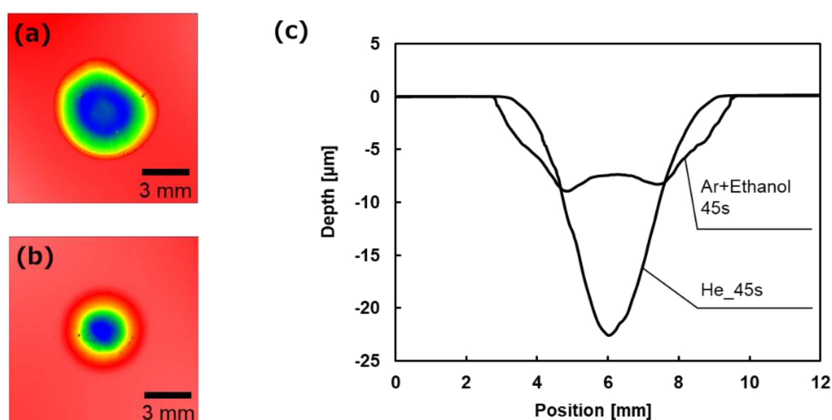

Figure 3.15 Scanning white-light interferometer (SWLI) images of the removal spots formed by AP-PCVM for 45 s using (a) ethanol-added Ar and (b) He as carrier gases as well as (c) comparison of their cross-sectional profiles.

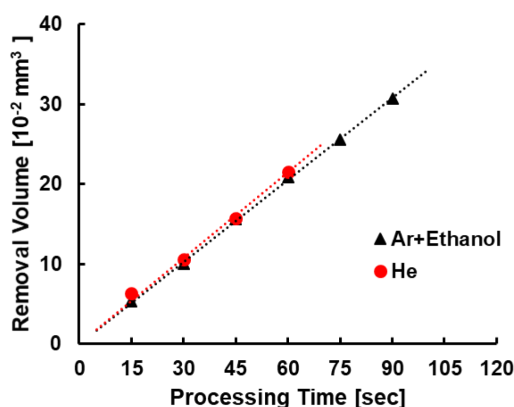

Figure 3.16 Relationship between processing time and removal volume of the removal spot formed by AP-PCVM (RF power: 60 W, ethanol: 0.003 g/min, carrier He/Ar: 600 sccm, CF_4: 10 sccm, O_2: 4 sccm).

comparative experiment was conducted. The RF power was 60 W and the ethanol flow rate was 0.003 g/min. The carrier gas was He/Ar (600 sccm) and the process gases were CF_4 (10 sccm) and O_2 (4 sccm). The processing time was 15–90 s. Figure 3.14 (a) and (b) show the cross-sectional profiles of removal spots formed on the quartz crystal wafers by AP-PCVM in different processing time using ethanol-added Ar and He as the carrier gas. As an example of them, scanning white-light interferometer (SWLI) images of the removal spots formed by etching for 45 s using He and ethanol-added Ar as carrier gases as well as comparison of their cross-sectional profiles were shown in Fig. 3.15 (a), (b), and (c). As He has a much lower mass than N_2, and Ar

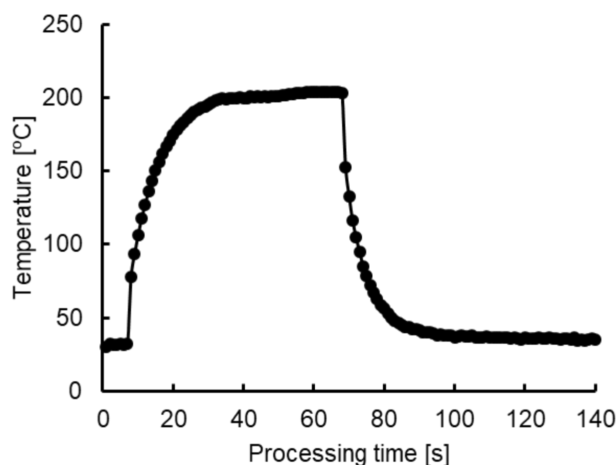

Figure 3.17 Processing temperature of the removal spot measured by infrared thermography.

has a higher mass than N_2. So, the area of plasma using ethanol-added Ar as the carrier gas is wider than that of using He as the carrier gas. The diameter of the removal spot formed using ethanol-added argon as the carrier gas was larger than that of the spot formed using He, but the maximum depth was lower. The relationship between the removal volume of the removal spots and the processing time is shown in Fig. 3.16. The removal volumes using He and ethanol-added Ar were almost the same for the same processing time. In addition, the removal volume was proportional to the processing time in both cases. The results above show that, using ethanol-added Ar as the carrier gas in AP-PCVM instead of He, the same etching rate is obtained, and the operation cost is reduced. In addition, in our previous research, it has been proved that if the temperature of processing point exceeded 200ºC, crystal twinning will occurred easily. Figure 3.17 shows the processing temperature of the removal spot processed by AP-PCVM using ethanol-added Ar as the carrier gas for 60 s, measured by infrared thermography. The temperature of the processing spot increased with the increase of processing time and was saturated at about 200ºC, which was considered that there was no risk of occurrence of crystal twinning under this processing condition.

3.6.2 Etching rate

From the above, ethanol-added Ar has been used as the carrier gas instead of He to generate a stable glow plasma and obtained the same etching rate. In the actual production process, to realize quartz crystal wafers with high thickness uniformity, plasma is used for raster scan processing by controlling the dwell time rather than stationary point processing. Thus, it is necessary to define the relationship between the removal volume and the scanning speed of the plasma. Line scan experiments were conducted on a quartz crystal wafer. The RF power was 60 W and the ethanol flow rate was 0.003 g/min. The carrier gas was He/Ar (600 sccm) and the process gases were CF_4

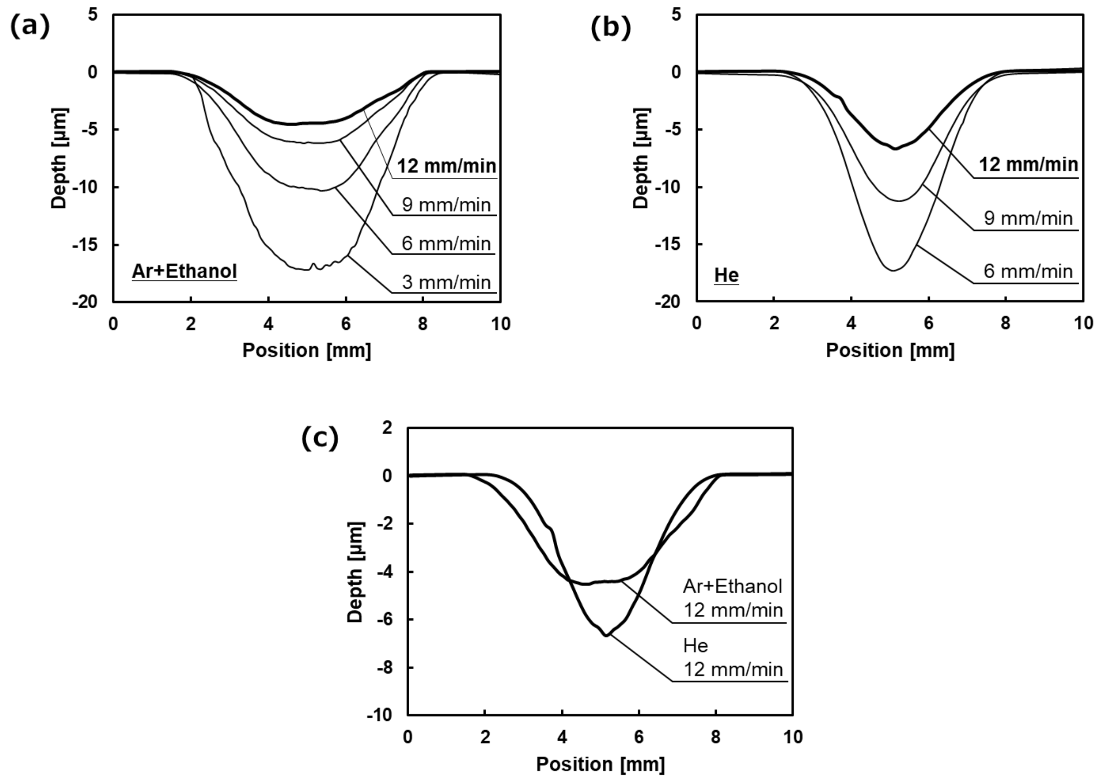

Figure 3.18 Cross-sectional profiles of grooves formed by AP-PCVM on quartz crystal wafers in different scanning speeds. (a) Ethanol-added argon as the carrier gas. (b) Helium as the carrier gas. (c) Comparison of cross-sectional profiles of the grooves formed by etching with the scanning speed of 12 mm/min.

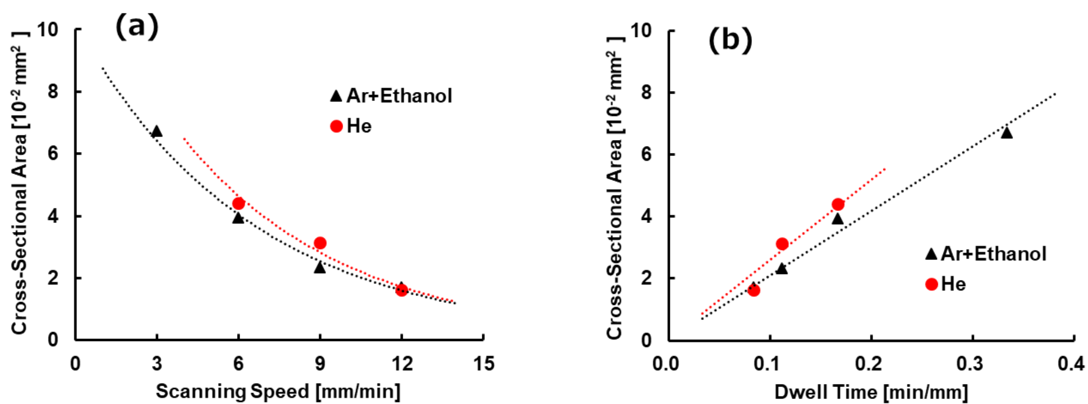

Figure 3.19 Relationship between scanning speed (a) or dwell time (b) and cross-sectional area of the etched groove formed by AP-PCVM (RF power: 60 W, ethanol: 0.003 g/min, carrier He/Ar: 600 sccm, CF_4: 10 sccm, O_2: 4 sccm).

(10 sccm) and O_2 (4 sccm). The scanning speed was 3, 6, 9, and 12 mm/min. Figure 3.18 (a) and 3.18(b) show the cross-sectional profiles of the grooves formed on the quartz crystal wafer during AP-PCVM in different scanning speed using ethanol-added Ar and He as the carrier gas. And comparison of cross-sectional profiles of the grooves formed by etching with the scanning speed of 12 mm/min using ethanol-added Ar and He as carrier gases was shown in Fig. 3.18 (c). In the case of formation of the removal spot using ethanol-added Ar, the central cross-sectional shape of the removal spot was complicated as shown in Fig. 3.15. However, in the case of line scan experiment, the cross-sectional shape of the grooves formed by AP-PCVM using ethanol-added argon and helium both became smooth due to the integration of the removal spot shape along the scanning direction. Removal rate was evaluated by calculation of the cross-sectional area of the groove. Figure 3.19 (a) shows the relationship between the scanning speed and the cross-sectional area of the groove formed on the quartz crystal wafer by a line scan during AP-PCVM. This result shows that the cross-sectional area correlates with the scanning speed. Since the reciprocal of the scanning speed is the dwell time of plasma, the relationship between the dwell time and the cross-sectional area of the groove is shown in Fig. 3.19 (b). The cross-sectional area of the groove was proportional to the dwell time of plasma. In our previous research, AP-PCVM using helium as a carrier gas has been confirmed to be able to obtain quartz crystal wafers with high thickness uniformity [1, 7]. From the above results, similar cross-sectional shape of grooves was obtained during AP-PCVM using helium and ethanol-added argon as the carrier gas. Therefore, in AP-PCVM using ethanol-added argon to substitute helium as the carrier gas, it is possible to realize quartz crystal wafers with high thickness uniformity by controlling the scanning speed in accordance with this relationship [29].

3.7 Summary

As a part of plasma nanomanufacturing process, AP-PCVM has been successfully applied to improve the thickness uniformity of ultrathin quartz crystal wafer in the previous study. Helium, a gas with high cost and unstable supply, has been used as the carrier gas in AP-PCVM till date. Although argon, which is a low cost and is easier to manufacture from liquid air, is also commonly used in vacuum plasma as the carrier gas, the breakdown voltage of Ar at AP is about 7300 V, which is much higher than that of He (about 3000 V) [83]. Since the high breakdown voltage for argon at atmospheric pressure easily leads to the formation of filamentary arc streamers, which can break a quartz crystal wafer, argon has not been used in AP-PCVM as the carrier gas to correct the thickness distribution of a quartz crystal wafer until now. In this chapter, it was confirmed that the plasma can be stabilized by adding a small fraction of ethanol into Ar, and the etching characteristics of ultrathin quartz crystal wafer by AP-PCVM using ethanol-added Ar as the

carrier gas were investigated.

(1) The difference between He plasma and Ar plasma at AP was well explained using Penning effect. The addition of a small fraction of ethanol to Ar can generate atmospheric-pressure plasma with a stable glow discharge state instead of arc streamers due to the Penning effect between metastable states Ar atoms and ethanol molecular.

(2) The etching characteristics of ultrathin quartz crystal wafer obtained by AP-PCVM using ethanol-added Ar-based atmospheric-pressure CF_4 plasma were investigated. Due to the incompletely decomposed carbon from ethanol, a large amount of carbon deposit was formed on quartz crystal wafer after AP-PCVM using ethanol-added Ar as the carrier gas. The experimental results proved that the addition of oxygen into the process gas can suppress the formation of the carbon deposit.

(3) Since oxygen itself did not contribute to the etching reaction of the quartz crystal, and the generation of O and F radicals both require the energy from Ar in the active state, the competition between O_2 and CF_4 led to a decrease in etching rate at high oxygen fractions. An O_2 flow rate of 4 sccm is suitable because a high etching rate can be obtained without carbon deposition.

(4) Comparative experiments were conducted on ultrathin quartz crystal wafers in AP-PCVM using He and ethanol-added Ar as the carrier gas (the other experimental conditions were same). Since He has a much lower mass than air, and Ar has a higher mass than air, so the area of plasma using ethanol-added Ar as the carrier gas was wider than that of He as the carrier gas. The diameter of the removal spot formed using ethanol-added Ar as the carrier gas was larger than that of the spot formed using He, but the maximum depth was lower. However, the volumetric removal rate using He and ethanol-added Ar were almost the same.

(5) Since the same etching rate was obtained using He or ethanol-added Ar as the carrier gas in AP-PCVM, and the removal volume was proportional to the processing time in both cases. Hence, it is considered that using argon instead of helium as the carrier gas in AP-PCVM will effectively solve problems such as the depletion of natural resources and high cost.

References

1) K. Yamamura, S. Shimada, Y. Mori, Damage-free improvement of thickness uniformity of quartz

crystal wafer by plasma chemical vaporization machining, *CIRP Annals – Manufacturing Technology*. **57** (2008) 567-570.

2) R. Sun, X. Yang, Y. Ohkubo, K. Endo, K. Yamamura, Optimization of gas composition used in plasma chemical vaporization machining for figuring of reaction-sintered silicon carbide with low surface roughness, *Scientific Reports.* **8** (2018) 2376.

3) Y. Mori, K. Yamauchi, K. Yamamura, Y. Sano, Development of plasma chemical vaporization machining, *Review of Scientific Instruments.* **71** (2000) 4627-4632.

4) N. Yu, R. Jourdain, M. Gourma, P. Shore, Analysis of De-Laval nozzle designs employed for plasma figuring of surfaces, *The International Journal of Advanced Manufacturing Technology.* **87** (2016) 735-745.

5) M. Castelli, R. Jourdain, P. Morantz, P. Shore, *Rapid optical surface figuring using reactive atom plasma, Precision Engineering*. **36** (2012) 467-476.

6) P. Piechulla, J. Bauer, G. Boehm, H. Paetzelt, T. Arnold, Etch mechanism and temperature regimes of an atmospheric pressure chlorine-based plasma jet process, *Plasma Processes and Polymers.* **13** (2016) 1128-1135.

7) K. Yamamura, M. Ueda, M. Shibahara, N. Zettsu, Finishing of AT-cut quartz crystal wafer with nanometric thickness uniformity by pulse-modulated atmospheric pressure plasma etching, *Journal of Nanoscience and Nanotechnology.* **11** (2011) 2922-2927.

8) https://ele.kyocera.com/ja/technical/358441/

9) *Helium Stewardship Act of 2013*, https://www.energy.senate.gov/services/files

10) A. Schutze, J. Y. Jeong, S. E. Babayan, *et al.*, The atmospheric-pressure plasma jet: A review and comparison to other plasma sources, *IEEE Transactions on Plasma Science.* **26** (1998) 1685-1694.

11) J. Park, I. Henins, H. W. Herrmann, *et al.*, Discharge phenomena of an atmospheric pressure radio-frequency capacitive plasma source, *Journal of Applied Physics.* **89** (2001) 20-28.

12) W. Sun, G. Li, H. Li, *et al.*, Characteristics of atmospheric-pressure, radio-frequency glow discharges operated with argon added ethanol, *Journal of Applied Physics.* **101** (2007) 123302.

13) A. A. Kruithof, F. M. Penning, Determination of the townsend ionization coefficient α for pure argon, *Physica.* **3** (1936) 515-533.

14) H. Sugai, Inter university – Plasma electronics, *Ohmsha*, 2016.

15) A. A. Kruithof, F. M. Penning, Determination of the townsend ionization coefficient α for mixtures of neon and argon, *Physica.* **4** (1937) 430-449.

16) X. Shao, N. Jiang, G. Zhang, *et al.*, Comparative study on the atmospheric pressure plasma jets of helium and argon, *Applied Physics Letters.* **101** (2012) 253509.

17) F. Tochikubo, Z. L. Petrovic, S. Kakuta, *et al.*, Influence of Ar metastable on the discharge structure in Ar and N2 mixture in RF discharges at 13.56 MHz, *Japanese Journal of Applied Physics*. **33** (1994) 4271-4275.

18) H. Barankova, L. Bardos, S. Berg, Metastable assisted deposition of TiN films, *Applied Physics Letters*. **67** (1995) 1521-1523.
19) A. A. Radzig, B. M. Smirnov, Reference data on atoms, molecules, and ions, *Springer-Verlag* (1985).
20) W. Xia, D. Liu, H. Xu, *et al.*, The effect of ethanol gas impurity on the discharge mode and discharge products of argon plasma jet at atmospheric pressure, *Plasma Sources Science and Technology*. **27** (2018) 055001.
21) T. Vandevelde, T. D. Wu, C. Quaeyhaegens, *et al.*, Correlation between the OES plasma composition and the diamond film properties during microwave PA-CVD with nitrogen addition, *Thin Solid Film*. **340** (1999) 159-163.
22) O. Flores, F. Castillo, H. Martinez, *et al.*, Characterization of direct current He-N2 mixture plasma using optical emission spectroscopy and mass spectrometry, *Physics of Plasma.* **21** (2014) 053502.
23) U. Cvelbar, N. Krstulovic, S. Milosevic, M. Mozetic, Inductively coupled RF oxygen plasma characterization by optical emission spectroscopy, *Vacuum*. **82** (2008) 224-227.
24) C. Teng, C. M. Ma, C. Lu, *et al.*, Thermal conductivity and structure of non-covalent functionalized graphene/epoxy composites, *Carbon.* **49** (2011) 5107-5116.
25) P. Ren, D. Yan, X. Ji, *et al.*, Temperature dependence of graphene oxide reduced by hydrazine hydrate, *Nanotechnology.* **22** (2011) 055705.
26) C. H. Lucas, A. J. L. Peinado, J. D. L. Gonzalez, *et al.*, Study of oxygen-containing groups in a series of graphite oxides: Physical and chemical characterization, *Carbon.* **33** (1995) 1585-1592.
27) M. Jimenez, R. Rincon, A. Marinas, M. D. Calzada, Hydrogen production from ethanol decomposition by a microwave plasma: Influence of the plasma gas flow, *International Journal of Hydrogen Energy.* **38** (2013) 8708-8719.
28) G. Faggio, A. Capasso, G. Messina, *et al.*, High-temperature growth of graphene films on copper foils by ethanol chemical vapor deposition, *The Journal of Physical Chemistry C.* **117** (2013) 21569-21576.
29) R. Sun, X. Yang, K. Watanabe, *et al.*, Etching characteristics of quartz crystal wafers using argon-based atmospheric pressure CF_4 plasma stabilized by ethanol addition, *Nanomanufacturing and Metrology.* **2** (2019) 168-176.

Chapter 4

Application of plasma nanomanufacturing process to RS-SiC

4.1 Introduction

PCVM and PAP have been successfully applied to the processing of a variety of single-crystal materials. However, both PCVM and PAP are based on chemical reactions. Due to the reactive species generated by plasma have different reaction rate with different materials, it is difficult for PCVM and PAP to be applied to multicomponent materials so far. In this chapter, through the optimization of processing parameters, plasma nanomanufacturing process, which combines PCVM with PAP, was applied to the processing of a multicomponent material (RS-SiC) and obtained a smooth surface.

4.2 Figuring of RS-SiC by AP-PCVM

As introduced in section 1.2.2, SiC, as the main component of RS-SiC, gives RS-SiC many excellent properties, such as low density, high hardness, high thermal conductivity, low thermal expansion coefficient, chemical inertness, and so on. In addition, compared with single-crystal SiC, the production cost of RS-SiC is relatively low. Therefore, RS-SiC is considered an ideal material for optical mirror devices in space telescope systems, or molds for optical components. In order to meet the application requirements, ultrasmooth surface of RS-SiC is required, and AP-PCVM is considered to be an appropriate method to remove the damage layer formed during the preliminary mechanical figuring process, and to further improve the shape accuracy.

4.2.1 Microwave AP-PCVM setup used in this work

In Chapter 3, since the possibility of both crystal twinning and breaking of the quartz crystal wafer increases if the temperature of processing area exceeding 200℃, capacitively coupled plasma, which has a relatively low temperature, was used. Unlike quartz crystal wafer, RS-SiC will not be broken due to the high temperature of the plasma. On the contrary, higher MRR can be obtained at a higher temperature. Furthermore, using pure argon as the carrier gas without adding ethanol can also generate a stable microwave plasma. Therefore, in this chapter, microwave plasma is selected in AP-PCVM for processing of RS-SiC. Figure 4.1 shows the conceptual diagram of the microwave AP-PCVM setup. The microwave AP-PCVM experimental setup used in this work is laboratory-

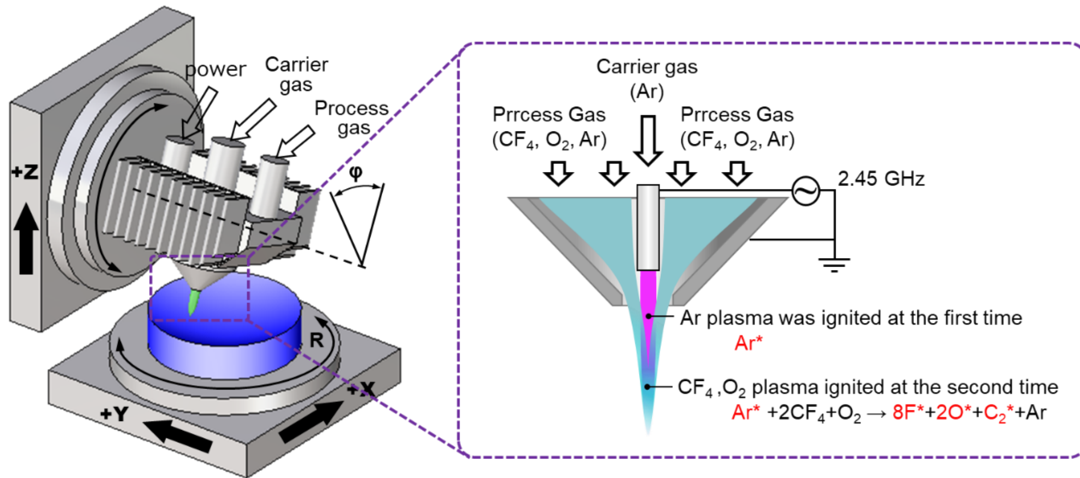

Figure 4.1 Schematic diagram of the microwave AP-PCVM setup.

built. The main part of the setup comprises a CNC machine equipped with an x-y-z-table, a microwave power supply unit (Nagano. JRC, NJW-143), a gas supply system for plasma generation and a plasma generator (Nagano. JRC, NJW-144). As an important part of micro AP-PCVM setup, the internal schematic diagram of the plasma generator is also shown in Fig. 4.1. Argon (Ar) gas was supplied as a carrier gas into the ceramic tube installed at the center of the plasma generator, which was surrounded by a cavity resonator. A microwave electric field with a frequency of 2.45 GHz was applied to generate an electric field whose maximum intensity was near the tip of the ceramic tube, where the Ar atoms were ionized and atomic radicals were generated. The Ar plasma was ignited at the first time. Simultaneously, Ar, CF_4, and O_2 were supplied as the process gases from another gas inlet offset from the center. At this time, collisions occurred between argon in the active state originating from the center of the plasma generator and Ar, CF_4, and O_2 in the ground state. As a result of the collisions, F radicals and O radicals, which contributed to etching, were generated at the second time. The reason why the CF_4 was ionized at the second time but not ionized directly by the microwave electric field is that the F radicals are very reactive, and would have corroded the ceramic tube, decreasing its lifetime, and contamination due to the precipitation of substances originating from the etched ceramic tube would have interfered with the etching process. The gas flow rate of Ar, CF_4, and O_2 was controlled by mass flow controllers (MFCs).

4.2.2 Processing gap

As shown in Fig. 4.2, in AP-PCVM process, the distance between the outlet of plasma generator and substrate was defined as processing gap. As one of the important processing parameters in AP-PCVM process, the processing gap has a great influence on the etching characteristics of AP-PCVM. Figure 4.3 shows the SWLI images and cross section of the removal spots processed

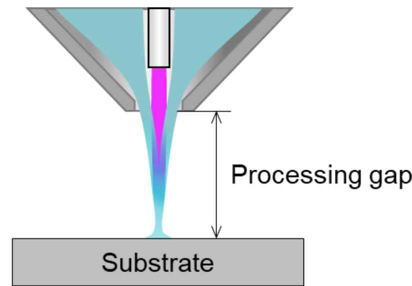

Figure 4.2 Definition of processing gap in AP-PCVM.

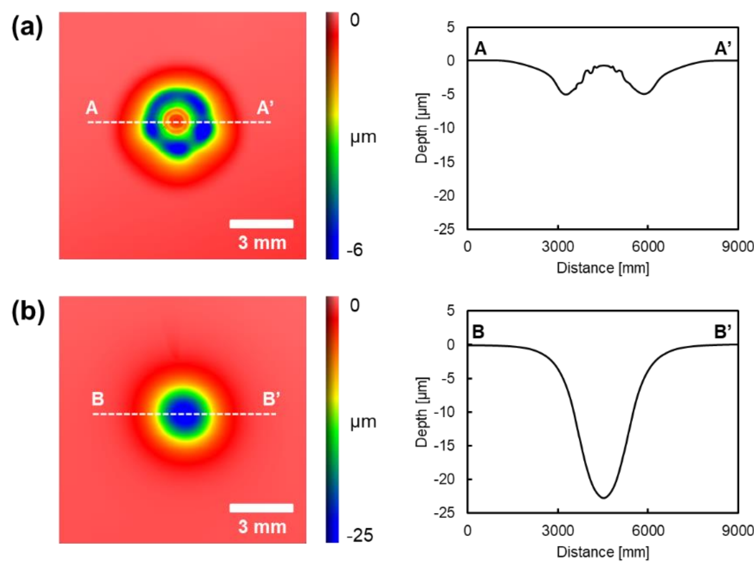

Figure 4.3 SWLI images and cross section of the removal spot processed under the same processing conditions except processing gap (a) Gap 2 mm, (b) Gap 6 mm.

under the same processing conditions except processing gap for 5 s. When the processing gap was 2 mm, a shallow ring-shaped removal spot was obtained. However, when the processing gap was 6 mm, a deep Gaussian-shaped removal spot was obtained. To elucidate the relationship between etching characteristics and processing gap in AP-PCVM, the mixed state of the gases used in AP-PCVM was simulated using ANSYS computational fluid dynamics (CFD) simulation.

4.2.2.1 Analysis of gas component distribution in different processing gap using computational fluid dynamics simulation

As shown in Fig. 4.1, the carrier gas was supplied from the ceramic tube installed at the center of the plasma generator. However, the process gas was supplied from the other gas inlet offset from the ceramic tube and mixed with the carrier gas nearby the outlet of the plasma generator. Thus, it

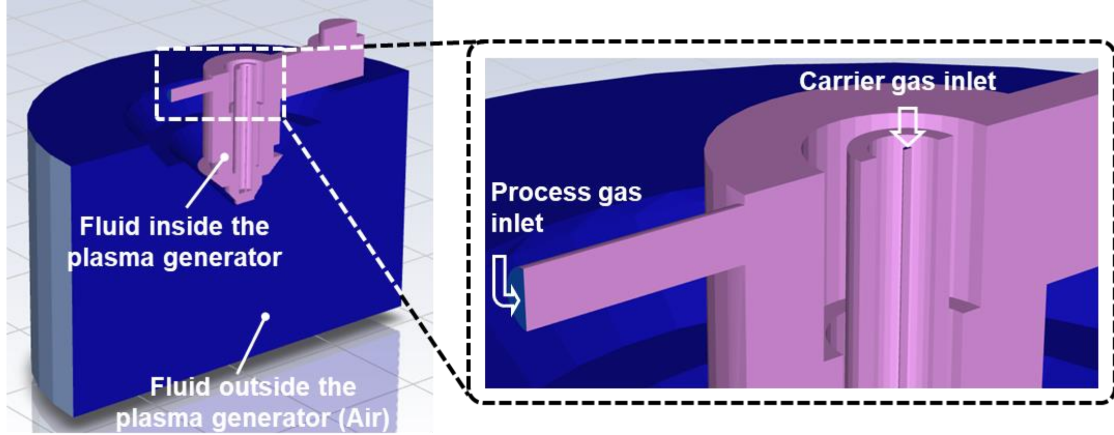

Figure 4.4 Schematic diagram of the model used in CFD simulation.

is considered that the mixing state of the mixture gases (carrier gas and process gas) was changed with the distance from the outlet of plasma generator (processing gap). To analyze the distribution of the mixture gases in different processing gap, CFD simulation was conducted using ANSYS. Figure 4.4 shows the fluid model used in CFD simulation. The fluid model contained two parts: fluid inside and outside (air) of the plasma generator. The inlet diameter of the carrier gas (Ar: 500 sccm) was ϕ 0.5 mm, and the inlet diameter of the process gas (Ar: 1000 sccm, CF_4: 10 sccm, O_2: 90 sccm) was ϕ 3.0 mm. Before the CFD simulation, the fluid situation should be confirmed by the Reynolds number (*Re*)

$$Re = \frac{\rho u L}{\mu} \tag{4-1}$$

where ρ is the density of the fluid (kg/m^3), u is the flow velocity (m/s), L is a characteristic linear dimension (diameter of the pipe, m), and μ is the dynamic viscosity of the fluid (Pa･s). At low *Re* (< 2100), flows tend to be dominated by laminar flow, while at high *Re* (> 4000) flows tend to be turbulent [1)]. Since Ar was the main component in the fluid model for CFD simulation, the *Re* of the fluid was approximated calculated using the physical characteristics value of Ar:

$$Re_{\text{fluid}} = \frac{\rho u L}{\mu} = \frac{1.4 \times 10.6 \times 0.5 \times 10^{-3}}{22.9 \times 10^{-6}} = 324 \tag{4-2}$$

Since Re_{fluid} < 2100, the fluid model used in this work was considered to laminar flow. In CFD simulation this time, the density of the mixture gas was defined using the ideal gas law for an incompressible flow, the slover computed the density ρ as

$$\rho = \frac{p_{\text{op}}}{\frac{R}{M_{\text{w}}} T} \tag{4-3}$$

where R is the universal gas constant, M_{w} is the molecular weight of the gas, and p_{op} is the operating pressure. Since the mixture flow included more than one chemical species, the specific heat capacity C_{p} of the mixture gas was computed as a mass fraction average of the pure species heat capacities

$$C_{\mathrm{p}} = \sum_{i} Y_{\mathrm{i}} c_{\mathrm{p,i}} \tag{4-4}$$

where Y_{i} is the local mass fraction of each species. As described above that the ideal gas law was used, thus the solver computed the thermal conductivity k and viscosity μ based on Kinetic theory as

$$k = \sum_{i} \frac{X_{\mathrm{i}} k_{\mathrm{i}}}{\sum_{\mathrm{j}} X_{\mathrm{j}} \phi_{\mathrm{ij}}} \qquad \mu = \sum_{i} \frac{X_{\mathrm{i}} k_{\mathrm{i}}}{\sum_{\mathrm{j}} X_{\mathrm{j}} \phi_{\mathrm{ij}}} \qquad \text{(4-6) (4-7)}$$

where

$$\phi_{\mathrm{ij}} = \frac{\left[1 + \left(\frac{\mu_{\mathrm{i}}}{\mu_{\mathrm{j}}}\right)^{1/2} \left(\frac{M_{\mathrm{w,j}}}{M_{\mathrm{w,i}}}\right)^{1/4}\right]^{2}}{\left[8\left(1 + \frac{M_{\mathrm{w,i}}}{M_{\mathrm{w,j}}}\right)\right]^{1/2}} \tag{4-8}$$

and X_{i} is the mole fraction of species i. Mass diffusion coefficients are required whenever solving species transport equations in multicomponent flows. Mass diffusion coefficients are used to compute the diffusion flux J_{i} of a chemical species in a laminar flow using Fick's law:

$$J_{\mathrm{i}} = -\rho D_{\mathrm{i,m}} \nabla Y_{\mathrm{i}} - D_{\mathrm{T,i}} \frac{\nabla T}{T} \tag{4-9}$$

where $D_{\mathrm{i,m}}$ is the mass diffusion coefficient for species *i* in the mixture and $D_{T,i}$ is the thermal diffusion coefficient. $D_{\mathrm{i,m}}$ can be specified in a variety of ways, including by specifying D_{ij}, the binary mass diffusion coefficient of component i in component j.

$$D_{\mathrm{i,m}} = \frac{1 - X_{\mathrm{i}}}{\sum_{\mathrm{j,j \neq i}} \left(X_{\mathrm{j}} / D_{\mathrm{ij}}\right)} \tag{4-10}$$

The solver used a modification of the Chapman–Enskog formula [2)] to compute the diffusion coefficient D_{ij} using kinetic theory:

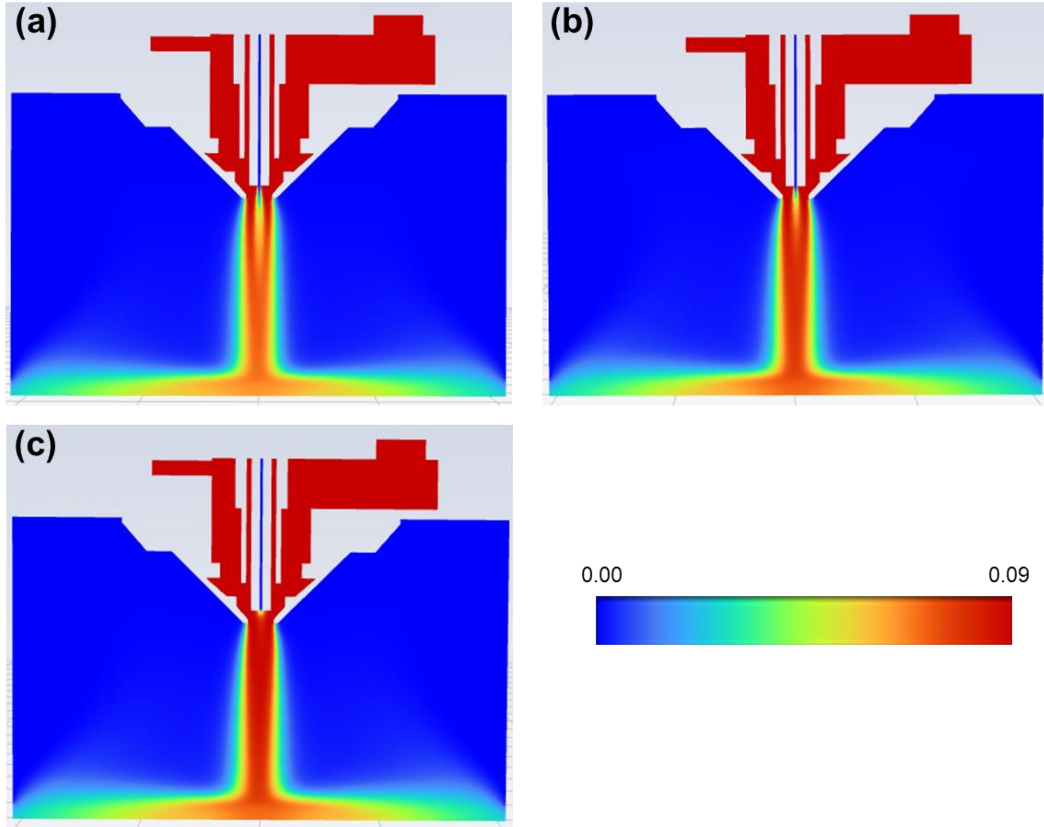

Figure 4.5 Mole fraction distribution result of CF_4 under carrier gas inlet temperature of (a) 300 K, (b) 773 K, and (c) 5273 K.

$$D_{\mathrm{ij}} = 0.00188 \frac{\left[T^3\left(\frac{1}{M_{\mathrm{w,i}}}+\frac{1}{M_{\mathrm{w,j}}}\right)\right]^{1/2}}{p_{\mathrm{abs}}\sigma_{\mathrm{ij}}^2 \Omega_{\mathrm{D}}} \tag{4-11}$$

where p_{abs} is the absolute pressure, and Ω_{D} is the diffusion collision integral, which is a measure of the interaction of the molecules in the system.

And the thermal diffusion coefficient $D_{\mathrm{T,i}}$ was defined using the following empirically-based composition-dependent expression derived from [3)]

$$D_{\mathrm{T,i}} = -2.59 \times 10^7 T^{0.659} \left[\frac{M_{\mathrm{w,i}}^{0.511} X_{\mathrm{i}}}{\sum_{i=1}^{N} M_{\mathrm{w,i}}^{0.511} X_{\mathrm{i}}} - Y_i\right] \cdot \left[\frac{\sum_{i=1}^{\mathrm{N}} M_{\mathrm{w,i}}^{0.511} X_{\mathrm{i}}}{\sum_{i=1}^{N} M_{\mathrm{w,i}}^{0.489} X_{\mathrm{i}}}\right] \tag{4-12}$$

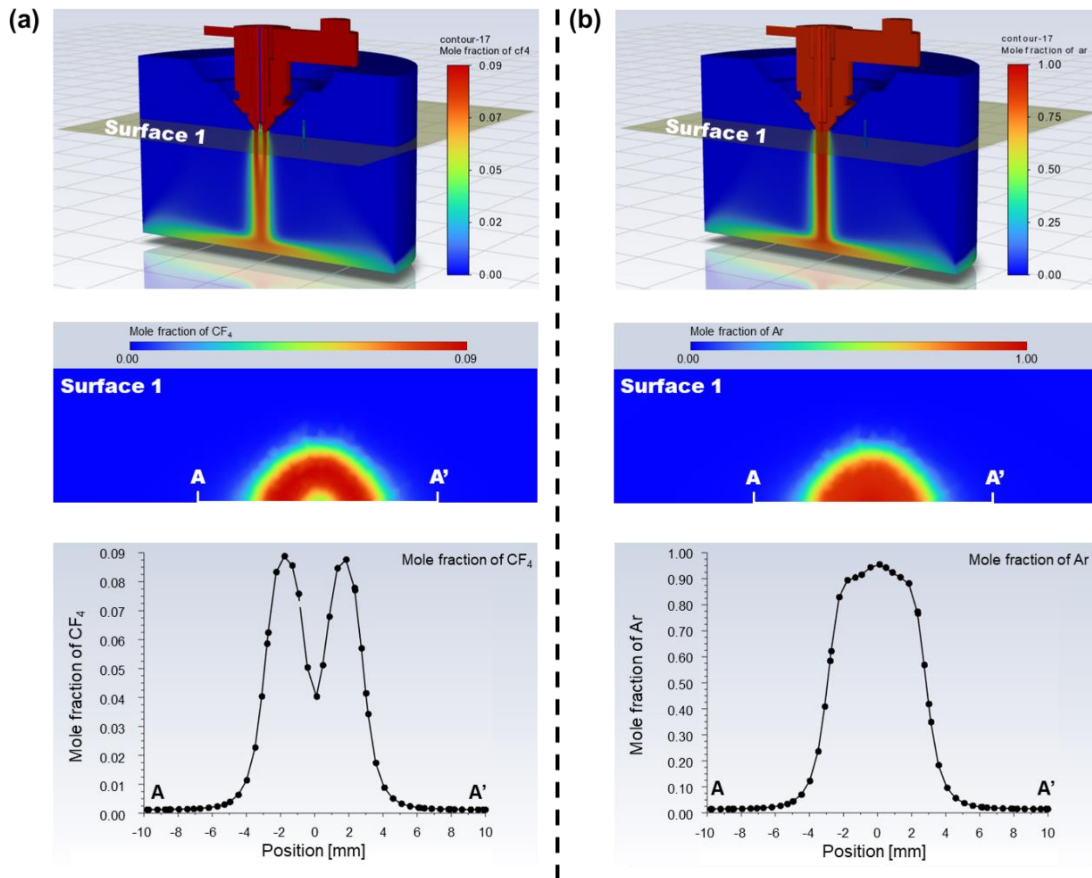

Figure 4.6 Mole fraction distribution of (a) CF_4 and (b) Ar on the surface 1 (processing gap = 2 mm) and the cross section of A-A' when the inlet temperature of carrier gas was set at 300 K.

Since both mass diffusion coefficient $D_{\mathrm{i,m}}$ and the thermal diffusion coefficient $D_{\mathrm{T,i}}$ change with temperature, the diffusion rate of each specie is greatly affected by temperature. Figure 4.5 shows the mole fraction distribution result of CF_4 under different carrier gas inlet temperature. The inlet temperature of process gas was set at 300 K, and the inlet temperature of carrier gas was set at 300 K, 773 K, and 5273 K, respectively. As shown in Fig. 4.5(a), after ejecting from the ceramic tube, the carrier gas Ar began to diffuse and mix with the process gases (Ar, CF_4, and O_2), which was introduced around it. In the initial stage of mixing, CF_4 was mainly distributed on the periphery of gas flow. A certain distance was needed to make CF_4 diffuse to the center and mix well with the carrier Ar gas. As the inlet temperature of the carrier gas increased, the diffusion rate of mixture gas also increased, and the distance needed for well mixing became shorter. Figure 4.6 shows the mole fraction distribution of CF_4 and Ar on the surface 1 (processing gap = 2 mm) and the cross section of A-A' when the inlet temperature of carrier gas was set at 300 K. Since CF_4 has not been fully diffused and mixed with Ar in such a short distance from the outlet of the

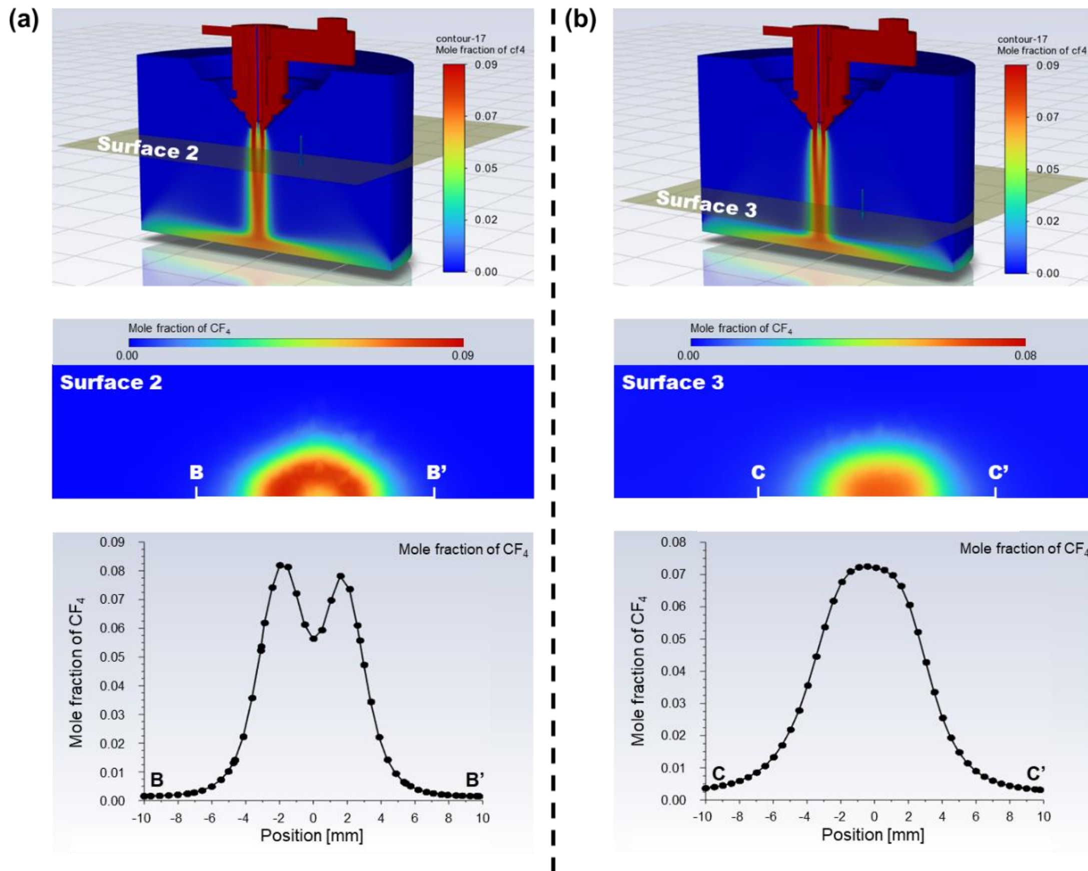

Figure 4.7 Mole fraction distribution of CF_4 (a) on the surface 2 (processing gap = 6 mm) and the cross section of B-B', (b) on the surface 3 (processing gap = 24 mm) and the cross section of C-C' when the inlet temperature of carrier gas was set at 300 K.

plasma generator, the distribution of CF_4 was ring-shaped on surface 1 (processing gap = 2). Although Ar was more distributed in the center position, Ar did not have the ability to etch, so the removal volume in the center was very small. Since F radicals generated from the decomposition of CF_4 contributed to the etching process in AP-PCVM, the shape of the distribution of CF_4 in CFD simulation presented the same ring shape as the removal spot experimentally obtained in AP-PCVM at processing gap of 2 mm as shown in Fig. 4.3(a). However, when the processing gap = 6 mm, the simulation result and the actual processing result did not match. As shown in Fig. 4.3(b), when the processing gap was 6 mm, a Gaussian-shaped removal spot was formed, which was considered that CF_4 has been well diffused and mixed with the carrier gas at the processing gap of 6 mm. However, from the CFD simulation result, on the surface 2 with a processing gap of 6 mm, the distribution of CF_4 still shows a ring-shaped distribution as shown in Fig. 4.7(a). And CF_4 did not well mix with carrier Ar until the processing gap reached 24 mm, as shown in Fig. 4.7(b). As shown in the schematic diagram of the plasma

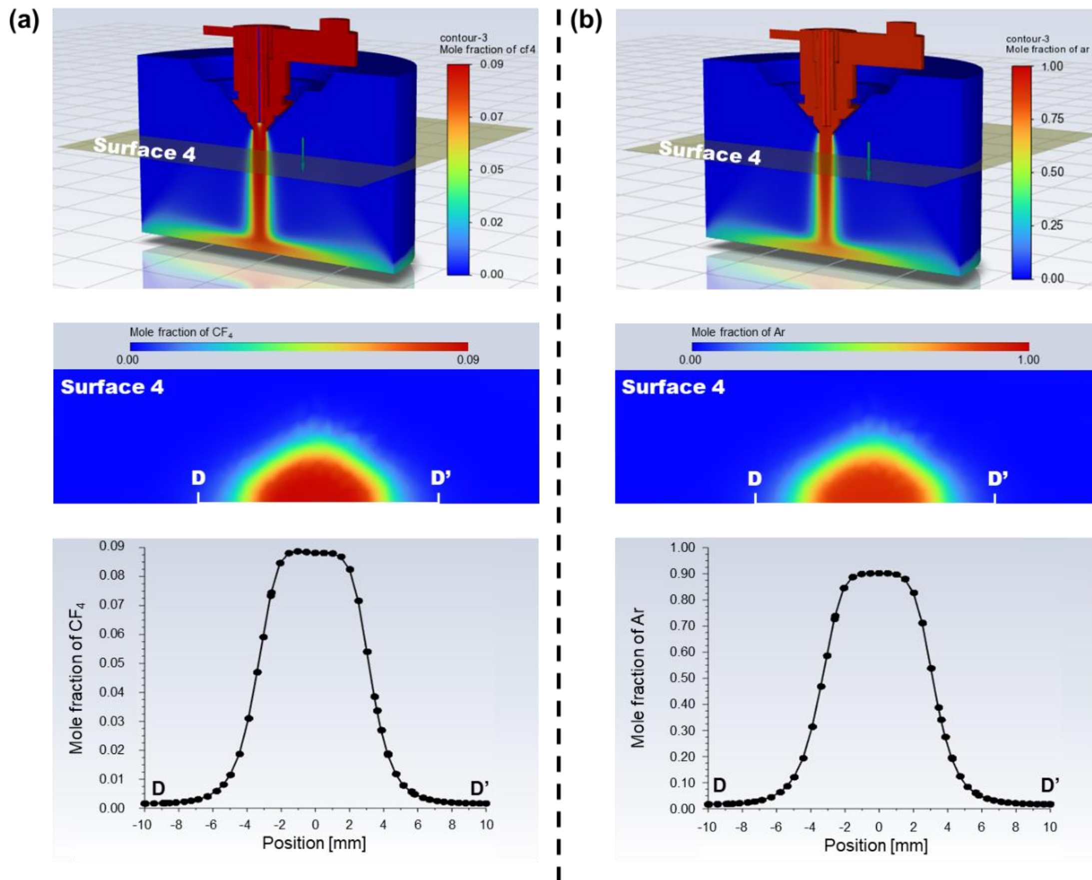

Figure 4.8 Mole fraction distribution of (a) CF_4 and (b) Ar on the surface 4 (processing gap = 6 mm) and the cross section of D-D' when the inlet temperature of carrier gas was set at 5273 K.

generator in Fig. 4.1, a microwave electric field with a frequency of 2.45 GHz was applied on ceramic tube to generate Ar plasma at the first time, the temperature of carrier Ar gas was increased due to plasma heating. Figure 4.8 shows the mole fraction distribution of CF_4 and Ar on the surface 4 (processing gap = 6 mm) and the cross section of D-D' when the inlet temperature of carrier gas was set at 5273 K. Different from the CFD simulation result where the carrier gas inlet temperature was 300 K, when the inlet temperature was set at 5273K, the gas diffusion rate was greatly increased due to the increase of temperature. At the same position where the processing gap was 6 mm, CF_4 and Ar have been well mixed, instead of showing a ring-shaped distribution, which matched with the actual AP-PCVM processing result as shown in Fig. 4.3(b). Therefore, inside of the plasma generator, the temperature of the Ar plasma, which was ignited at the first time, was about 5273 K but not 300 K. Although the diffusion rate of gas increased greatly at high temperature, CF_4 still presented a ring-shaped distribution at the position where was too close to the outlet of ceramics tube as shown in Fig. 4.9. The above CFD simulation and

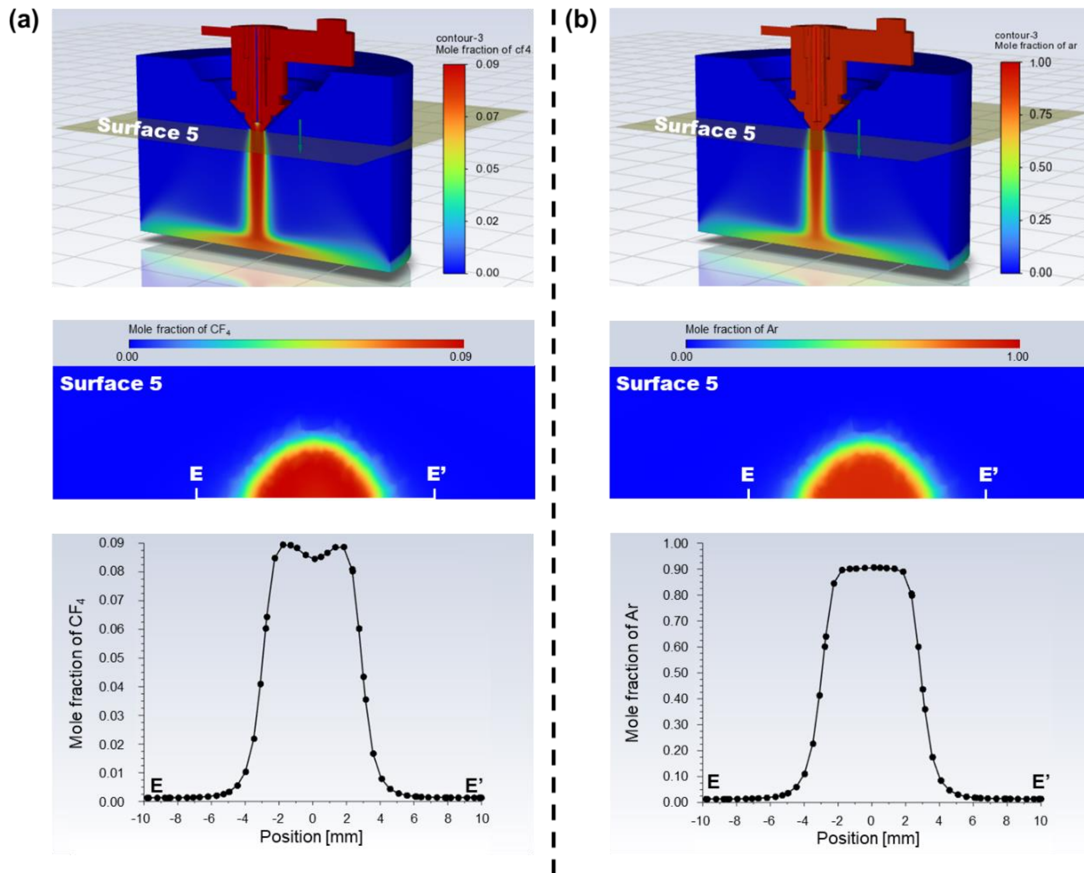

Figure 4.9 Mole fraction distribution of (a) CF_4 and (b) Ar on the surface 5 (processing gap = 2 mm) and the cross section of D-D’ when the inlet temperature of carrier gas was set at 5273 K.

AP-PCVM experimental results have confirmed that a certain processing gap was necessary to get a removal spot with a good shape like a Gaussian-shape.

4.2.2.2 Relationship between processing gap and etching rate

The relationship between processing gap and the shape of removal spot was discussed in the above section. In this section, the relationship between processing gap and etching rate will be investigated. Figure 4.10 shows the mole fraction distribution of CF_4 (a) and Ar (b) on the center line F-F’ obtained through CFD simulation when the inlet temperature of carrier gas was set at 5273 K. As the processing gap increased, more CF_4 diffused to the center region, where can be dissociated by Ar plasma (dissociated firstly using carrier Ar gas) and generate F radicals. Thus, the etching rate is considered to increase as the processing gap increased. After reaching to the maximum value, since CF_4 also diffused to the surroundings, the mole fraction of CF_4 began to decrease as the processing gap further increased. For the same reason, the mole fraction of Ar at the center region

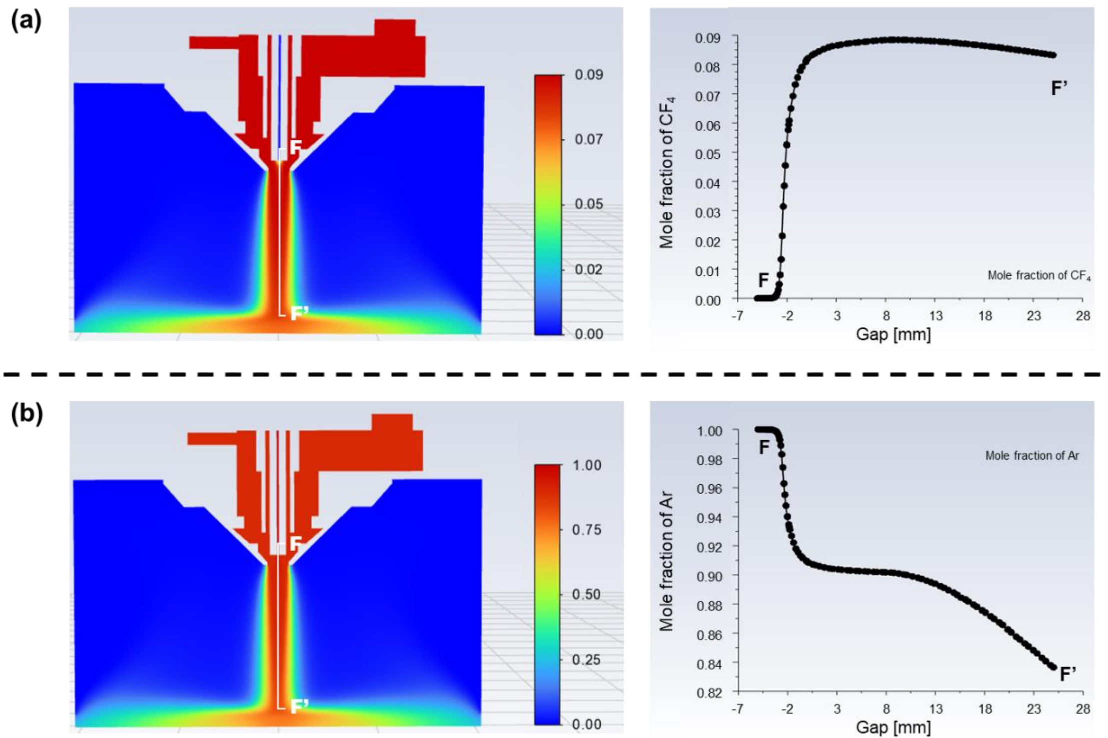

Figure 4.10 Mole fraction distribution of (a) CF_4 and (b) Ar on the center line F-F' obtained from CFD simulation when the inlet temperature of carrier gas was set at 5273 K..

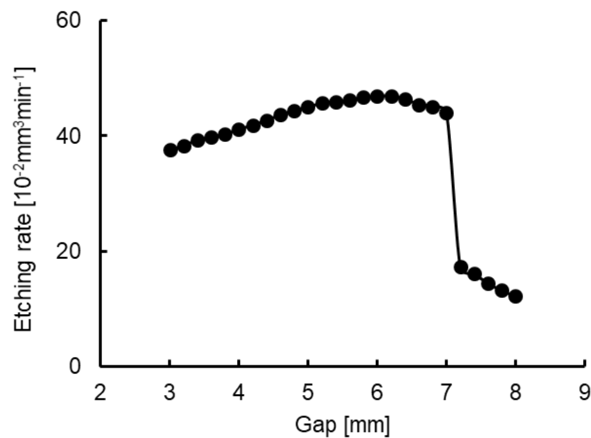

Figure 4.11 Relationship between processing gap and etching rate in AP-PCVM.

also decreased as the processing gap increased. In addition, the life of the excited Ar atom, which was the energy source of CF_4 plasma, was limited. When the processing gap became too large, excited Ar atoms lost their energy during the collision and returned to the ground state and cannot dissociate CF_4. Therefore, as the processing gap increased, the etching rate is considered to decrease

after reaching a peak value at a certain gap. A similar experimental result was obtained through AP-PCVM under different processing gap (3 ~ 8 mm) as shown in Fig. 4.11. From the above results, 6 mm was considered to be the optimal gap, where a good-shaped removal spot and the maximum etching rate can be obtained (The processing gap of maximum etching rate was also considered to achieve the most stable processing due to the $\Delta_{\text{Etching rate}}/\Delta_{\text{processing gap}}$ was small).

4.2.3 Causes of deterioration of surface roughness after AP-PCVM

As described in section 1.2.2, RS-SiC was manufactured by reaction-sintered at 1693 K in vacuum using green body (mixture of SiC power and carbon power) and silicon melt. Hence, SiC particles and unreacted Si are present in RS-SiC. Figure 4.12 shows a scanning electron microscope (SEM) image of the surface of RS-SiC used in this work, which was prepared by diamond lapping. And energy dispersive spectroscopy (EDS) spectra of point A, B, and C was also measured. It can be observed that the grain-shaped regions, which occupied most of the field of observation area, was SiC grains (point A and B). And the regions between the SiC grains are filled with Si (point C). Besides, many scratches were formed on the surface during the diamond lapping process.

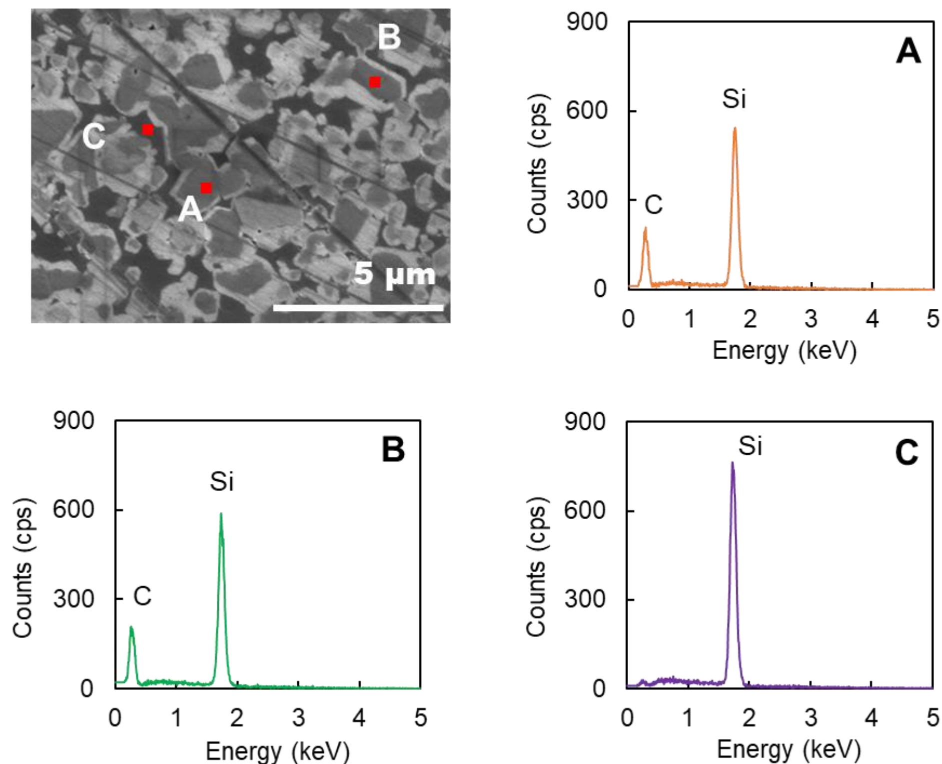

Figure 4.12 SEM image of the surface prepared by diamond lapping and EDS spectra of point A, B and C.

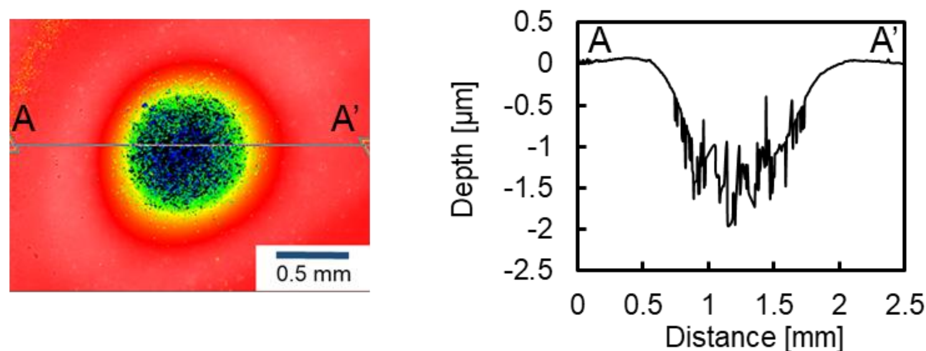

Figure 4.13 SWLI image of a removal spot formed by AP-PCVM as well as its cross section.

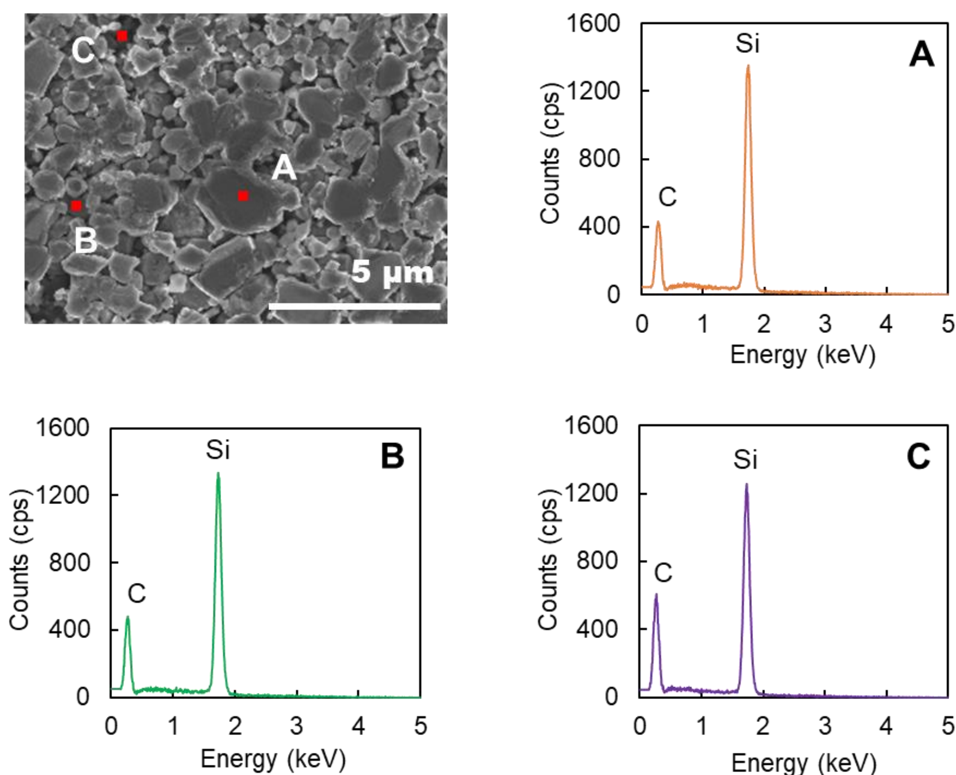

Figure 4.14 SEM image of the center of the removal spot processed by AP-PCVM (microwave power: 59 W, carrier Ar: 500 sccm, process Ar: 1000 sccm, CF_4: 50 sccm, O_2: 50 sccm, processing gap: 6 mm), and EDS spectra of point A, B, and C.

Preliminary investigation experiment of etching characteristics was conducted on RS-SiC. The size of the RS-SiC substrate was 50 mm × 50 mm × 3 mm, and all the AP-PCVM experiments were conducted at room temperature without substrate heating. The temperature of the surface irradiated by plasma, which was measured by infrared thermography, was less than 50°C. The carrier gas was

Ar (500 sccm) and the process gases were Ar (1000 sccm), CF_4 (50 sccm) and O_2 (50 sccm). The working gap between the tip of the nozzle and the sample surface, the microwave power and the machining time were 6.0 mm, 59 W, and 60 s, respectively. Figure 4.13 shows a SWLI image of a removal spot formed by AP-PCVM as well as its cross section. It was found that near the center of the removal spot, the roughness of the surface became large. To clarify the reason for the deterioration of the surface roughness, SEM image of the center of the removal spot was measured and shown in Figure 4.14. By comparing with the SEM image of RS-SiC (Fig. 4.12) before AP-PCVM, it can be clearly found that the surface morphology of RS-SiC has changed significantly. EDS spectra of point A, B, and C was also measured and shown in Fig. 4.14. In contrast to the image shown in Fig. 4.12, in the area processed by AP-PCVM, as shown in the EDS spectra, no matter the grain-shaped regions (point A) or the regions between the grains (point B and C), only SiC was detected. It means that, the Si regions that originally existed between SiC grains disappeared. It is assumed that the etching rate of Si was higher than that of SiC, the regions between SiC grains have been etched away, but the SiC grain remained. In other words, the difference between the etching rates of Si and SiC led to the large surface roughness. Thus, to obtain RS-SiC with a smoothly etched surface, it is essential to make the etching rate of SiC equal to that of Si.

4.2.4 Optimization of processing conditions for Gas composition

As discussed in section 4.2.3, to obtain RS-SiC with a smoothly etched surface, it is essential to make the etching rate of SiC equal to that of Si. However, due to the different chemical properties of the different components (SiC component and Si component) in RS-SiC, it is difficult to make the etching rate of them identically. A study on the relationship between the oxygen fraction in a process gas and the etching rate of Si has been reported by Mogab *et al.* for a low-pressure CF_4-O_2 plasma etching process [4]. Their results showed that the addition of O_2 to a CF_4 plasma markedly increases the optical emission intensity from atomic fluorine, but the etching rate is not strictly proportional to the density of F radicals because of the competition between F radicals and O radicals for active Si surface sites. If the etching rate - Oxygen fraction curves of Si and SiC have a cross point, then, it is considered that the etching rate of Si equal to that of SiC under the oxygen fraction condition at the cross point.

4.2.4.1 Correlation between gas composition and etching rate of Si (100) & SiC (0001)

To investigate the AP-PCVM etching characteristics and find the process gas composition for which the etching rate of Si is equal to that of SiC, spot processing experiments were conducted on 4H-SiC (0001) and Si (100) substrates using the optimal gap obtained in section 4.2.2 in different

Table 4.1 Experimental conditions of AP-PCVM in different oxygen fractions.

Parameters	Conditions
Experimental setup	Figure 4.1
Substrates	4H-SiC (0001)
	Si (100)
Carrier gas	Ar (500 sccm)
Process gas	Ar (1000 sccm)
	CF_4 (100 → 5 sccm)
	O_2 (0 → 95 sccm)
Applied microwave power	59 W
Processing gap	6 mm
Processing time	60 s

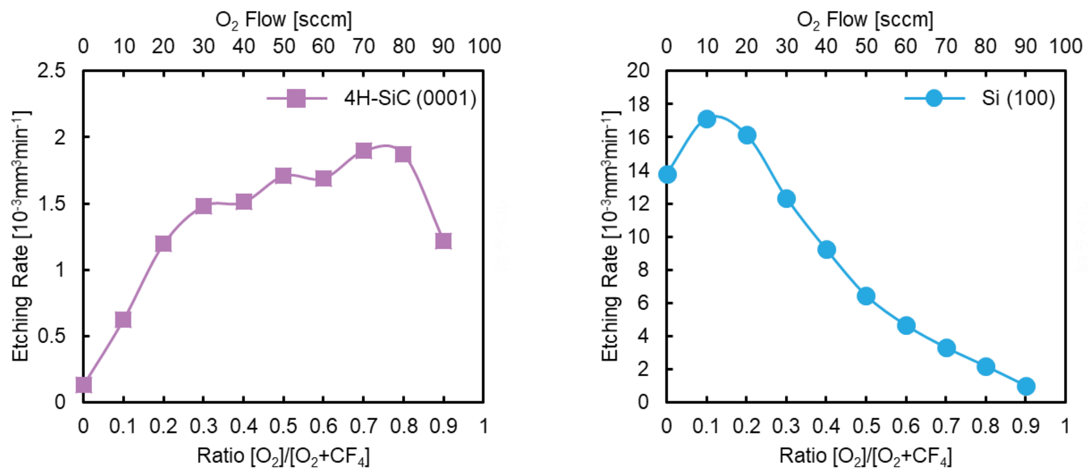

Figure 4.15 Etching rates of 4H-SiC (0001) and Si (100) for different oxygen fractions.

[O_2/(O_2 + CF_4)] ratios. The detailed experimental conditions are shown in Table 4.1. The flow of O_2 increased as the flow of CF_4 decreased, but their total flow was controlled at 100 sccm. The obtained etching rate–Oxygen fraction curves of 4H-SiC (0001) and Si (100) are shown in Fig. 4.15. The obtained experimental results were similar to those described in the papers of P. H. Yih *et al.* [5] and C. J. Mogab *et al* [4]. The etching rate of Si (100) generally increased at low oxygen fractions and the maximum etching rate was obtained at an O_2 concentration of about 10%. Then the etching rate decreased as the oxygen fraction further increased. The 4H-SiC (0001) etching rate exhibited a much less marked peak than Si (100) at an O_2 concentration of 70%. Since the bond dissociation

energy of Si-Si (310 kJ/mol) is lower than that of Si-C (447 kJ/mol) [6], it is considered that the lower bond dissociation energy of Si-Si led to a higher etching rate of Si (100) than that of 4H-SiC (0001) under the same conditions.

4.2.4.2 Mechanism for the change of etching rate under different gas composition

Although the absolute value of the etching rate of Si (100) and 4H-SiC (0001) and the oxygen fraction required to reach the maximum etching rate was different, their overall change were the same. As the oxygen fraction in the process gas increases, the etching rate initially increased and then decreased. Before exploring the mechanism for the change of etching rate under different gas composition, the chemical reactions that occurred during the AP-PCVM process should be clarified. Since AP-PCVM was carried out under an open atmosphere, the oxygen in the air was also excited and participated in the etching process. In the case of using the process gas (CF_4) without adding oxygen, the possible chemical reactions that occur in the AP-PCVM of 4H-SiC (0001) and Si (100) are as follows:

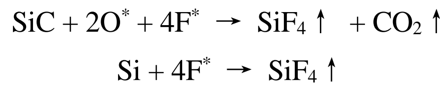

$$SiC + 2O^* + 4F^* \rightarrow SiF_4\uparrow + CO_2\uparrow$$
$$Si + 4F^* \rightarrow SiF_4\uparrow$$

As written in the chemical equation, F radicals (F^*) are considered to contribute to the etching process in AP-PCVM. It means that under the premise that the concentration of F^* was not saturated, as the number of F^* increases, the etching rate will also increase.

As reported in the paper of C. J. Mogab *et al.* [4], in CF_4 plasma, in the absence of oxygen, electrons in the proper energy range decompose CF_4 via the reaction below

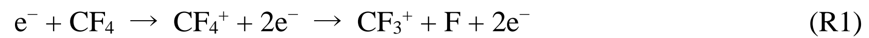

$$e^- + CF_4 \rightarrow CF_4^+ + 2e^- \rightarrow CF_3^+ + F + 2e^- \qquad (R1)$$

$$e^- + CF_4 \rightarrow CF_3 + F + e^- \qquad (R2)$$

$$e^- + CF_4 \rightarrow CF_3 + F^- \qquad (R3)$$

The first reaction (R1) has a higher threshold energy and proceeds more slowly than one of the latter two reactions (R2 and R3), but, nevertheless, generates sufficient positive ions and electrons to sustain the discharge. Reaction (R2) is energetically less favorable than (R3) and may be slow by comparison. The concentration of negative fluorine ions is also limited by the recombination,

$$CF_3 + F^- \rightarrow CF_4 + e^- \qquad (R4)$$

F atoms are also lost by heterogeneous recombination,

$$CF_3 + F \xrightarrow{Wall} CF_4 \qquad (R5)$$

When a small amount of oxygen was added into process gas, reaction

$$CF_3 + O_2 \rightarrow COF_2 + OF \quad \text{(R6)}$$

was considered to occurred. The combination of CF_3 with oxygen competed with reactions (R4) and (R5) and prevent the recombination of fluorine ions. In addition, the OF radical is highly reactive and can be converted to F atoms by several paths as follow

$$CF_3 + OF \rightarrow COF_2 + 2F \quad \text{(R7)}$$

$$OF + OF \rightarrow O_2 + 2F \quad \text{(R8)}$$

According to the reaction above, the addition of a small amount of oxygen in the CF_4 plasma can effectively promote the decomposition of CF_4 and the formation of F, which resulted in a marked increase in the etching rate of 4H-SiC (0001) and Si (100).

However, after the etching rate reaching the maximum value, it began to decrease as the oxygen fraction in process gas further increased. To verify the chemical reactions occurred in AP-PCVM at high oxygen fraction, X-ray photoelectron spectroscopy (XPS) measurement of the Si surfaces etched by AP-PCVM with different $[O_2/(O_2+CF_4)]$ ratios were conducted with a take-off angle of 30°. Figure 4.16 shows the Si2p spectra of Si (100) etched by AP-PCVM at oxygen fractions of 0%, 50%, and 90%. Since oxygen is present in the atmosphere, although no oxygen was initially added to the process gases, a Si-O peak (103.5 eV) [7] was observed on the surface. The Si-O peak became stronger as the oxygen fraction increased. The thickness (d) of the oxide layer at different oxygen

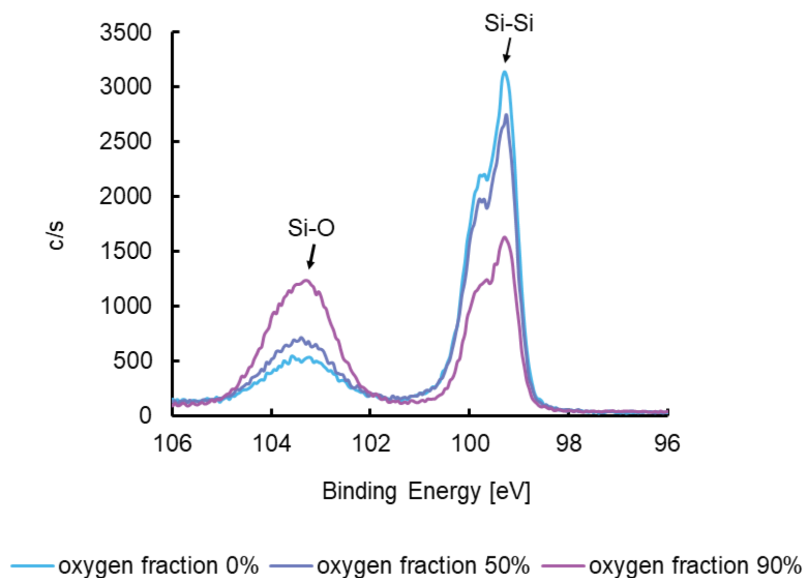

Figure 4.16 Si2p-XPS spectra of Si (100) etched by AP-PCVM for oxygen fractions of 0%, 50% and 90%.

fractions on Si (100) was calculated from the ratio of the Si-O peak and Si-Si peak intensities using the oxide thickness determination equation [8]

$$d = \lambda_{ox} \cdot sin\theta \cdot ln\left[\left(\frac{N_m}{N_{ox}} \cdot \frac{\lambda_m}{\lambda_{ox}}\right) \cdot \frac{I_{ox}}{I_m} + 1\right] \quad (4\text{-}13)$$

λ_m, λ_{ox}: escape depth of photoelectrons in base material and oxide layer.
N_m, N_{ox}: volume densities of atoms in base material and oxide layer.
θ: take-off angle of photoelectrons.
I_m, I_{ox}: intensities of photoelectron peaks of base material and oxide layer.

In the case of Si (100), λ_{Si} and N_{Si} were 3.34 nm [9] and 4.80 $\times 10^{22}/cm^3$, respectively. And in the case of SiO_2, λ_{SiO_2} [10] and N_{SiO_2} were 3.95 nm and 2.21 $\times 10^{22}/cm^3$, respectively. The calculated thickness oxide layer at different oxygen fractions is shown in Fig. 4.17. With increasing oxygen fraction in the process gases, the thickness of the residual oxide layer on Si (100) also increased. Similar plasma simulation results have also been reported by R. Knizikevicius [11]. As for 4H-SiC (0001), no Si-O peak was observed in the case of 4H-SiC (0001) at low oxygen fractions. Only for an oxygen fraction of 90% was an oxide layer observed, which had a thickness of 1.05 nm oxygen (λ_{SiC} [12] and N_{SiC} were 2.78 nm and 4.83 $\times 10^{22}/cm^3$, respectively). This means that as the fraction increased, the competition between the adsorption of oxygen and the etching by active species inhibited the etching process and led to a decrease in the etching rate at a high oxygen fraction. Despite O radicals being dominant owing to the high oxygen fraction, since the Gibbs free

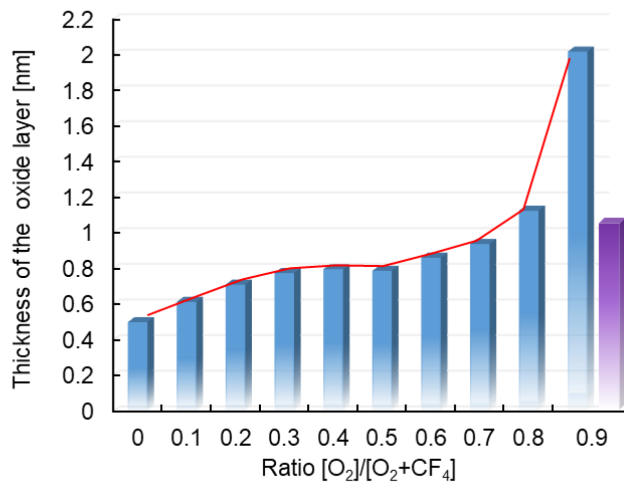

Figure 4.17 Thickness of oxide layer on Si (100) and 4H-SiC (0001) surface for different oxygen fractions.

energy of SiF_4 (−1573 kJ/mol) is lower than that of SiO_2 (−853 kJ/mol), although the middle of the reaction process produced SiO_2, the final reaction product was SiF_4 rather than SiO_2 [13]. Thus, the actual AP-PCVM process at high oxygen fractions is considered not simply an etching process but also involves oxidation process.

Oxidation process:

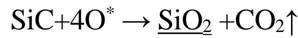

$SiC+4O^* \rightarrow \underline{SiO_2} + CO_2\uparrow$

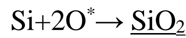

$Si+2O^* \rightarrow \underline{SiO_2}$

Etching process:

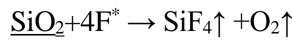

$\underline{SiO_2}+4F^* \rightarrow SiF_4\uparrow + O_2\uparrow$

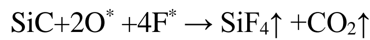

$SiC+2O^* + 4F^* \rightarrow SiF_4\uparrow + CO_2\uparrow$

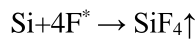

$Si+4F^* \rightarrow SiF_4\uparrow$

The etching rate–Oxygen fraction curves of 4H-SiC (0001) and Si (100) are integrated and shown in Fig. 4.18. The cross point of two curves, in which the etching rate of 4H-SiC (0001) was equal to that of Si (100), was obtained at oxygen fraction of around 85%. As shown in Fig. 4.17, after AP-PCVM, a residual oxide layer was confirmed on both 4H-SiC (0001) and Si (100) at oxygen fraction of 90%. Although the oxidation process and etching process proceed simultaneously during the actual AP-PCVM process, the oxidation process was considered to dominate the AP-PCVM process at oxygen fraction 90%. And in this condition, the AP-PCVM process can be simply considered

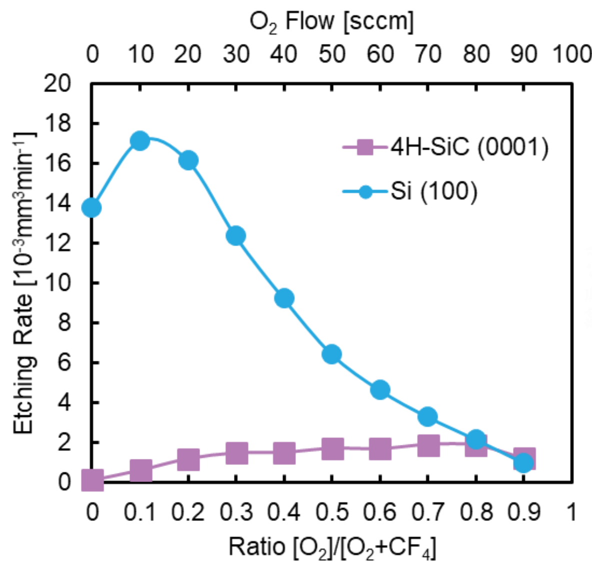

Figure 4.18 Etching rates of 4H-SiC (0001) and Si (100) for different oxygen fractions.

as a process in which SiC/Si was firstly oxidized and then etched away in the form of oxide layer (SiO_2). This can explain the reason why the etching rate of 4H-SiC (0001) and Si (100) was equivalent, and an oxide layer was remained.

4.2.4.3 Improvement of surface roughness of RS-SiC by optimizing gas composition

It has been found that the gas composition for which the etching rate of Si (100) coincided with that of 4H-SiC (0001) had an oxygen fraction of between 80% and 90%. As described in section 4.2.2, the surface roughness of RS-SiC became worse after AP-PCVM due to the difference between the etching rates of Si component and SiC component. Therefore, it is considered that a smooth surface can be obtained by AP-PCVM under the conditions around the cross point of the two curves shown in Fig. 4.18. To find the optimum gas composition for processing RS-SiC, spot processing experiments were conducted on RS-SiC with different oxygen fractions (80%, 85%, 90%). The carrier gas was Ar (500 sccm) and the process gases were Ar (1000 sccm), CF_4 (20, 15, 10 sccm) and O_2 (80, 85, 90 sccm). The working gap was 6.0 mm and the etching time was 60 s. Figure 4.19 shows SWLI images and cross sections of the removal spots. The surface roughness of the removal spot has been greatly improved with an oxygen fraction of 90% but the removal spot was shallow. It is possible that the surface roughness deteriorates as the depth of the removal spot increases. To investigate this hypothesis, a 120s-removal spot was processed on RS-SiC with an oxygen fraction of 90%. Figure 4.20(a) shows the cross sections of removal spots etched with an oxygen fraction of 90% for 60 and 120 s, and Fig. 4.20(b) shows the cross section of a removal spot etched with an oxygen fraction of 50% for 60 s. The figures showed that the surface roughness of the removal

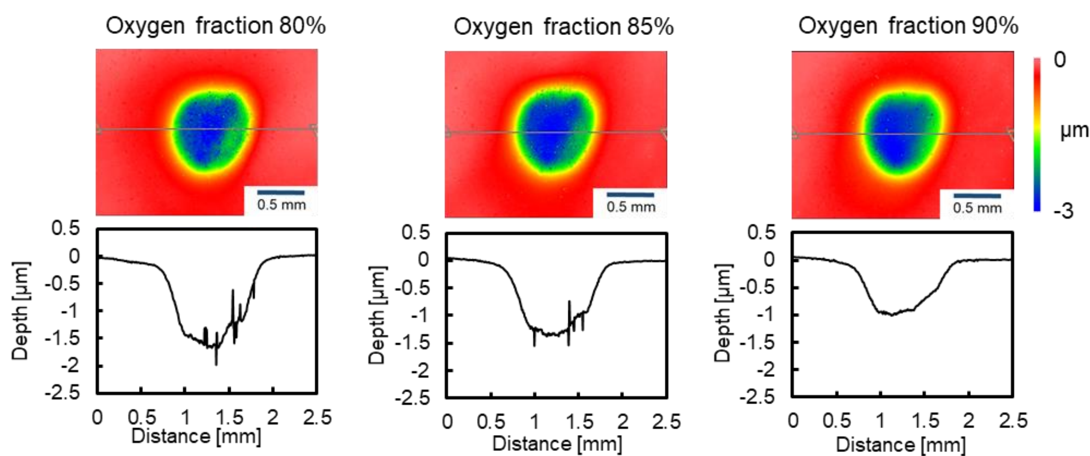

Figure 4.19 SWLI images and cross sections of removal spots at oxygen fractions of 80%, 85% and 90%.

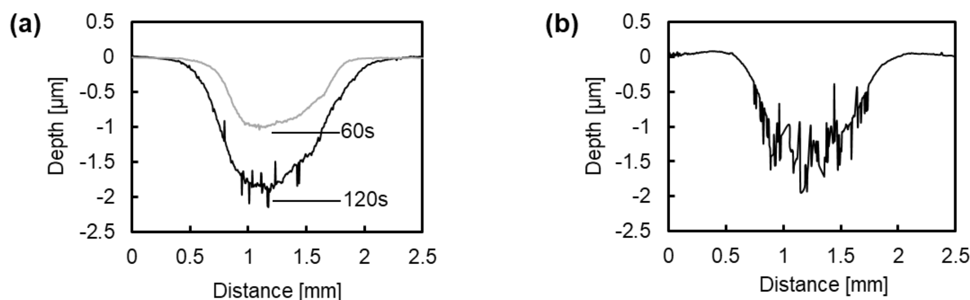

Figure 4.20 Cross section of removal spots etched with an oxygen fraction of (a) 90% for 60 and 120 s, (b) 50% for 60 s.

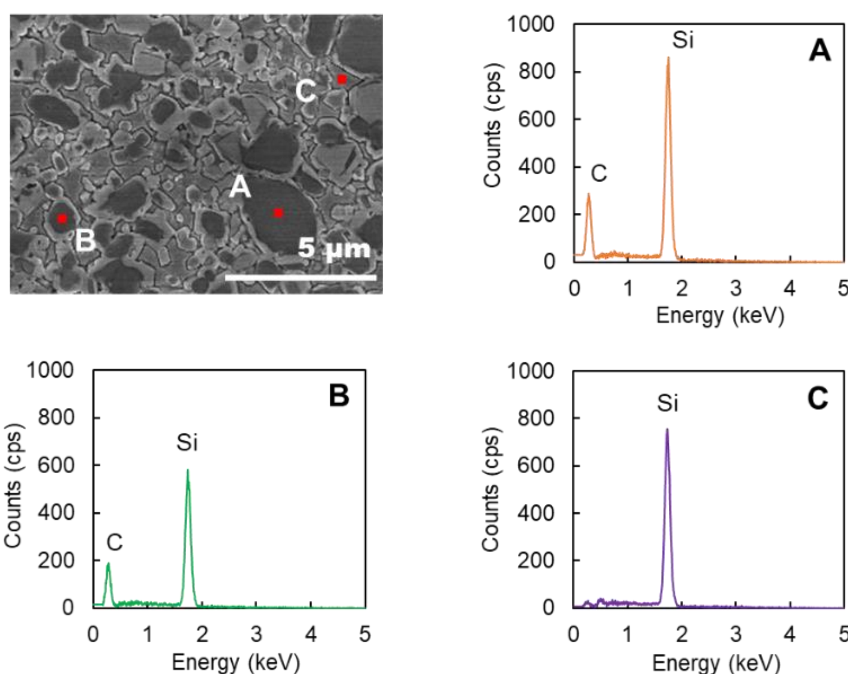

Figure 4.21 SEM image of the RS-SiC processed by AP-PCVM with an oxygen fraction of 90% (microwave power: 59 W, carrier Ar: 500 sccm, process Ar: 1000 sccm, CF_4: 10 sccm, O_2: 90 sccm, processing gap: 6 mm), and EDS spectra of point A, B, and C.

spot etched with an O_2 fraction of 90% was lower than that of the surface etched with an O_2 fraction of 50% even for the same removal depth. Figure 4.21 shows the SEM image of the RS-SiC surface etched with an O_2 fraction of 90% and EDS spectra of point A, B, and C. Since Si component and SiC component were removed in the same etching rate, the RS-SiC surface after AP-PCVM was the same as the initial surface, where the regions between the SiC grains (point A and B) are filled with Si (point C).

4.2.4.4 Raster scanning results for AP-PCVM on RS-SiC using optimized gas composition

In the previous section, it was confirmed that a removal spot with a smooth surface can be obtained at an oxygen fraction of 90%. From the etching rate curve, it was assumed that the etching

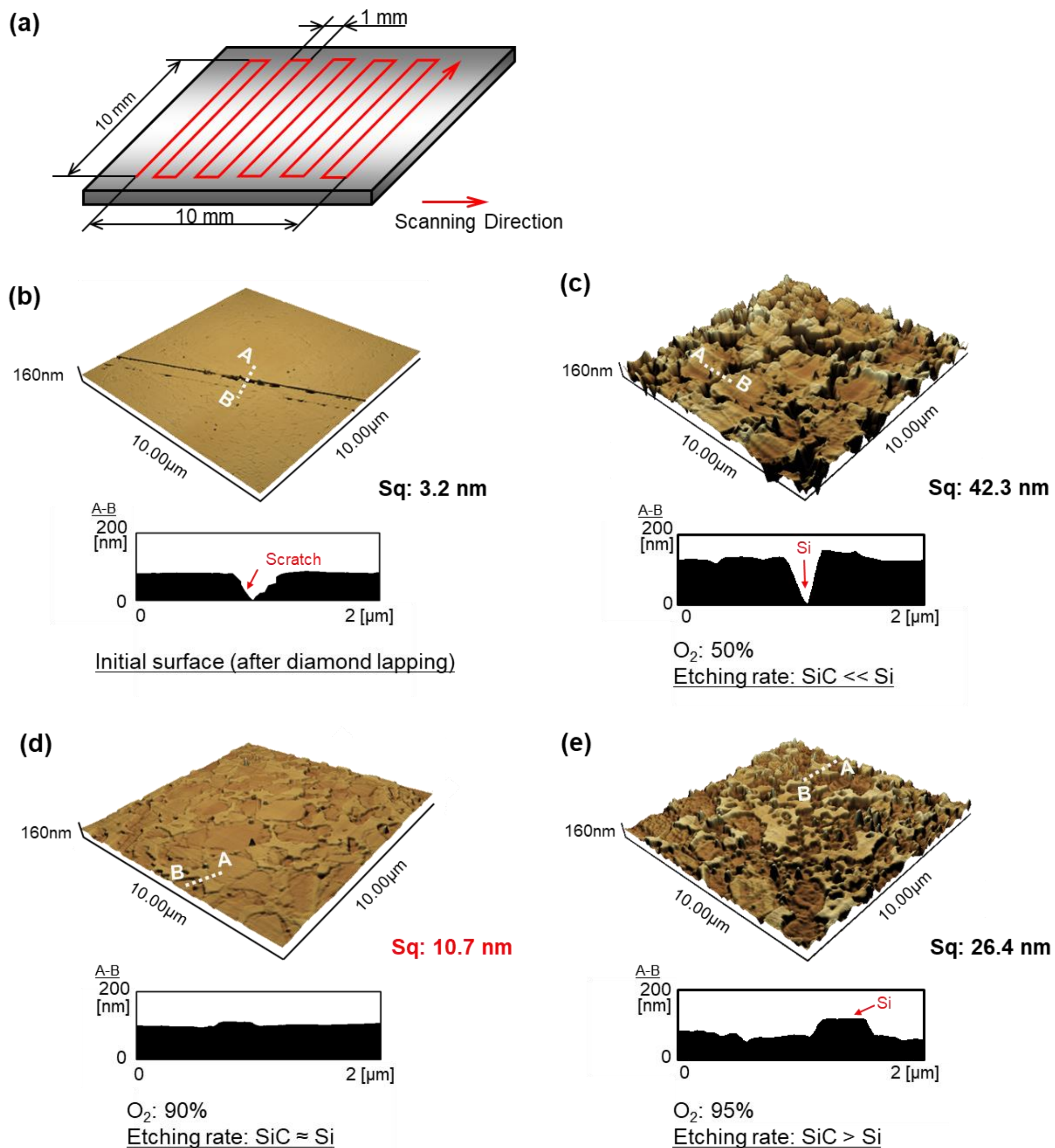

Figure 4.22 Raster scanning results for AP-PCVM. (a) Scanning path, (b) AFM image of initial surface processed by diamond lapping before AP-PCVM, (c) AFM image of surface etched by AP-PCVM with oxygen fraction of 50%, (d) AFM image of surface etched by AP-PCVM with oxygen fraction of 90%, (e) AFM image of surface etched by AP-PCVM with oxygen fraction of 95%.

rate of Si (100) is greater than that of 4H-SiC (0001) when the oxygen fraction is less than 90% and that the etching rate of Si (100) is less than that of 4H-SiC (0001) when the oxygen fraction is more than 90%. In the actual application of AP-PCVM, since the volume of the removal spot increases with the processing time, the local removal volume at a certain position can be controlled via the dwelling time of the plasma jet during scanning. A surface etching experiment was conducted to evaluate the roughness of surfaces etched by AP-PCVM with oxygen fractions of 50%, 90%, and 95%. The carrier gas was Ar (500 sccm) and the process gases were Ar (1000 sccm), CF_4 (50, 10, 5 sccm) and O_2 (50, 90, 95 sccm). The working gap was 6.0 mm. The scanning path is shown in Fig. 4.22(a). The size of the etched area in the AP-PCVM was 10 mm × 10 mm, and etching was performed in the raster scanning mode with a scan speed of 10 mm/min and a feed pitch of 1 mm. To ensure the same etching depth, the etching process was conducted twice with oxygen fractions of 90% and 95%. Figure 4.22(b) shows the initial surface before AP-PCVM, which was prepared by diamond lapping, whose roughness was measured by atomic force microscopy (AFM). Although the surface roughness was excellent, an SSD layer and scratches were formed as shown in Fig. 4.12. Figure 4.22(c) shows an AFM image of the surface after etching with an oxygen fraction of 50%. Since the etching rate of Si was greater than that of SiC at this oxygen fraction, the regions between SiC were concave and the surface roughness deteriorated to 42.3 nm *S*q. Figure 4.22(d) shows an AFM image of the surface after etching with an oxygen fraction of 90%. Since the etching rates of Si and SiC coincided at this oxygen fraction, a smooth surface was obtained. As AP-PCVM is an isotropic etching process, the surface became slightly rougher than the diamond lapped surface. Figure 4.22(e) shows an AFM image of the surface after etching with an oxygen fraction of 95%. Since the etching rate of Si was less than that of SiC, the regions between the SiC grains protruded. For this reason, the surface roughness deteriorated to 26.4 nm *S*q. To demonstrate the reproducibility of the experiments, the experiment described above was conducted four times with three different

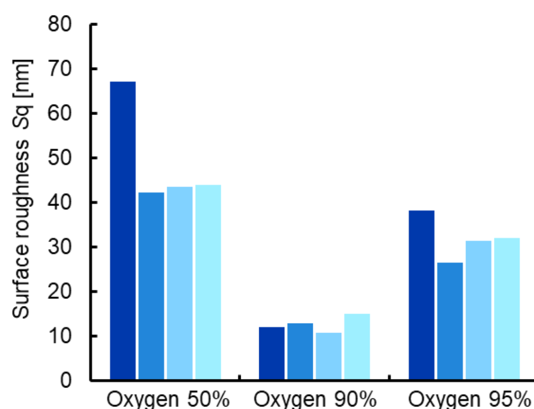

Figure 4.23 Variation in surface roughness of RS-SiC etched by raster scanning AP-PCVM with oxygen fractions of 50%, 90% and 95%.

oxygen fractions. The surface roughness was measured at four random locations under each condition and the variation in the surface roughness of RS-SiC etched by raster scanning AP-PCVM with oxygen fractions of 50%, 90% and 95% is shown in Fig. 4.23. It was shown that the surface roughness was greatly decreased with an oxygen fraction of 90%.

The models proposed for the AP-PCVM process on an RS-SiC surface at different oxygen

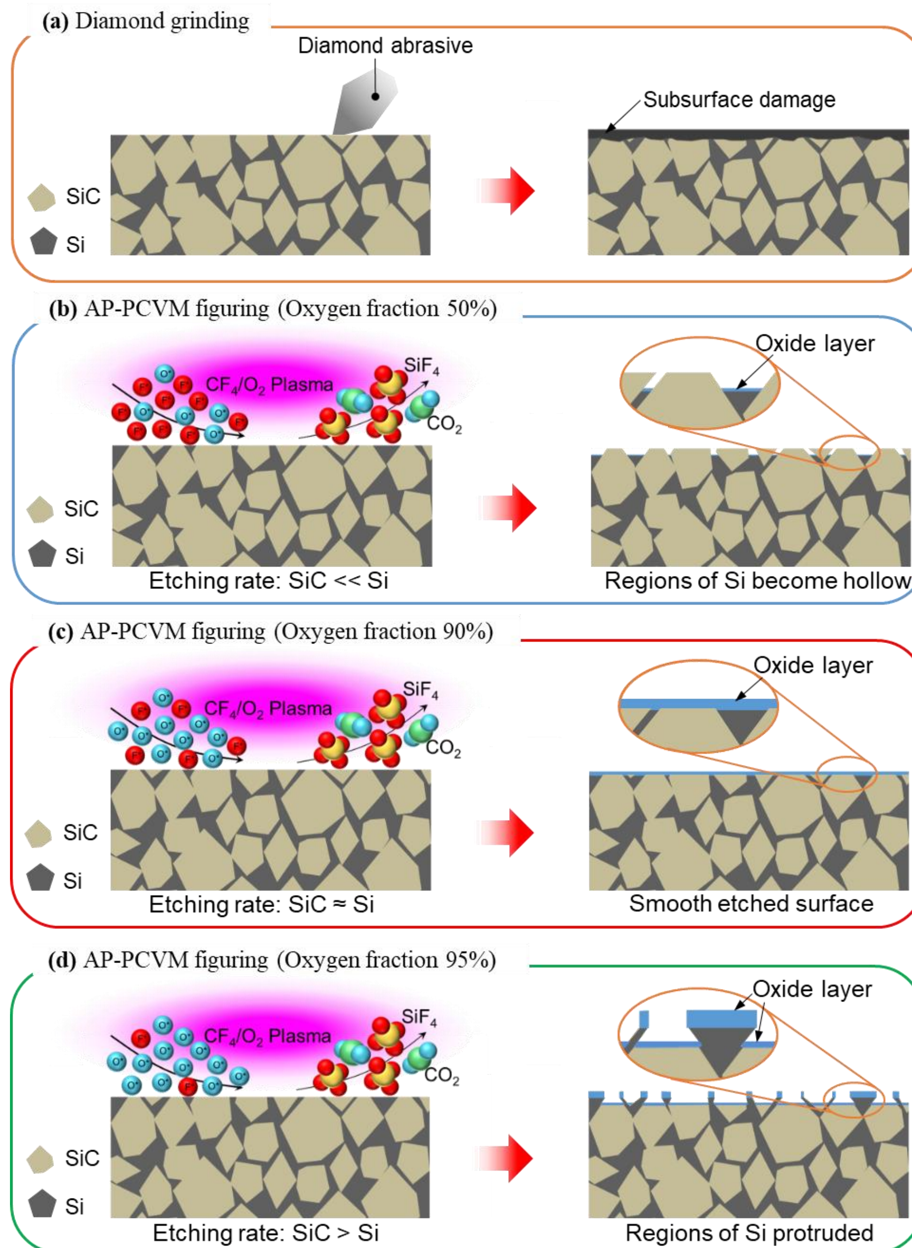

Figure 4.24 Models showing figuring process for SiC/Si-MMC. (a) Figuring by diamond grinding, (b) Figuring by AP-PCVM (etching rate: SiC << Si), (c) Figuring by AP-PCVM (Etching rate: SiC ≈ Si), (d) Figuring by AP-PCVM (etching rate: SiC > Si).

fractions are shown in Fig 4.24. As shown in Fig. 4.24(a), turning, and grinding with a diamond tool are used to realize figuring with high precision and high efficiency. However, scratches and an SSD layer are inevitably formed. Since AP-PCVM is a pure chemical noncontact process, scratches and an SSD are not formed. As shown in Fig. 4.24(b), when the etching rate of Si was greater than that of SiC (oxygen fraction of 50%), the volume of removed Si was larger than that of SiC, causing the regions of Si to become hollow. As shown in Fig. 4.24(d), when the etching rate of Si was less than that of SiC (oxygen fraction of 95%), the volume of removed Si was smaller than that of SiC; thus, the regions of Si protruded. Neither of the two conditions produced a smoothly etched surface. As shown in Fig. 4.24(c), only when the etching rate of Si coincided with that of SiC (oxygen fraction of 90%) were the Si and SiC etched at the same rate and a smoothly etched surface was obtained.

4.2.5 Aspherical shape figuring of RS-SiC by AP-PCVM

As discussed in the previous sections, the etching rates of Si and SiC components coincided with an oxygen fraction of 90%, smooth etched surface of RS-SiC can be obtained by AP-PCVM. In this section, a figuring experiment was performed on RS-SiC to form an aspherical shape using the optimum gas composition. The processing theory of figuring by AP-PCVM has been introduced in Chapter 2 (section 2.4.3), dwelling time distribution of plasma in figuring process can be obtained through the deconvolution simulation using the target removal volume data and removal spot data. In this time, the target removal volume should be the superposition of the initial surface shape of RS-SiC before AP-PCVM and the design shape. The target shape was an aspherical shape designed by the equation as follow:

$$1000\boldsymbol{Z} = \frac{0.4\boldsymbol{r}^2}{1+\sqrt{1-(1-0.99)0.16\boldsymbol{r}^2}} + 5.3\times10^{-5}\boldsymbol{r}^4 - 10^{-8}\boldsymbol{r}^6 - 10^{-10}\boldsymbol{r}^8 - 4\times10^{-12}\boldsymbol{r}^{10}$$

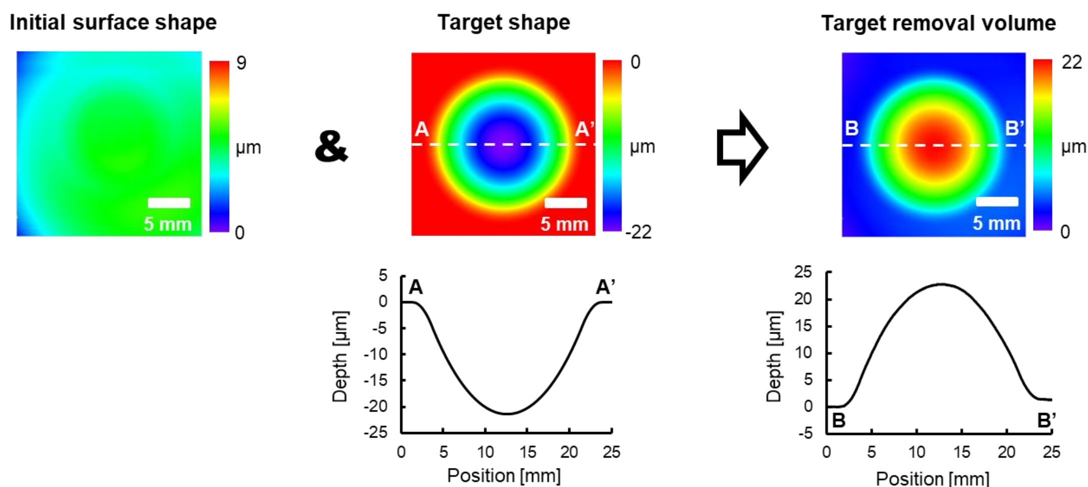

Figure 4.25 Target removal volume used in deconvolution simulation.

The optic axis is presumed to lie in the *z* direction, and the Z-component of the displacement of the surface from the vertex, at distance *r* from the axis. Diameter of the aspherical shape was 20 mm and the maximum depth was 21.3387 μm. The initial surface shape of RS-SiC was measured by point autofocus probe 3D measuring instrument (MITAKA NH-3S), and the target removal volume was calculated as shown in Fig. 4.25. Removal spot data used in deconvolution simulation was processed using the optimum processing conditions obtained in the previous sections (the carrier gas was Ar (500 sccm) and the process gases were Ar (1000 sccm), CF_4 (10 sccm) and O_2 (90 sccm). And working gap was 6.0 mm). Using the scanning velocity distribution result calculated by

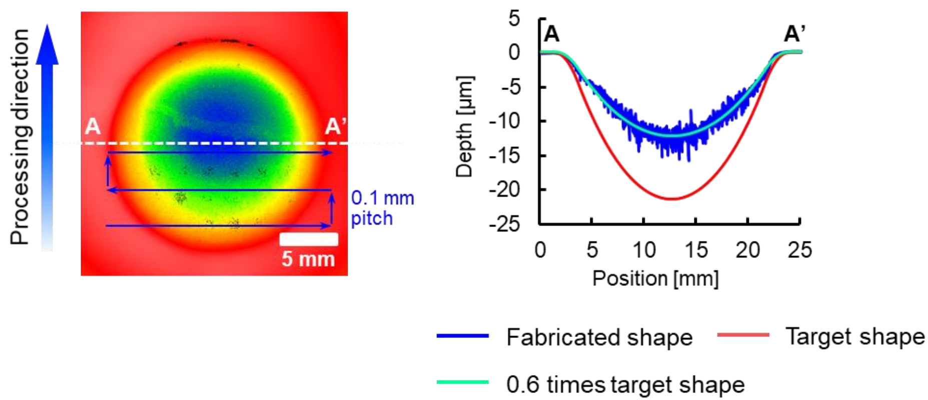

Figure 4.26 SWLI images and cross sections of fabricated shape.

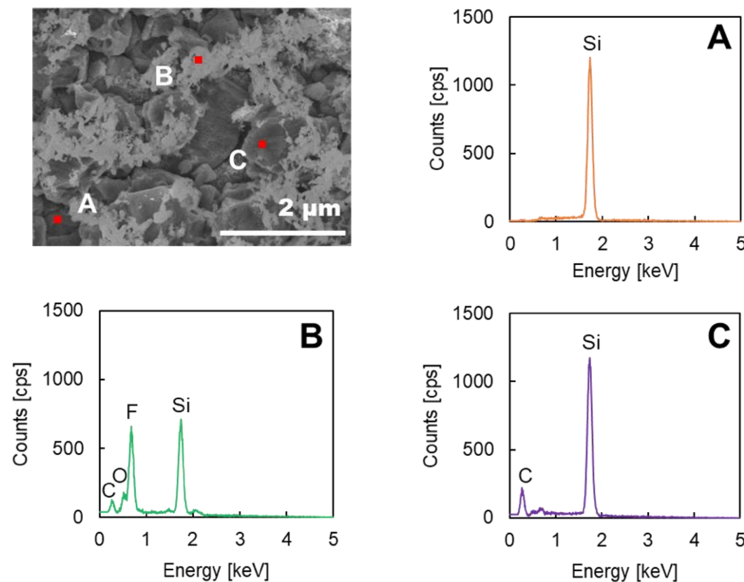

Figure 4.27 SEM image of the RS-SiC surface processed by NC-AP-PCVM and EDS spectra of point A, B, and C.

deconvolution simulation, a numerically controlled (NC) AP-PCVM was performed for about 8 hours, and the SWLI image and cross section of fabricated shape was shown in Fig. 4.26. The diameter of fabricated shape was the same with target shape (20 mm), but the depth was shallower than the target. The fabricated shape after the NC processing and the target shape have a proportional relation of about 0.6 times rather than being partially shallow. Figure 4.27 shows the SEM image of the RS-SiC surface after NC-AP-PCVM and EDS spectra of point A, B, and C. Since the etching rate of Si component coincides with that of SiC using the optimum gas composition, both of Si (point A) and SiC (point C) were observed on the surface after NC-AP-PCVM. However, in the position of suspected deposits (point B), Si, F, O, and C, four elements were detected. It is considered that F-based reaction products during NC-PCVM redeposited on the surface. Since reaction products (F-based) did not react with CF_4 plasma, the following etching process was suppressed and led to a shallower removal depth than target. Moreover, the redeposit of reaction products also led to the surface roughness deteriorated.

4.2.6 Optimization of processing conditions: Substrate temperature

The result in section 4.2.5 shows that the redeposition of reaction products on the substrate surface led to the shallow removal depth and deterioration of surface roughness. Therefore, preventing the redeposition of reaction products is essential during NC-AP-PCVM to improve the processing accuracy.

4.2.6.1 Effect of substrate temperature on redeposition of reaction products

So far, all the AP-PCVM experiments were conducted at room temperature without substrate heating. Consider the kinetic approach for the case of a uniform solid surface exposed to an adsorbing gas. According to the kinetic theory of gases, the flux I of the gas molecules impinging on the surface from the gas phase is given by

$$I = \frac{p}{\sqrt{2\pi m k_B T}}$$

where p is the partial pressure of the adsorbing gas, m is the mass of the gas molecule, k_B is Boltzmann's constant, and T is the temperature [14]. However, not all the impinging molecules become adsorbed at the surface, i.e., contribute to the adsorption rate. The ratio of the adsorption rate to the impingement rate is defined as the sticking coefficient s. Thus, the adsorption rate r_a is

$$r_a = sI = \frac{sp}{\sqrt{2\pi m k_{\mathrm{B}} T}}$$

It means that during the AP-PCVM process, the adsorption (redeposition) rate of the reaction products is related to the substrate temperature. Properly increasing the substrate temperature is considered to effectively reduce the redeposition of reaction products. To verify the relationship between the substrate temperature and the redeposition of reaction products, a surface processing experiment was carried out with the same raster scan speed. The detailed experimental conditions are shown in Table 4.2. Figure 4.28 shows the SEM images and F1s-XPS spectra of the initial

Table 4.2 Experimental conditions of AP-PCVM in different substrate temperature.

Parameters	Conditions
Experimental setup	Figure 4.1
Substrate	RS-SiC
Substrate temperature	25ºC / 400ºC
Carrier gas	Ar (500 sccm)
Process gas	Ar (1000 sccm)
	CF_4 (10 sccm)
	O_2 (90 sccm)
Applied microwave power	59 W
Processing gap	6 mm
Scan pitch	0.1 mm

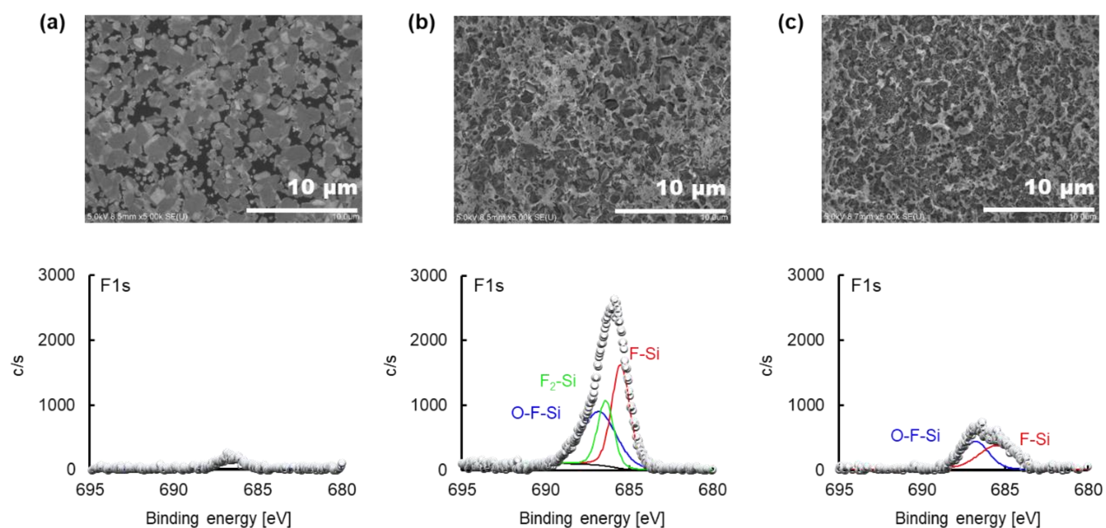

Figure 4.28 SEM image and F1s-XPS spectra of RS-SiC (a) before AP-PCVM, (b) after AP-PCVM without substrate heating, (c) after AP-PCVM with substrate heating up to 400ºC.

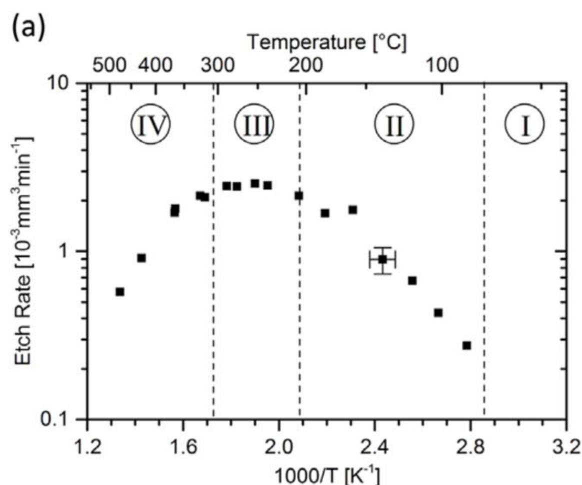

Figure 4.29 The influence of substrate temperature on etching rate [15].

RS-SiC surface and processed RS-SiC surface. Since the RS-SiC substrate before PCVM was cleaned using HF to remove the naturally oxide layer, a small amount of adsorbed F was detected. No obvious attachment was visible on the SEM image as shown in Fig. 4.28(a). After the normal PCVM at room temperature without substrate heating, a large amount of deposition, which was reaction products as shown in Figure 4.27 were observed. F1s-XPS spectra also confirmed this result. However, after the PCVM with substrate heating up to 400ºC, the F1s peak contributed to redeposited reaction products became weak, and the amount of deposition was significantly reduced as shown in the SEM image in Fig. 4.28(c). Therefore, substrate heating was a very effective method to prevent redeposition of reaction products during AP-PCVM process.

4.2.6.2 Effect of substrate temperature on etching rate

Although substrate heating can inhibit redeposition of reaction products, too high substrate temperature will also lead to a decrease in the adsorption rate of reactive radicals (F^*), resulting in a decrease in the etching rate. P. Piechulla *et al*. has reported the relationship between the etching rate and substrate temperature in the case of using He-based CCl_4 plasma etching silicon substrate [15]. As shown in Fig. 4.29, they confirmed when the substrate temperature exceeds a certain value, the etching rate decreased. Following the scheme of a typical reactive vapor process one may assume depletion of reactants by enhanced desorption from the surface. Therefore, the substrate temperature that can inhibit the redeposition of reaction products and maintain a high etching rate is considered the optimal substrate temperature for AP-PCVM. In future work, the optimal temperature will be determined to further improve the processing accuracy of NC-AP-PCVM.

4.3 Surface finishing of RS-SiC by PAP

Although the surface roughness of the processed RS-SiC surface was greatly improved by optimizing processing conditions such as processing gap and gas composition used in AP-PCVM, and the low spatial frequency roughness (LSFR) was removed effectively. However, since AP-PCVM is a pure chemical processing method, isotropy of chemical etching causes AP-PCVM doesn't have the ability to remove high spatial frequency roughness (HSFR). To remove the HSFR remained on the surface after AP-PCVM to obtain an atomically smooth surface, PAP is considered to be an effective method with low cost. The optimization of processing conditions in PAP will be carried out in future work.

4.4 Summary

AP-PCVM can quickly remove LSFR without forming SSD, and PAP can remove HSFR and achieve an atomically smooth surface, thus plasma nanomanufacturing process, which combined AP-PCVM, and PAP is considered a very suitable processing method to process RS-SiC. However, as a pure chemical processing method, the application of AP-PCVM to multicomponent materials such as RS-SiC faces many challenges. In this chapter, through the optimization of a variety of processing conditions, AP-PCVM was successfully applied to RS-SiC and obtained a smooth surface. AP-PCVM was firstly applied to process a multicomponent material until now, which further broadened the application area of plasma nanomanufacturing process.

(1) A microwave plasma generator with special structure was used in this work. In order to clarify the mixed state of the carrier gas and the process gas before and after ejected from the plasma generator, CFD fluid simulation was carried out. The CFD fluid simulation results well explained the reason why the etching rate and the shape of the removal spot changed with the variation of the processing gap in AP-PCVM.

(2) Since the process gas was introduced from the other gas inlets and mixed with the carrier gas, enough time and distance were needed to make them mixed well. Due to insufficient mixing, a circular removal spot was obtained because the distribution of CF_4 was circular at a small processing gap. In contrast, a removal spot with Gaussian-shape was obtained at a relatively large processing gap, where the process gas (CF_4) was fully mixed with the carrier gas. In addition, the distribution in the direction of injection can also explain the correlation between the etching rate and the processing gap. Since the Ar plasma (ignited at the first time using carrier Ar gas), which was the energy source, hit the substrate and lost its energy before mixed

and collided with the ground state CF_4 to generate F radicals, the etching rate was low at small processing gap. With the increase of the processing gap, carrier Ar and CF_4 were fully mixed, and the energy of Ar plasma was transferred to CF_4 to generate F radicals, the etching rate also increased. The processing gap 6 mm, where the removal spot with good shape can be obtained and the change rate of etching rate was small, was the optimal processing gap.

(3) According to the comparison of SEM images, SWLI images and EDS spectra of the RS-SiC surface before and after AP-PCVM, the difference in the etching rate of the Si and SiC components was the main reason for the deterioration of surface roughness. This is also the reason why it was difficult to apply AP-PCVM to the processing of multicomponent materials like RS-SiC.

(4) Upon optimizing the oxygen fraction of the process gases, the etching rates of both Si (100) and 4H-SiC (0001) changed. Due to the promoting effect of oxygen on the formation of F radicals in CF_4 plasma, the etching rate reached the maximum at a certain oxygen fraction and decreased due to the competitive relationship between the oxidation and etching process as the oxygen fraction further increased. When the oxygen fraction was 90%, the etching rate of Si (100) coincided with that of 4H-SiC (0001). Through the analysis of the XPS spectra of the processed surface, the mechanism that making the etching rate of the two components in RS-SiC coincide was the result of the competition between the oxidation process and the etching process. At high oxygen fraction, the oxidation reaction dominated the AP-PCVM process. Both two components were firstly oxidized to SiO_2 and then be etched, thus, the Si and SiC components were removed at the same rate.

(5) The results of raster scanning experiments also proved that, when the oxygen fraction in-process gas was lower than 90%, the etching rate of Si was greater than that of SiC and the surface roughness deteriorated due to the regions of Si became hollow. And when the oxygen fraction was higher than 90%, the etching rate of SiC was greater than that of Si, the surface roughness also deteriorated due to the regions of Si became protruded. Only when the oxygen fraction was 90%, SiC and Si was etched at the same rate and a smoothly etched surface was obtained.

(6) Aspherical shape figuring experiment using the optimal processing conditions was also conducted on RS-SiC by AP-PCVM. The diameter of fabricated shape was the same with target shape, but the depth was shallower than the target. The redeposition of reaction products is the cause of this result. Heating of the substrate was effective in preventing the redeposition

of reaction products. However, a too high substrate temperature also caused the adsorption rate of reactive radicals decrease, thereby result in the decrease of etching rate. Therefore, the optimization of the substrate temperature was also necessary.

(7) AP-PCVM can achieve figuring efficiently without forming SSD, but a further polishing is required to obtain an atomically smooth surface. In plasma nanomanufacturing process, PAP plays the role of surface finishing, and the related work will be carried out in the future.

References

1) https://en.wikipedia.org/wiki/Reynolds_number
2) H. A. McGee, Molecular engineering, *McGraw-Hill*, 1991.
3) K. K. Kuo, Principles of combustion, 1986.
4) C. J. Mogab, A. C. Adams, D. L. Flamm, Plasma etching of Si and SiO_2 – The effect of oxygen additions to CF_4 plasma, *Journal of Applied Physics.* **49** (1978) 3796-3803.
5) P. H. Yih, V. Saxena, A. J. Steckl, A review of SiC reactive ion etching in fluorinated plasma, *Physica Status Solidi b*. **202** (1997) 605-642.
6) Y. R. Luo, Bond dissociation energies, In *CRC Handbook of Chemistry and Physics. (89th ed.)* 65-69.
7) D. R. Wheeler, S. V. Pepper, Angle-resolved X-ray photoelectron spectroscopy of epitaxially grown (100) β-SiC to 1300ºC, *Surface and Interface Analysis.* **10** (1987) 153-162.
8) B. R. Strohmeier, An ESCA method for determining the oxide thickness on Aluminum alloys, *Surface and Interface Analysis.* **15** (1990) 51-56.
9) S. Tanuma, C. J. Powell, D. R. Penn, Calculations of electron inelastic mean free paths. IX. Data for 41 elemental solids over the 50 eV to 30 keV range, *Surface and Interface Analysis.* **43** (2011) 689-713.
10) S. Tanuma, C. J. Powell, D. R. Penn, Calculations of electron inelastic mean free paths for 31 materials, *Surface and Interface Analysis.* **11** (1988) 577-589.
11) R. Knizikevicius, Real dimensional simulation of silicon etching in $CF_4 + O_2$ plasma, *Applied Surface Science.* **201** (2002) 96-108.
12) S. Tanuma, C. J. Powell, D. R. Penn, Calculations of electron inelastic mean free paths III. Data for 15 Inorganic Compounds over the 50-2000 eV range, *Surface and Interface Analysis.* **17** (1991) 927-939.
13) JANAF thermochemical tables, *Journal of Physical and Chemical Reference Data. Monograph* **9** (1998).
14) K. Oura, M. Katayama, A. V. Zotov, V. G. Lifshits, A. A. Saranin, Elementary processes at surfaces I. adsorption and desorption, *Surface Science*. (2003).
15) P. Piechulla, J. Bauer, G. Boehm, H. Paetzelt, T. Arnold, Etch mechanism and temperature regimes of

an atmospheric pressure chlorine-based plasma jet process, *Plasma Processes and Polymers*. **13** (2016) 1128-1135.

Chapter 5

Highly efficient and dress-free dry polishing technique with plasma-assisted surface modification and dressing

5.1 Introduction

Since many pits were formed on the surface by shedding-off grains from the sintered material surface, high-quality polishing of sintered materials has always been a challenging in the field of precision machining. As described in Chapter 1, sintered AlN ceramic is an excellent candidate for heat sinks and microelectronics application [1,2)]. In recent years, research on using AlN substrates as the epitaxial growth substrate has also attracted considerable attention, and requires high-quality AlN surfaces. Although CMP processes are now widely used to polish difficult-to-machine materials with high hardness and chemical inertness, such as SiC and GaN [3,4)], the low MRR of CMP makes such processes very time-consuming. Large particles can easily be formed by the agglomeration of the abrasive particles in slurry when it is placed for a long time as shown in Fig. 5.1. The management and disposal of the used slurry in CMP are also considered as very expensive for actual industrial applications. Thus, a dry polishing technique without using slurry is desired. Generally, a fixed abrasive is used in dry polishing processes. No matter which kind of fixed abrasive grinding stone been used, over a certain period after polishing, the abrasives will undergo wear, and the grinding stones will be overloaded and will lose their polishing ability. Therefore, to solve these problems, a dry dress-free polishing technique, which can also be applied to polishing sintered ceramics materials, is desired. As a part of plasma nanomanufacturing process, PAP is a suitable dry polishing technique. In this chapter, vacuum PAP using Ar-based

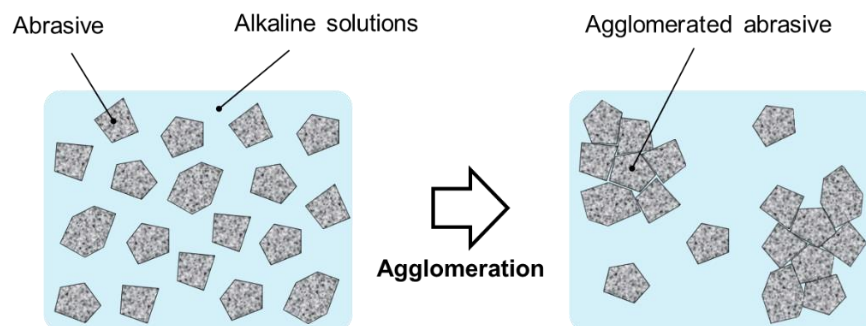

Figure 5.1 Agglomeration of the abrasive particles in slurry used in CMP.

CF_4 plasma, and a vitrified-bonded diamond grinding stone was applied to polish an AlN ceramic wafer. When using CF_4 plasma, it was confirmed that SiO_2, which is the main component material of the binder in the vitrified-bonded diamond grinding stone, was etched by the CF_4 plasma, which is equivalent to the continuous dressing of the grinding stone surface. By irradiating CF_4 plasma, the new diamond abrasives were constantly exposed, and the surface of the AlN grains was modified to AlF_3, so that a high MRR will be maintained. Thus, overall, using a vitrified-bonded grinding stone, the simultaneous plasma-assisted dressing (PAD) in the PAP process enabled a dress-free high integrity polishing process for sintered AlN.

5.2 Vacuum PAP setup used in this work

In our previous research, PAP, which uses fixed abrasives instead of slurry, has been proven to be very effective for obtaining atomically smooth surfaces of difficult-to-machine materials without forming subsurface damages [5,6]. In Ref. [5], Yamamura *et al.* modified the Si face of 4H-SiC into SiO_2 by the irradiation of atmospheric-pressure water-vapor plasma, and they obtained an atomically smooth surface without subsurface damages using a CeO_2 polishing film to remove the modified SiO_2 layer. In Ref. [6], Deng *et al.* confirmed that many pits were generated on a GaN surface after using a conventional CMP process, where the pits originated because of dislocations in the GaN epilayer. It was considered that these pits were generated by the preferential etching of the dislocations using the chemicals in the slurry. In contrast, in the case of PAP, the atmospheric-pressure CF_4 plasma irradiation modified the GaN surface to GaF_3, and an atomically smooth pit-free GaN surface was obtained by removing the GaF_3 layer using a CeO_2 resin-bonded grinding stone. As for the capacitively coupled plasma (CCP) used in PAP, the breakdown conditions at different gas pressures were first studied by Paschen *et al.*, and the result of their study is the well-known Paschen curve [7], which is explained thus: In a discharge system, in which the electrode distance is constant, an increase in pressure leads to a small mean free path, to prevent the electrons sufficient energy to ionize. Thus, it is easier to generate plasma with relatively low gas pressures. However, larger plasma areas were intended to be generated to increase the modification process efficiency, thereby increasing the MRR of PAP. In Ref. [5, 6], although local stable glow discharge plasma was generated and used at AP, the substrate was only locally irradiated by plasma per unit time, resulting in a very low surface modification efficiency. Furthermore, due to the high collision frequencies (high density of gas particles) at AP, spark, or arc discharge can easily occur, thus damaging the substrate. As a result, it is nearly impossible to generate a large stable glow discharge plasma at AP to improve the modification efficiency [8]. A relatively lower gas pressure (lower density of gas particles) can decrease the collision frequency, thus avoiding the formation of spark or arc discharges. In this work, vacuum plasma was proposed

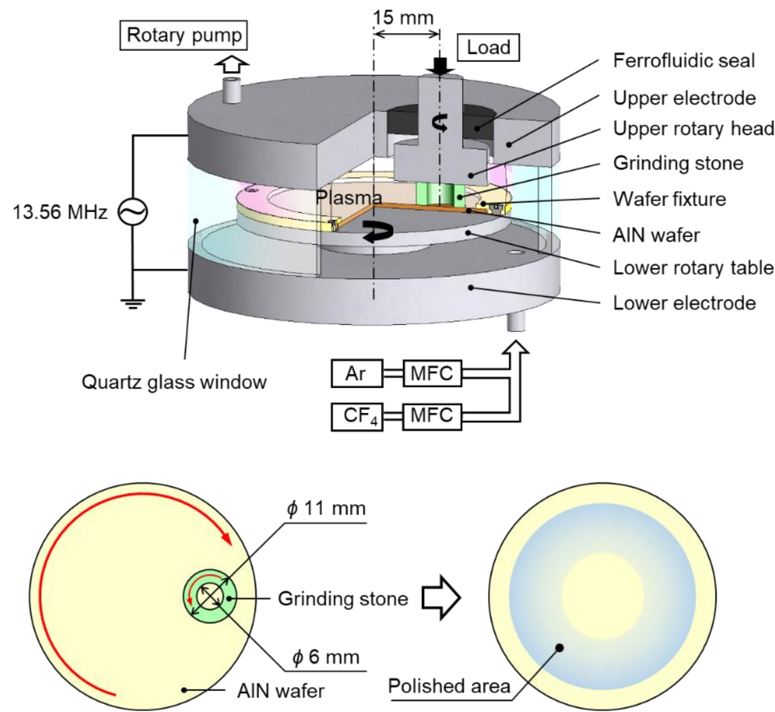

Figure 5.2 Schematic diagram of the vacuum PAP setup.

to be used instead of atmospheric-pressure plasma since a stable large area plasma can be easily generated with relatively lower gas pressures.

Figure 5.2 shows a schematic of the vacuum PAP setup used in this study. The setup comprises upper and lower metal electrodes made of aluminum alloy, and the area between them was separated from the atmosphere using a cylindrical quartz glass cover. The rotary pump was used to reduce the required pressure for plasma generation in this space. A ϕ 50 mm × 1.0 mm^t sintered AlN wafer was installed on the lower rotary table, and a vitrified-bonded diamond grinding stone (outer diameter = 11 mm, inner diameter = 6 mm, thickness = 6 mm) was set on the upper rotary head, whose center of rotation was offset by 15 mm from the center of rotation of the lower rotary table. Therefore, the area to be polished was ring-shaped, as shown in Fig. 5.2. The gap distance between the upper electrode and AlN wafer surface was 14 mm, and the Ar and CF_4 mixture was controlled using MFCs. By applying RF (f = 13.56 MHz) power on the upper electrode, plasma was generated in the space between the upper electrode and AlN wafer, and the grinding stone was pressed against the AlN wafer with a constant load. Through the rotation of the lower rotary table and upper rotary head, plasma irradiation and polishing were alternately conducted on the AlN wafer. Conventional mechanical polishing can also be carried out using this setup without applying RF power. Table 5.1 shows the detailed experimental conditions used in this work.

Table 5.1. Experimental conditions of dry polishing.

Parameters	**Conditions**
Experimental setup	Figure 5.2
Substrates	AlN ceramics (grinded surface)
Abrasive material	vitrified-bonded diamond (ϕ 0.25 µm)
Polishing pressure	800 Pa
Grinding stone rotation	121 rpm
Substrates rotation	100 rpm
Chamber pressure	800 Pa
Carrier gas	Ar (100 sccm)
Process gas	CF_4 (5 sccm)
Applied RF power	PAP: 100 W / Polishing without plasma: 0 W
Polishing time	30 mins × 6 times

5.3 Different fixed abrasive grinding stone distinguished according to the type of bond materials

As seen in Fig. 5.3, the fixed abrasive grinding stone generally contains the three main elements of abrasive particles, bond materials, and pore. Abrasive particles provide a uniform and dependable cutting action of the abrasive gains, and pore between abrasive particles controls the porosity which releases the heat from grinding and makes it easy for the rejection of the chips. Bond materials maintain a bonding effect between abrasive particles. According to the kind of bond materials, a fixed abrasive grinding stone can be divided into four types of stones: a resin- bonded grinding stone, a metal-bonded grinding stone, an electroplated monolayer grinding stone, and a vitrified-bonded grinding stone [9]. However, no matter which kind of fixed abrasive grinding stone is used, over a period after polishing, the abrasives undergo wear, and grinding stones get loaded and lose their

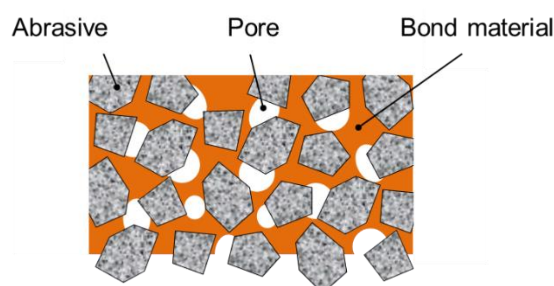

Figure 5.3 Schematic diagram of the fixed abrasive grinding stone.

polishing ability. In Ref. [6], although an atomically smooth pit-free GaN surface was obtained using PAP process, the loading of CeO_2 resin-bonded grinding stone greatly limits the MRR. Therefore, dressing grinding stones is essential to sustain efficient material removal processes [10, 11)]. Not every type of grindstone is suitable for PAP. With a resin-bonded grinding stone, the material used to bond the abrasives with the stone is mainly phenolic, which is cured over 200°C. Due to the large area of vacuum plasma, a grinding stone is inevitably exposed to plasma with high temperature. Thus, it is difficult to use resin-bonded grinding stones in vacuum PAP due to the relatively high temperatures. Metal bonds mainly use modified copper/tin and cobalt/bronze materials. Since CCP is used in vacuum PAP, the metal components in metal-bonded grinding stones and electroplated monolayer grinding stones cause the concentration of the electric field distribution. Partial arc discharge plasma could be easily generated at the location where the electric field distribution is concentrated. However, the vitrified-bonded (main component of binders is SiO_2) grinding stone is suitable for use in PAP.

5.4 Polishing properties of vitrified-bonded grinding stones with different abrasive particle sizes for conventional dry polishing method

Figure 5.4 shows the SEM images, SWLI image, and cross-sectional profile of the AlN surface after mechanical polishing was performed using a grinding stone with large size SiC abrasive particles, where the average abrasive particle size is 30 μm. As shown in the SEM image of the AlN surface, the average size of the AlN grains was 3 μm, and AlN was removed in units of AlN grains after polishing using large abrasives due to the weak intergranular interactions. Figure 5.4 indicates

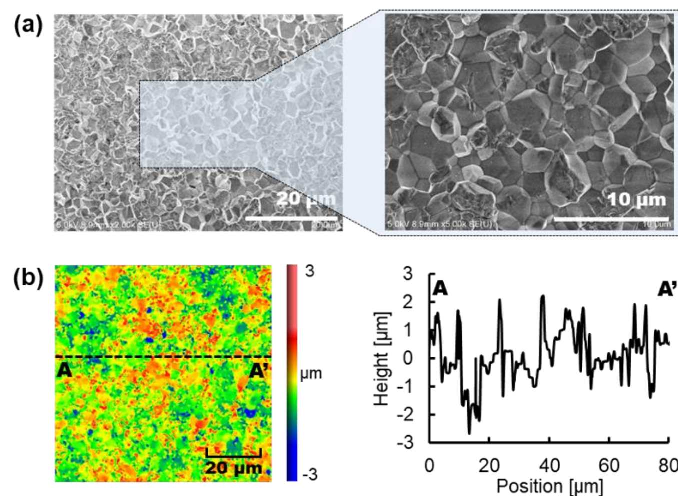

Figure 5.4 Surface morphology of the AlN after polishing using #600 abrasive. (a) SEM image, (b) SWLI image and cross-sectional profile.

that it is difficult to obtain smooth surfaces using mechanical polishing with large size abrasives due to the shedding of AlN grains. Wang *et al.* established equations describing the relationship between the polishing pressure and abrasive particle size and proved that the abrasive particle size is an important parameter of the polishing pressure. When smaller particle size abrasives were used with

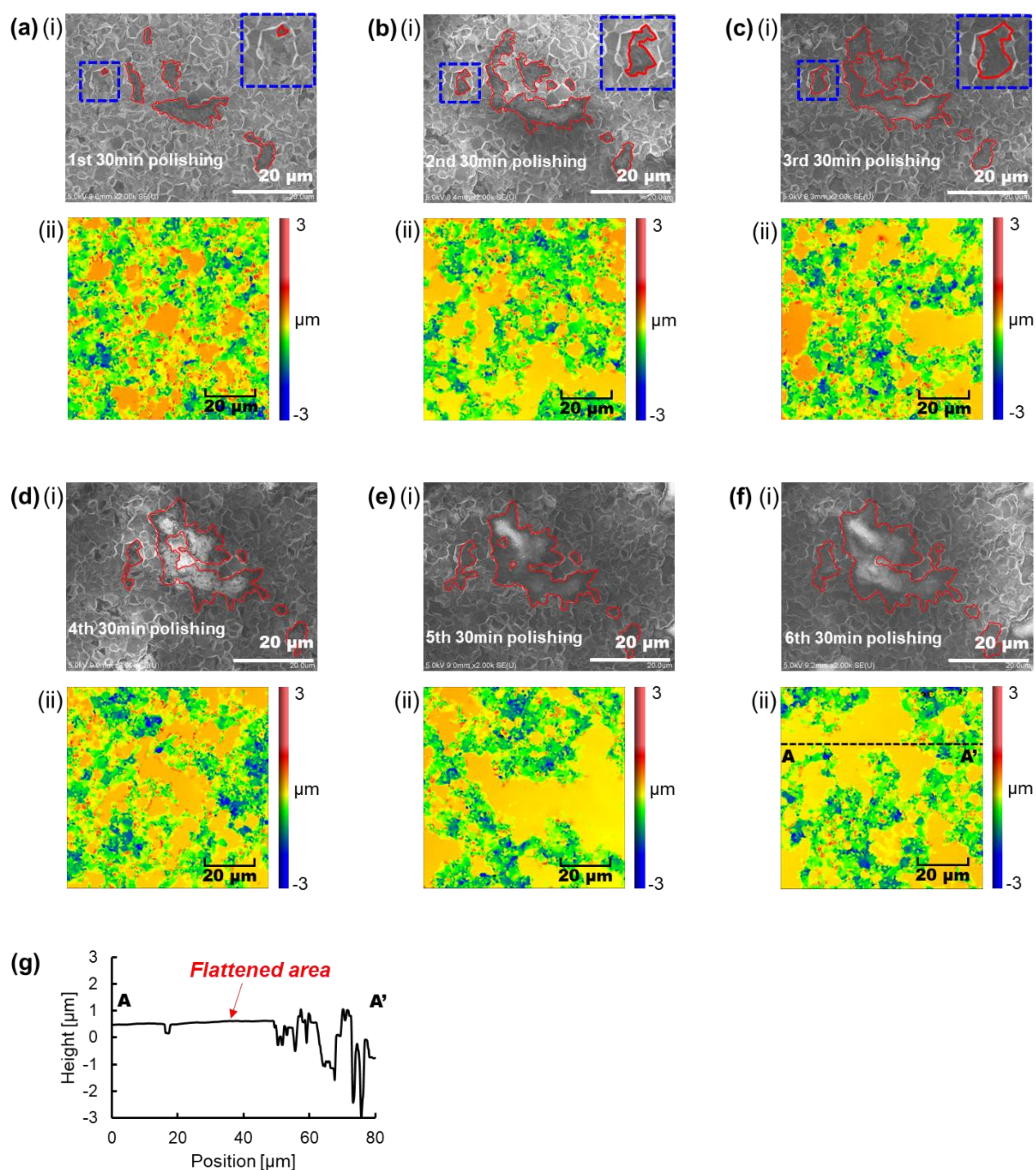

Figure 5.5 (i) SEM image and (ii) SWLI image of the AlN surface (a) after the 1st 30 min of dry polishing, (b) 2nd 30 min of dry polishing, (c) 3rd 30 min of dry polishing, (d) 4th 30 min of dry polishing, (e) 5th 30 min of dry polishing, (f) and 6th 30 min of dry polishing. (g) Cross-sectional profile of the AlN surface after the 6th 30 min of dry polishing.

a constant load, due to the increase in the number of abrasive grains per unit area, the polishing pressure acting on each abrasive became smaller [12, 13]. Thus, polishing experiments using a grinding stone with small size abrasive particles were conducted on the AlN wafer. Figures 5.5(a)–5.5(f) show an SEM image at the same position and an SWLI image of the AlN surface after polishing every 30 min under the experimental conditions shown in Table 5.1. Moreover, Fig. 5.5(g) shows the cross-sectional profile of the AlN surface after the 6th 30-min polishing process. In contrast to the polishing results when large size abrasive particles were used, as shown in the blue frame of Fig. 5.5(a–i), the AlN was flattened from the top of each AlN grain but not in units of AlN grains. With the increase in the polishing time, the flattened area of each AlN grain increased, and the flattened grains became more connected together, as shown in the red frame of Figs. 5.5(a)–5.5(f). Finally, a smooth AlN surface could be expected. Based on the above results, polishing sintered AlN wafers using vitrified-bonded grinding stones with different abrasive particle sizes can be modeled, as shown in Fig. 5.6. When the AlN wafer was polished using large size abrasive particles, the polishing pressure acting on each abrasive increased. The large polishing pressure led to a large tangential force larger than the intergranular interactions of the AlN grains, leading to the shedding of the AlN grains, and many pits were formed on the AlN surface, as shown in Fig. 5.6(a). In contrast,

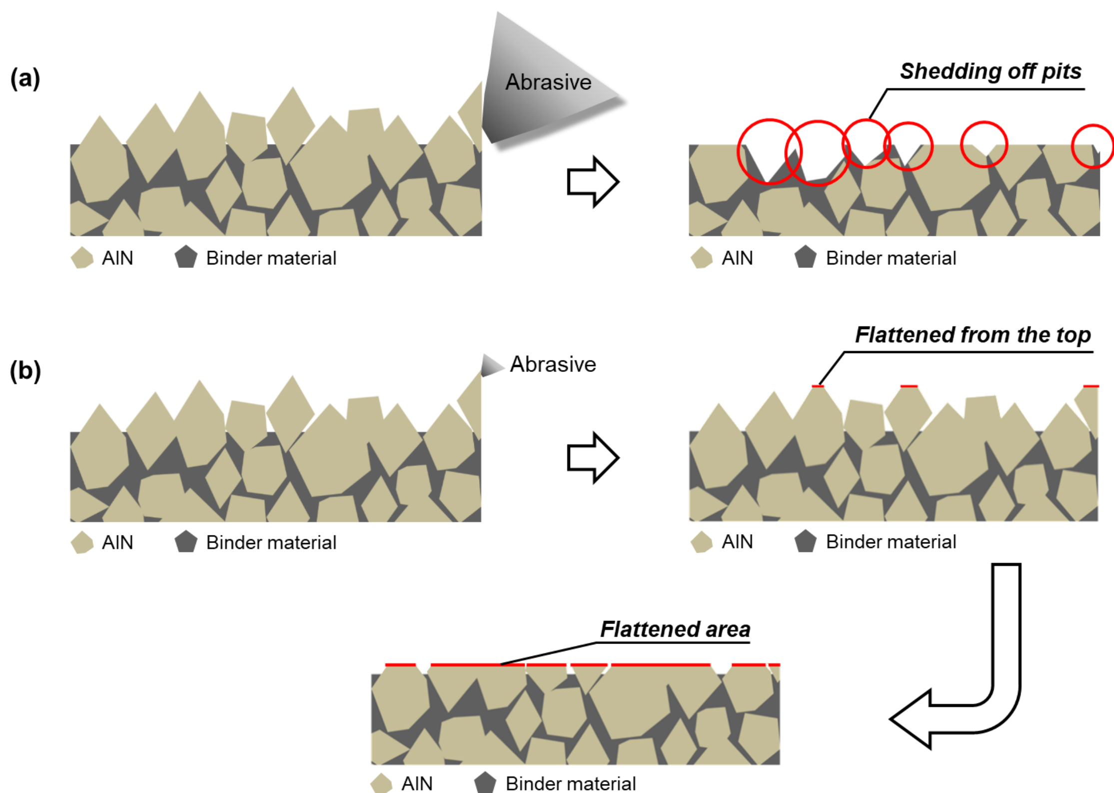

Figure 5.6 Models showing the mechanical dry polishing process for AlN using (a) large particle size abrasives and (b) small particle size abrasives.

when the AlN wafer was polished using small size abrasive particles, the polishing pressure acting on each abrasive particle was very small. Thus, the AlN grains did not shed off from the surface and were flattened from the top. As the flattened area became larger, a smooth AlN surface could be obtained, as shown in Fig. 5.6(b).

5.5 Loading of the grinding stone surface under ultralow polishing pressure

In the previous section, it has been confirmed that the shedding of AlN grains in a mechanical dry polishing process can be effectively suppressed using small size abrasive particles and ultralow polishing pressure. However, when polishing using a vitrified-bonded grinding stone, abrasives undergo wear and easily fall. Thus, over a period after polishing, a grinding stone surface easily gets loaded and loses its polishing ability. Currently, a dressing process, which mechanically removes the worn-out abrasive particles and bond material by applying external force to expose new abrasive particles, is necessary [10)]. However, dressing processes demand an interrupted polishing process, resulting in significant productivity losses. In recent years, many research were conducted to develop self-sharpening vitrified-bonded grinding stones to make the dressing phenomenon occur under the grinding force itself by weakening the bond strength [14)]. However, self-sharpening needs enough polishing force to break the bonds between abrasive particles, which does not work when only ultralow polishing pressure is applied. In this study, mechanical dry polishing experiments without dressing, mechanical dry polishing experiments with frequent dressing, and PAP experiments without dressing were conducted using a vitrified-bonded diamond grinding stone under ultralow polishing pressure. The MRRs were compared under different conditions, and each polishing mechanism was discussed. In this section, mechanical dry polishing experiments of AlN without dressing or plasma irradiation were conducted under the conditions shown in Table 5.1. The surface morphology of the grinding stone was observed every 30 min using SWLI and SEM, and the results are shown in Fig. 5.7. *S*dr (developed interfacial area ratio) was used to evaluate the surface condition of the grinding stone and is expressed as the percentage of a defined area’s additional surface area contributed by its texture in comparison with the planar definition area. However, the *S*dr of a completely flat surface is 0 [15)]. If many abrasive particles are exposed on the grinding stone surface, the *S*dr value will be large. At each stage of the experiment, four positions on the surface of the grinding stone were observed randomly, and the representative data are shown in Fig. 5.7. Figure 5.7(a) shows the SEM image (i) and SWLI image (ii) of the grinding stone surface after dressing using a diamond dress plate (average particle size is 10 μm). Many pores can be observed on the initial surface of the grinding stone, and the *S*dr value of the grinding stone surface was approximately 0.6. After 1 h of mechanical dry polishing, the *S*dr value from SWLI image did

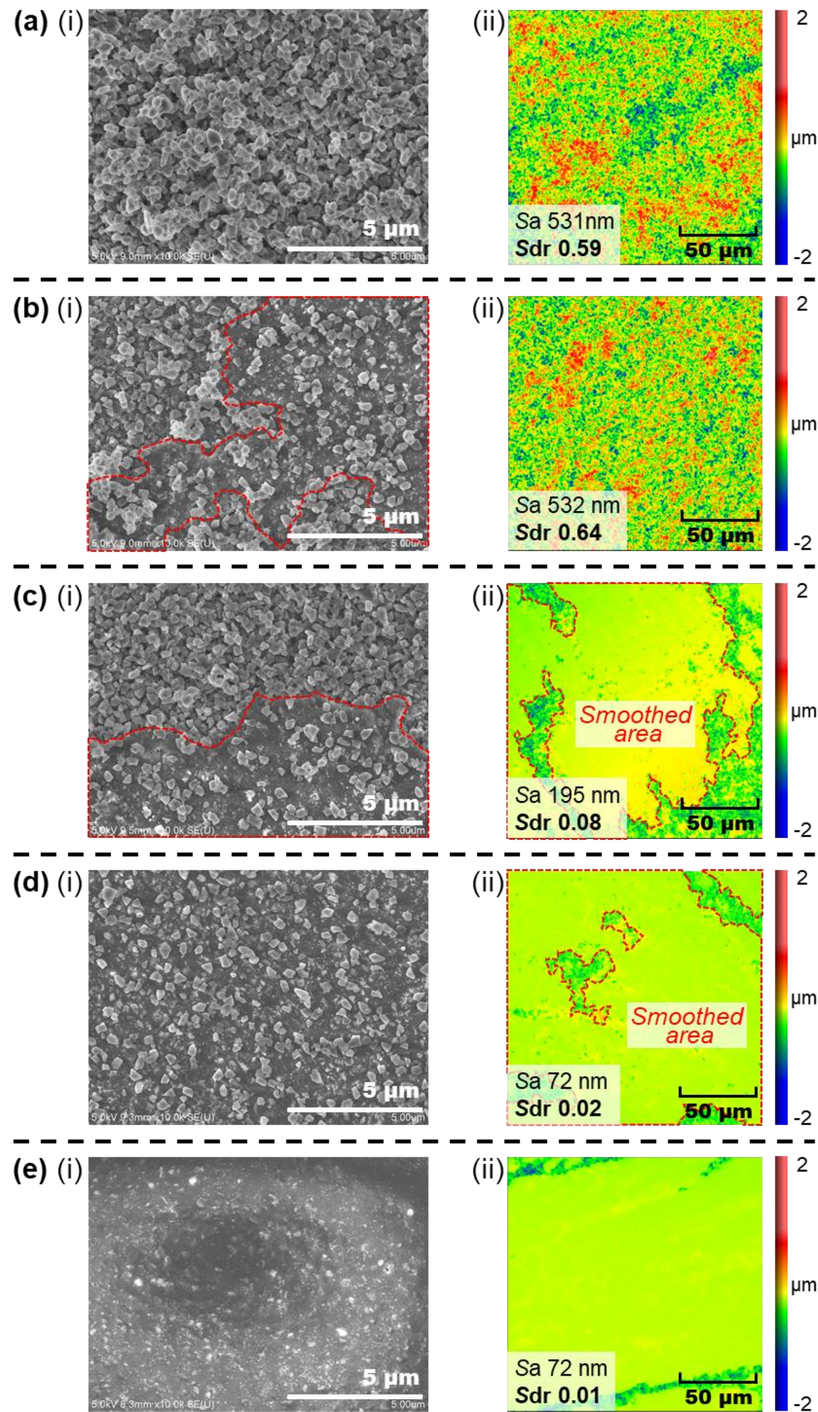

Figure 5.7 (i) SEM and (ii) SWLI images of the diamond grinding stone surface (a) after dressing using a diamond dress plate after (b) 1 h of dry polishing, (c) 2 h of dry polishing, (d) 3 h of dry polishing, and (e) after cleaning using N_2 gas blow.

not change significantly in the large-scale observation range, as shown in Fig. 5.7(b–ii). However, in the small-scale observation range using SEM, a part of the surface of the grinding stone became

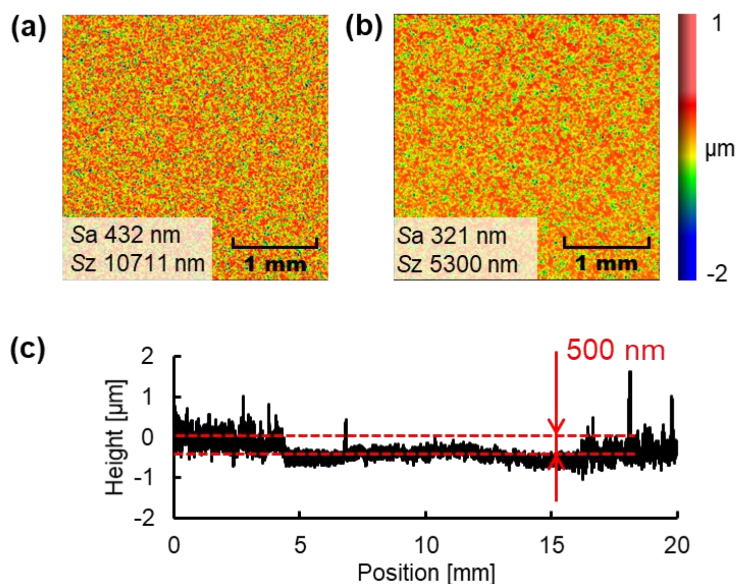

Figure 5.8 SWLI images of the AlN (a) before mechanical dry polishing and (b) after 3h of mechanical dry polishing. (c) Cross-sectional profile of the ring-shaped polished area.

smooth because the pores were filled with the falling abrasive particles, bond materials, and removed AlN chips, as shown in the area surrounded by the red frame of Fig. 5.7(b–i). Since only an ultralow polishing pressure was applied, self-sharpening did not occur. However, with the increase in the polishing time, the smoothed area on the grinding stone surfaces also increased, and the *S*dr of the grinding stone surface significantly decreased from 0.59 to 0.02, as shown in Figs. 5.7(c) and 5.7(d). However, some diamond abrasives could still be observed on the grinding stone surface after 3 h of polishing, as shown in Figs. 5.7(d–i). Since these abrasive particles were not fixed by a bond material, after simple cleaning using an N_2 gas blows, these abrasive particles, which had been recently adhered to the surface, were easily removed. As shown in Fig. 5.7(e), after cleaning, there were almost no abrasive particles with cutting edges exposed on the surface, meaning that the grinding stone lost its polishing ability and only slid on the AlN surface. Figures 5.8(a) and 5.8(b) show the SWLI images of the AlN surface before and after 3 h of mechanical dry polishing without plasma irradiation, and Fig. 5.8(c) shows the cross-sectional profile of the ring-shaped polished area measured by a stylus profiler. Since the grinding stone quickly lost its polishing ability due to the loading of its surface, the MRR was very low. The removal depth was only 500 nm, and the surface roughness *S*a only decreased from 432 to 321 nm.

5.6 Increase in MRR by dressing the surface of the grinding stone and cleaning the surface of AlN ceramics wafer

It has been confirmed that the surface of grinding stones gets easily loaded during mechanical dry polishing processes with ultralow polishing pressure. Thus, to maintain the polishing ability of grinding stones, frequent dressing is necessary. In this section, mechanical dry polishing experiments without plasma irradiation were conducted under the conditions shown in Table 5.1, while the surface of the used grinding stone was dressed using a diamond dress plate (average particle size was 10 μm), and the used AlN wafer was cleaned using isopropyl alcohol (IPA)

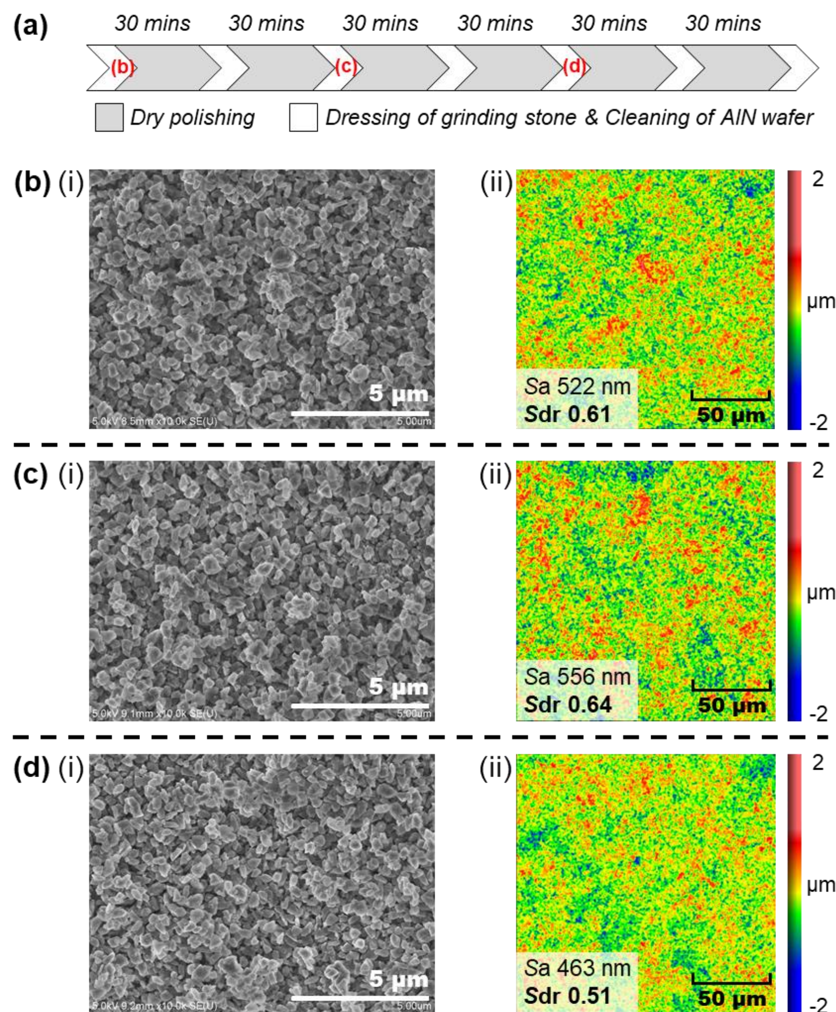

Figure 5.9 (a) Experimental procedure and (i) SEM and (ii) SWLI images of the diamond grinding stone surface (b) before the 1st 30-min of polishing, (c) 3rd 30-min of polishing, and (d) 5th 30-min of polishing.

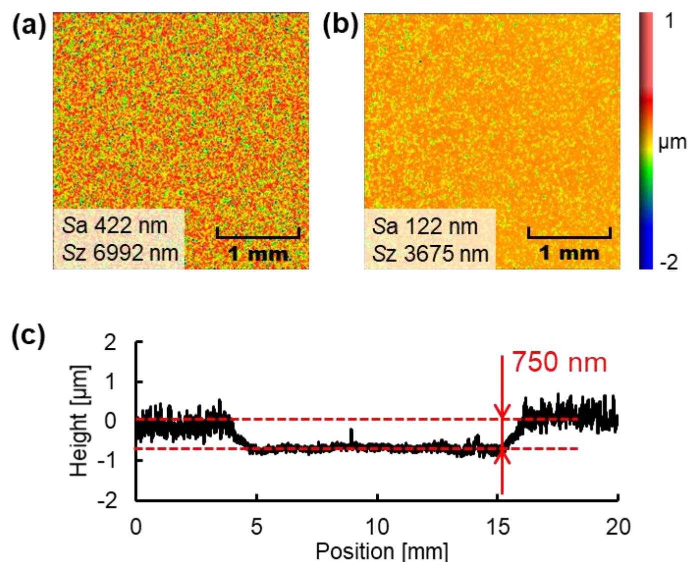

Figure 5.10 SWLI images of the AlN (a) before dry polishing and (b) after 3 h of dry polishing. (c) Cross-sectional profile of the ring-shaped polished area.

ultrasonic cleaning every 30 min, as shown in Fig. 5.9(a). To represent the surface morphology of each stage, Figs. 5.9(b)–5.9(d) show the SEM (i) and SWLI images (ii) of the grinding stone surface before the 1st 30-min polishing, before the 3rd 30-min polishing, and before the 5th 30-min polishing, which were after dressing. Before each 30-min mechanical dry polishing process, the surface of the grinding stone was confirmed to be in the best state, where enough abrasive particles with cutting edges were exposed and without loading, and the *S*dr values of the grinding stone surface were all approximately 0.6. Figures 5.10(a) and 5.10(b) show the SWLI images of the AlN surface before and after 3 h of mechanical dry polishing without plasma irradiation, and Fig. 5.10(c) shows the cross-sectional profile of the ring-shaped polished area. Since the grinding stone surface was dressed in time before getting loaded, it was considered that an effective polishing process was being conducted all the time. The surface roughness *S*a decreased from 422 to 122 nm, and the removal depth was 750 nm, which is larger than in the case without grinding stone dressing.

5.7 Self-sharpening technique of metal-bonded grinding stones using electrolytic in-process dressing (ELID)

It has been confirmed that the frequent dressing of grinding stones is very effective and necessary in maintaining the MRR in fixed abrasive polishing processes with ultralow polishing pressure. However, frequent dressing impacts both the processing efficiency and tooling costs. Thus, a dress-free polishing technique is desired.

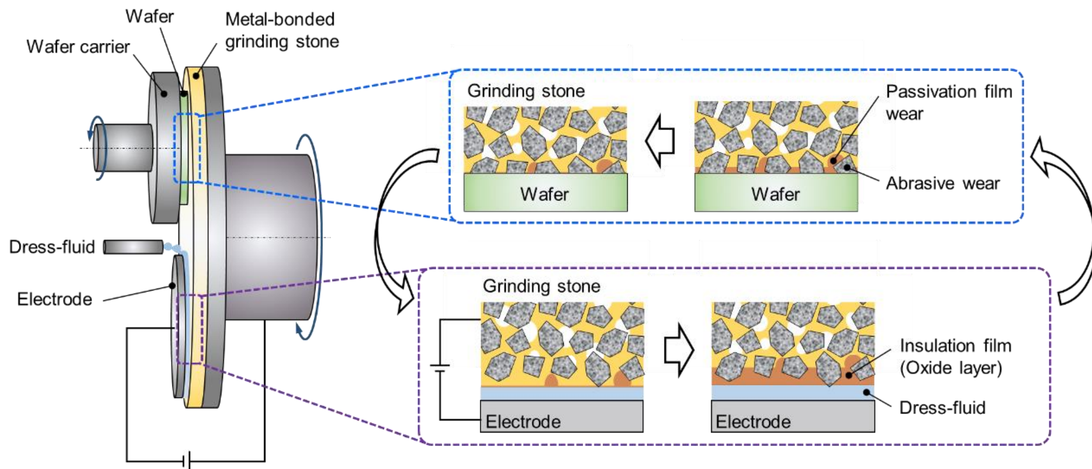

Figure 5.11 Schematic diagram of a typical setup and mechanism of ELID-grinding method.

H. Ohmori *et al*. developed the self-sharpening technique of metal-bonded grinding stones using electrolytic in-process dressing (ELID) [16, 17]. Figure 5.11 shows the schematic diagram of a typical setup and mechanism of ELID-grinding method. A metal-bonded grinding stone made by sintering abrasive particles and bond material with cast iron as the main component was used. The electrode plate used for ELID was placed with a 0.1–0.3 mm gap from the grinding stone. At first, the surface of grinding stone had good electro-conductivity. Therefore, the current was as high between the electrode plate and grinding stone. After several minutes passed, the bond material (mainly cast iron) was removed by the electrolysis (mostly ionized into Fe^{2+}), and an appropriate amount of abrasive particle protrusion was obtained. The ionized Fe made hydro-oxide substances $Fe(OH)_2$ or $Fe(OH)_3$. Next, this substance changed into an oxide substance Fe_2O_3 by the help of the electrolysis of water. After these reactions occurred, the electro-conductivity of the surface of the grinding stone was reduced in accordance with the growing of the oxide layer. Thereby, the current decreased. At this time, the initial dressing was completed. When the grinding process was started from this state, the protruded abrasives grind the substrate. As the abrasives wear, at the same time the oxide layer also became worn. The wear of the oxide layer caused an increase in the electro-conductivity of the grinding stone surface. And thus the electrolysis increased and the oxide layer was recovered. The protrusion of the abrasives was therefore remained constant in a general sense [17]. Although ELID-grinding method has been successfully applied to the grinding of many materials [18-20], it was difficult to be applied in dry PAP process since dress-fluid was necessary for ELID. Furthermore, in PAP process, the metal components in metal-bonded grinding stones would cause the concentration of the electric field distribution. Partial arc discharge plasma could be easily generated at the location where the electric field distribution concentrated. Thus, a new dress-free process like ELID that can be used in PAP is desired.

5.8 Modification of AlN ceramics wafer by Ar-based CF_4 plasma irradiation

As the removal mechanism of AlN in the PAP process, AlN was first modified by plasma irradiation to make a modified layer on the AlN surface and subsequently removed it using abrasive. Table 5.2 shows the oxidation–reduction potential of different oxidizing species [21)]. Fluorine atoms have the strongest oxidation–reduction potential. Therefore, it is considered that if the surface of AlN are exposed to plasma containing CF_4, surface modification will occur easily. Table 5.3 shows the conditions used for plasma modification using CF_4 gas. Figure 5.12 shows the optical emission spectroscopy (OES) spectrum of the Ar-based CF_4 plasma generated during the plasma irradiation. Optical emission from Ar, OH, N_2, and F (739.9 nm) were obtained from the spectrum. Fluorine radicals were generated by the dissociation of CF_4, and OH and N_2 were generated from the air (H_2O and N_2). Since fluorine radicals have a high oxidation potential, efficient modification of AlN is expected. The surface composition of AlN was analyzed by XPS before and after CF_4 plasma irradiation. As shown in the Figs. 5.13(a) and 5.13(b), only Al–N (73.7 eV [22-24)]) and Al–O (74.6 eV [22-24)]) peaks were observed from the Al2p spectrum, and no peak attributed to the fluorine compound was observed from the F1s spectrum of the AlN surface before plasma irradiation. After 2 h of plasma irradiation, a strong peak corresponding to Al–F_3 (76.3 eV [25)]) was observed in both the Al2p and F1s spectra, as shown in the Figs. 5.13(c) and 5.13(d). This result showed that AlN was modified

Table 5.2 Oxidation-reduction potential.

Radicals	F	OH	O	O_3	H_2O_2	ClO_2	Cl_2
Oxidation-reduction potential (V)	3.03	2.80	2.42	2.07	1.78	1.49	1.36

Table 5.3 Experimental conditions of plasma irradiation.

Parameters	**Conditions**
Experimental setup	Figure 5.2
Substrates	AlN ceramics (grinded surface)
Carrier gas	Ar (100 sccm)
Process gas	CF_4 (5 sccm)
Chamber pressure	800 Pa
Applied RF power	100 W
Irradiation time	1 hours

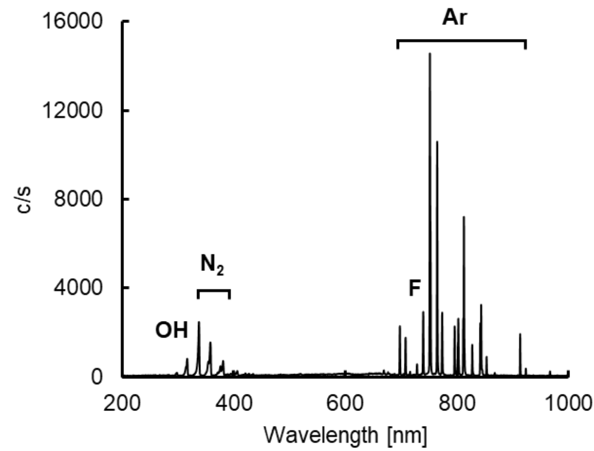

Figure 5.12 OES spectrum of the Ar-based CF_4 plasma used in this study.

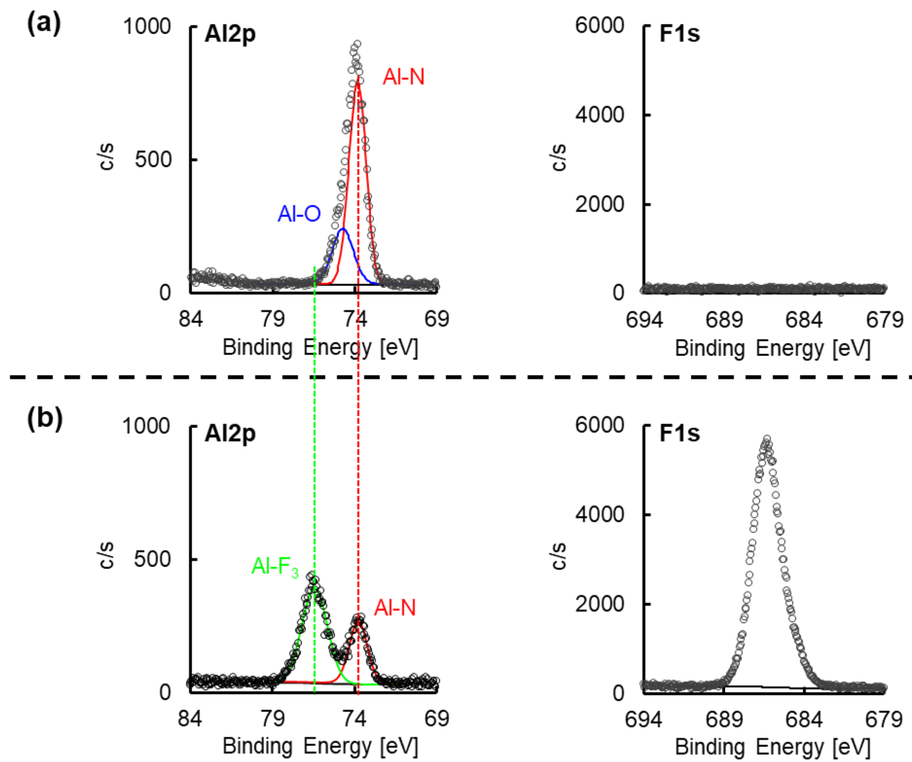

Figure 5.13 XPS spectra of AlN (a) Al2p spectra of AlN before plasma irradiation (b) F1s spectra of AlN before plasma irradiation (c) Al2p spectra of AlN surface after 1 h of plasma irradiation (d) F1s spectra of AlN after 1 h of plasma irradiation.

to AlF_3 by the irradiation of Ar-based CF_4 plasma.

.

5.9 Selection of abrasive material used in PAP

As discussed in section 5.3, the vitrified-bonded (main component of binders is SiO_2) grinding stone is suitable for use in PAP. And the Ar-based CF_4 plasma was confirmed to be very effective to modify AlN surface in section 5.8. And the choice of abrasive material used in PAP will be discussed in this section. As for the abrasive of vitrified-bonded grinding stone, diamond, SiC, silica (SiO_2), ceria (CeO_2) are commonly used. In our previous research, PAP, which used soft abrasives, has been proven to be very effective with regards obtaining atomically smooth surfaces of difficult-to-machine materials without forming subsurface damage [5,6]. Thus, the polishing characteristics of AlN ceramics wafer using soft abrasives #8000 SiO_2 (average particle size 1 μm) and #8000 CeO_2 (average particle size 1 μm) in PAP were investigated. Table 5.4 shows the detail experimental conditions of PAP. Figure 5.14 shows the SWLI images of the AlN and the photograph of the grinding stone before and after 2 h of PAP using silica abrasives. Since the F radicals dissociated from CF_4 have strong reactivity, CF_4 was often used as a process gas in PCVM to etch materials such as quartz glass or SiC wafer. In the PAP process using CF_4 plasma, not only AlN was modified by the irradiation of CF_4 plasma, but silica (SiO_2) abrasives were also etched by CF_4 plasma and became volatile reaction products, thereby losing the polishing ability as abrasives. Thus, as shown in Fig. 5.14, there was almost no change in the surface roughness of AlN ceramics before and after PAP. In addition, since the grinding stone was also exposed to CF_4 plasma, the diameter of the grinding stone was reduced from 11.37 to 10.87 mm because the silica abrasives were etched. For

Table 5.4 Experimental conditions of PAP.

Parameters	Conditions
Experimental setup	Figure 5.2
Substrates	AlN ceramics (polished surface)
Abrasive material	vitrified-bonded silica or ceria
Polishing pressure	800 Pa
Grinding stone rotation	121 rpm
Substrates rotation	100 rpm
Chamber pressure	800 Pa
Carrier gas	Ar (100 sccm)
Process gas	CF_4 (5 sccm)
Applied RF power	PAP: 100 W
Polishing time	2 hours

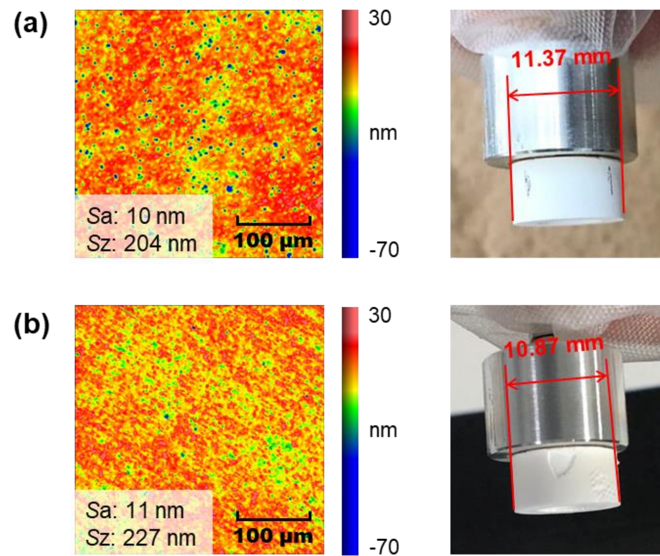

Figure 5.14 SWLI images of the AlN and photograph of silica grinding stone (a) before PAP and (b) after 2 h of PAP.

the same reason, SiC abrasives were also considered unsuitable for PAP process using CF_4. PAP experiment using another soft abrasive ceria (CeO_2) was also conducted on AlN ceramics under the same conditions. Different from the polishing results using silica abrasives, since ceria cannot be etched by CF_4 plasma, polishing ability of ceria abrasives was maintained. However, the surface

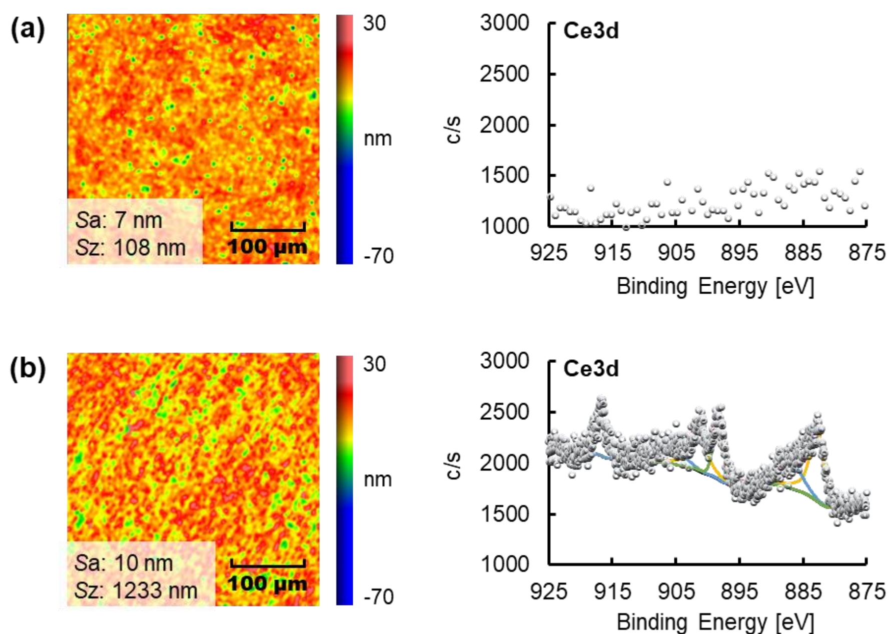

Figure 5.15 SWLI images and Ce3d-XPS spectra of the AlN (a) before PAP and (b) after 2 h of PAP using ceria abrasives.

roughness of AlN ceramics became larger than before PAP as shown in Fig. 5.15. By comparing the XPS spectra on the AlN surface before and after PAP, it can be found that peaks, which were not detected before PAP, were observed from the Ce3d spectrum. This was that ceria abrasives adhered to the AlN surface during PAP process and hindered the modification of the AlN surface by plasma, thereby interrupting the PAP process, and ultimately led to the deterioration of the surface roughness. According to the above results, several commonly used abrasives such as silica, SiC, and ceria have been proved to be unsuitable for PAP process using CF_4 due to various reasons, and chemically inert diamond abrasives have become the best candidate abrasive material. The polishing characteristics of AlN ceramics using diamond abrasives in PAP will be discussed details in the following sections.

5.10 Change of adhesion force between diamond abrasive particles and AlN ceramics surface after Ar-based CF_4 plasma irradiation

To investigate the effect of the AlF_3 modified layer formed on the AlN surface after CF_4 plasma irradiation on the PAP process, the adhesion force between the diamond abrasive particles and AlN ceramics surface before and after the plasma modification was compared. Recently, AFM has been used to characterize the particle-surface adhesion force through the measurement of force-distance curves [26, 27]. Figure 5.16 shows a schematic diagram of the force-distance curve. The force-distance curve can be divided into two different segments where ①-③ refers to motion where the tip is approaching the surface and ④-⑥ is when the tip is retracting from the surface [28]. In the force-distance curve measurement, the zero force is defined as the position of the cantilever beam when the sample is very far away, and

① Cantilever is approaching the surface. If there are attractive or repulsive forces between the tip and the sample, those could be measured in this segment by the down or up bending of the cantilever.

② Snap-in at some critical distance the tip feels an attractive force from the surface and falls quickly toward the surface until contact [27, 29].

③ Repulsive portion: the tip and sample are in contact and bends up upon further movement until reach to the setted z-position. This section is referred to as the net-repulsive portion.

④ Repulsive portion on withdrawal: the tip is unbending while releasing from the surface after reached to the setted z-position.

⑤ Pull-out: The tip will adhere during the release process until the force exerted by the cantilever is enough to break the adhesion and jump out.

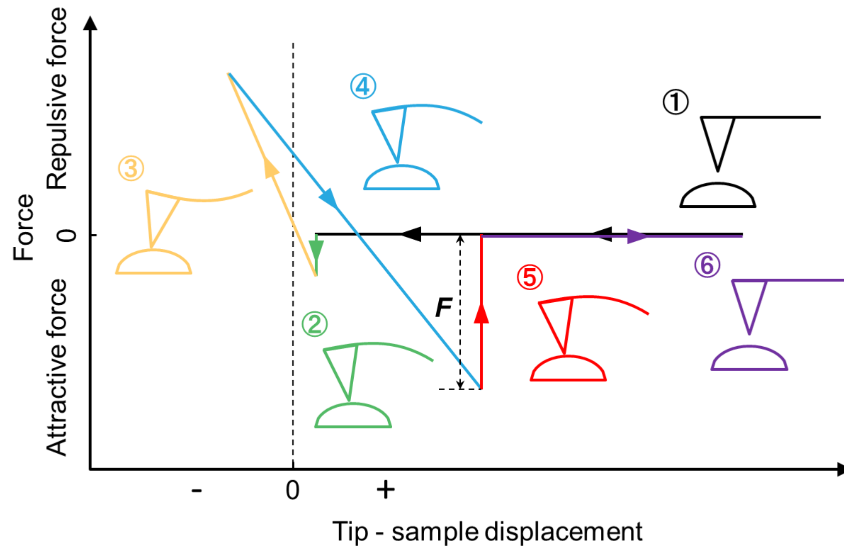

Figure 5.16 Schematic diagram of the force-distance curve using AFM.

⑥ The cantilever has returned to its unperturbed state while the further increases of the tip-sample distance.

The force *F* is the adhesion force between the tip and material surface. In addition to the adhesion force itself, the partial pressure of water vapor (relative humidity, RH) of the measure environment will also affect the value of adhesion force shown in the force-distance curve [30]. D. B. Asay *et al.* has reported that as RH increased, the adhesion force measured with an AFM initially increases, reached a maximum, and then decreased at high RH [30]. Therefore, in the measurement in this work,

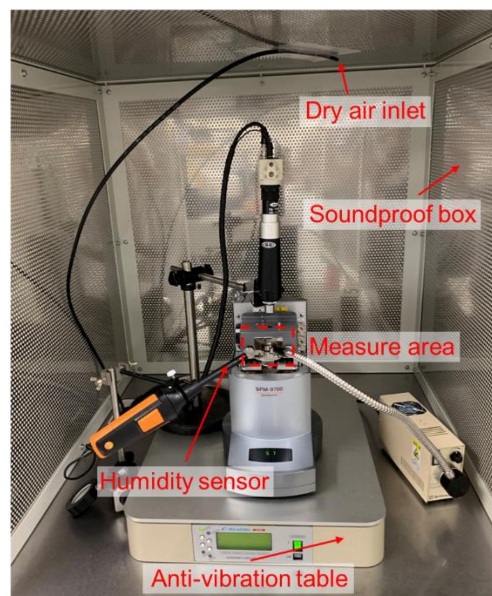

Figure 5.17 AFM used for adhesion force measurement.

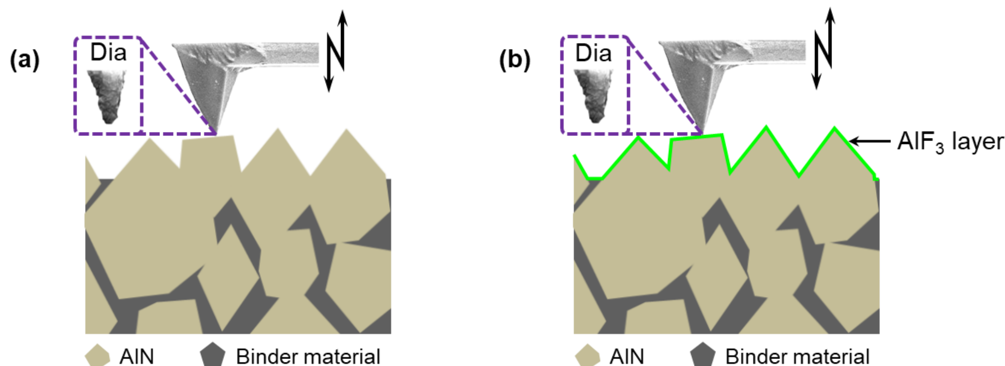

Figure 5.18 Schematic diagram of force-distance curve measurement on AlN wafer using diamond coated tip (a) before and (b) after CF_4 plasma irradiation.

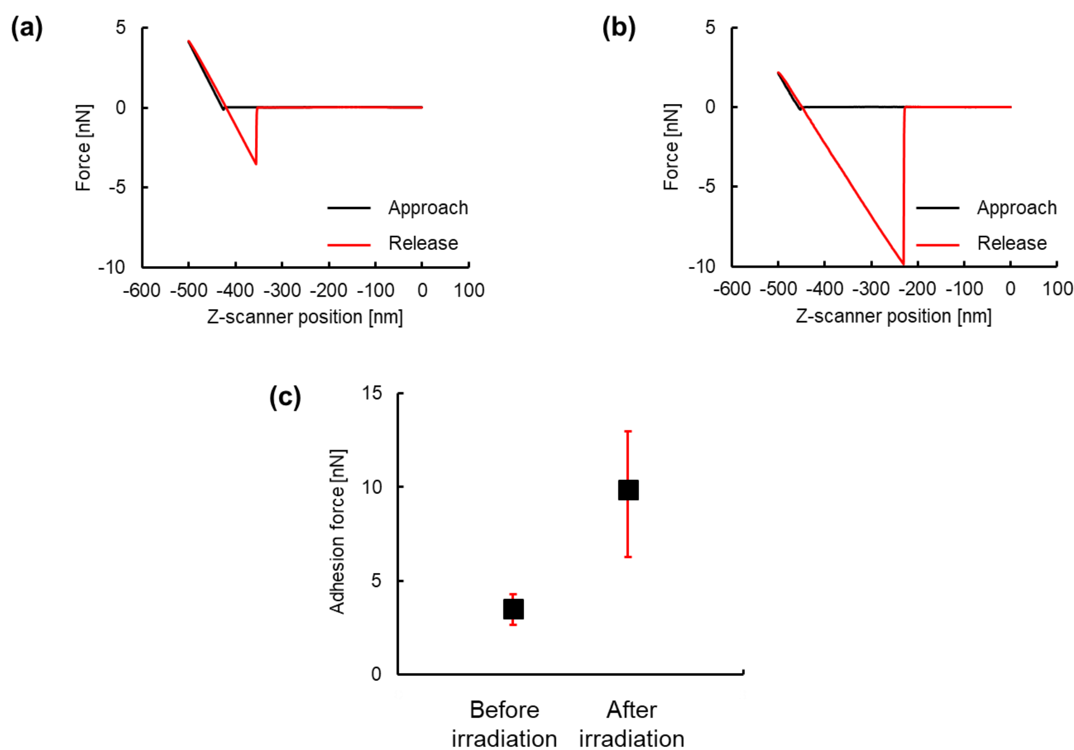

Figure 5.19 The representative force-distance curve between diamond tip (a) before and (b) after CF_4 plasma irradiation, and (c) the variation in adhesion force.

to eliminate the influence of RH of the measure environment on the measurement results, as shown in Fig. 5.17, the AFM (SPM-9700, SHIMADZU) was placed in a soundproof box. To reduce and stabilize the RH of the measure environment, the RH in the soundproof box was controlled by the dry air stream. The flow rate of dry air was controlled in 20 slm by a mass flow

controller, and the RH was monitored in real time by the Humidity sensor (TESTO 440). All measurements were conducted at 26.1℃ after the RH stabilized at 10%.

As shown in Fig. 5.18, a single-crystal diamond coated tip (Artech Carbon-ART D10) was used to measure the force-distance curve of AlN. And the changes of adhesion force between diamond abrasive particles and AlN surface before and after CF_4 plasma irradiation were investigated. The adhesion force between diamond tip and AlN wafer was randomly measured at 25 positions on the AlN wafer before and after CF_4 plasma irradiation. The representative force-distance curve on each state and the variation in adhesion force is shown in Fig. 5.19. The adhesion force between diamond tip and AlN wafer was significantly increased after CF_4 plasma irradiation from 3.5 nN to 9.9 nN. Therefore, during the actual PAP process, it is considered that the adhesion force between the diamond abrasive particles and the AlF_3 modified layer was also increased, which made the AlF_3 modified layer can be removed much easier than before plasma irradiation.

5.11 Dress-free polishing of AlN ceramics wafer in PAP

5.11.1 Preliminary polishing of AlN grinded surface

In comparison with conventional mechanical dry polishing, preliminary PAP experiments were also conducted on grinded AlN wafer under the conditions shown in Table 5.1 without dressing the used grinding stone. As a type of process gas with high oxidation potential, CF_4 is widely used for etching Si, SiC, and SiO_2. Here are the chemical reactions occurring during the etching process [31, 32].

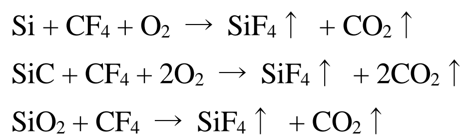

$$Si + CF_4 + O_2 \rightarrow SiF_4\uparrow + CO_2\uparrow$$
$$SiC + CF_4 + 2O_2 \rightarrow SiF_4\uparrow + 2CO_2\uparrow$$
$$SiO_2 + CF_4 \rightarrow SiF_4\uparrow + CO_2\uparrow$$

Before the PAP experiments, the grinding stone was dressed using a diamond dress plate. Figure 5.20 shows the SEM and SWLI images of the grinding stone surface at each stage, and Fig. 5.21 shows the variation in *S*dr values of grinding stone during different polishing processes. In contrast to the results without plasma irradiation, as described in section 5.5, no loading of the grinding stone surface was observed, which was similar to the results of dressing every 30 min in section 5.6. Diamond abrasives with cutting edges were exposed on the surface of the grinding stone all the time, and the *S*dr values were kept at approximately 0.6. Because the main component of the bond materials of the vitrified bond is SiO_2, it was able to react with fluorine radical generated by the dissociation of CF_4 in plasma to create volatile reaction products such as SiF_4 and to evaporate from the surface of the grinding stone. The worn-out abrasive particles fell off because of the etched the bond materials, and new abrasive particles were constantly exposed. The PAD process occurred all

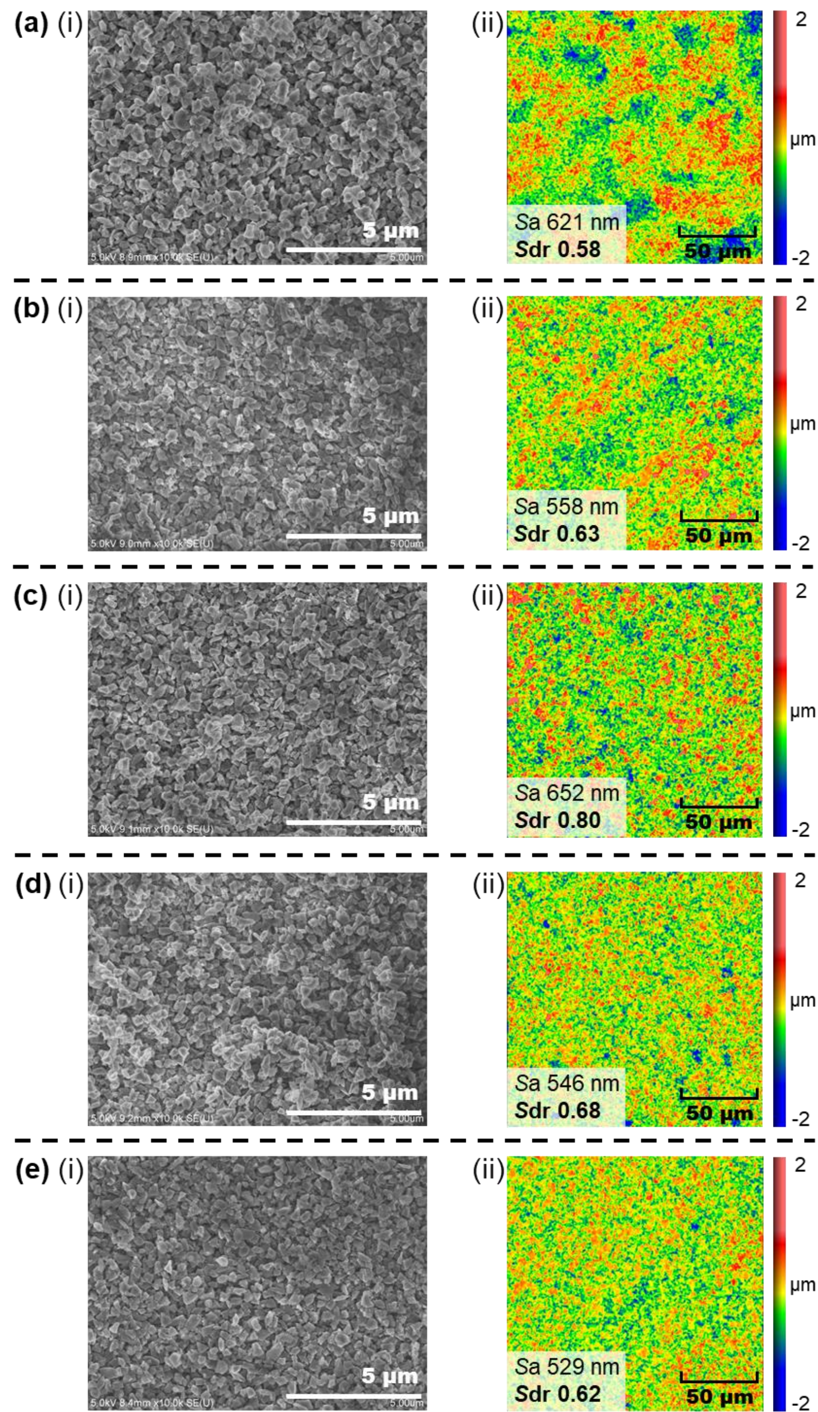

Figure 5.20 (i) SEM and (ii) SWLI images of the diamond grinding stone surface (a) after dressing using a diamond dress plate, (b) after PAP for 1 h, (c) after PAP for 2 h, (d) after PAP for 3 h, (e) and after cleaning using N_2 gas blow.

the time during the whole PAP process, and the etching rate of bond materials was fast enough to keep the grinding stone from being loaded.

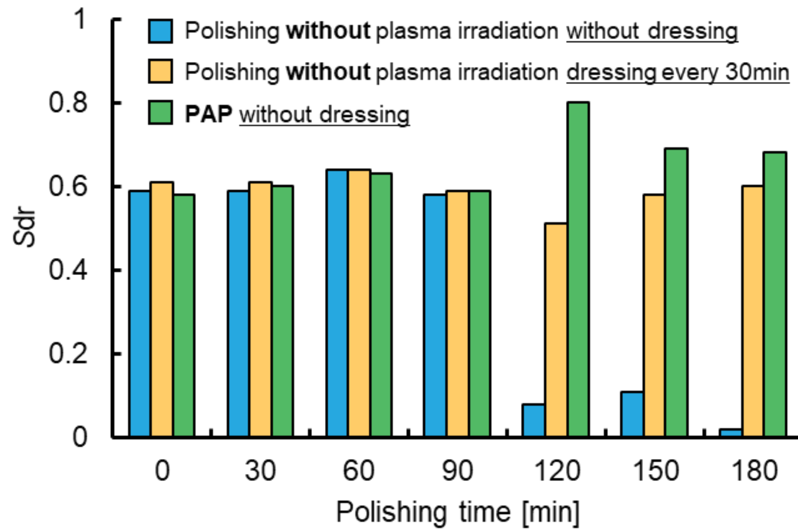

Figure 5.21 Variation in *S*dr values of grinding stone during different polishing processes.

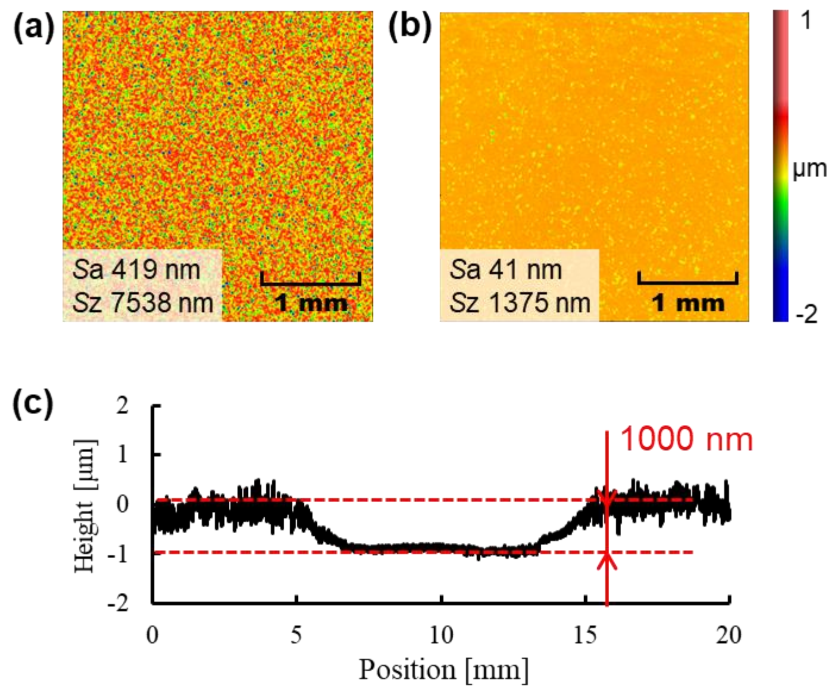

Figure 5.22 SWLI images of the AlN (a) before PAP and (b) after PAP for 3 h. (c) Cross-sectional profile of the ring-shaped polished area.

Figures 5.22(a) and 5.22(b) show the SWLI images of the AlN surface before and after PAP for 3h, and Fig. 5.22(c) shows the cross-sectional profile of the ring-shaped polished area. Although the

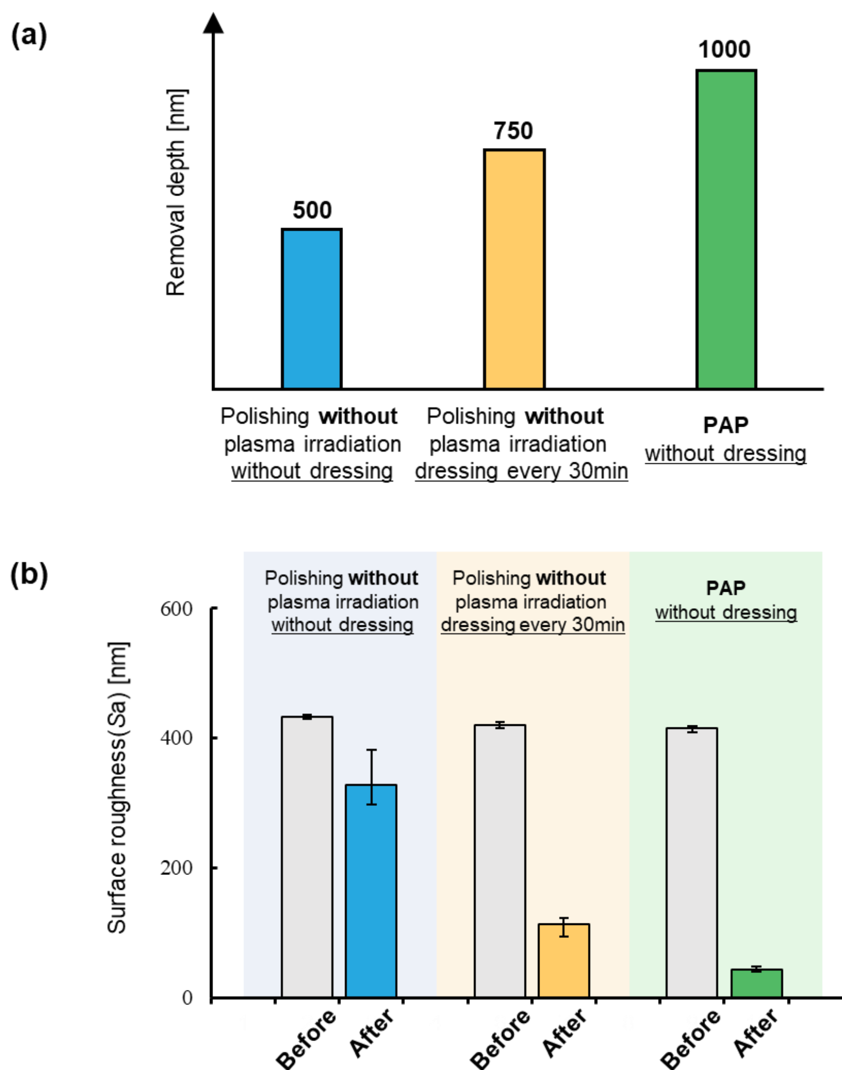

Figure 5.23 (a) Removal depth and (b) variation in the surface roughness of AlN wafer before and after different polishing processes.

grinding stone surface was not actively dressed during the 3-h PAP process, it was always maintained in a good state due to PAD. In the case of PAP, the consumed time by frequent dressing was saved, thus greatly improving the processing efficiency. After the CF_4 plasma irradiation, the AlN was modified to AlF_3, and its modified layer could be easily removed by the diamond abrasives as discussed in section 5.10. Thus, a much deeper removal depth (1000 nm) was realized, as shown in Fig. 5.22(c), and the surface roughness *S*a decreased from 419 to 41 nm. Figure 5.23 shows the removal depth and variation in the surface roughness of AlN wafer before and after different polishing processes.

To confirm the above hypothesis, XPS measurements of the grinding stone and AlN wafer surface

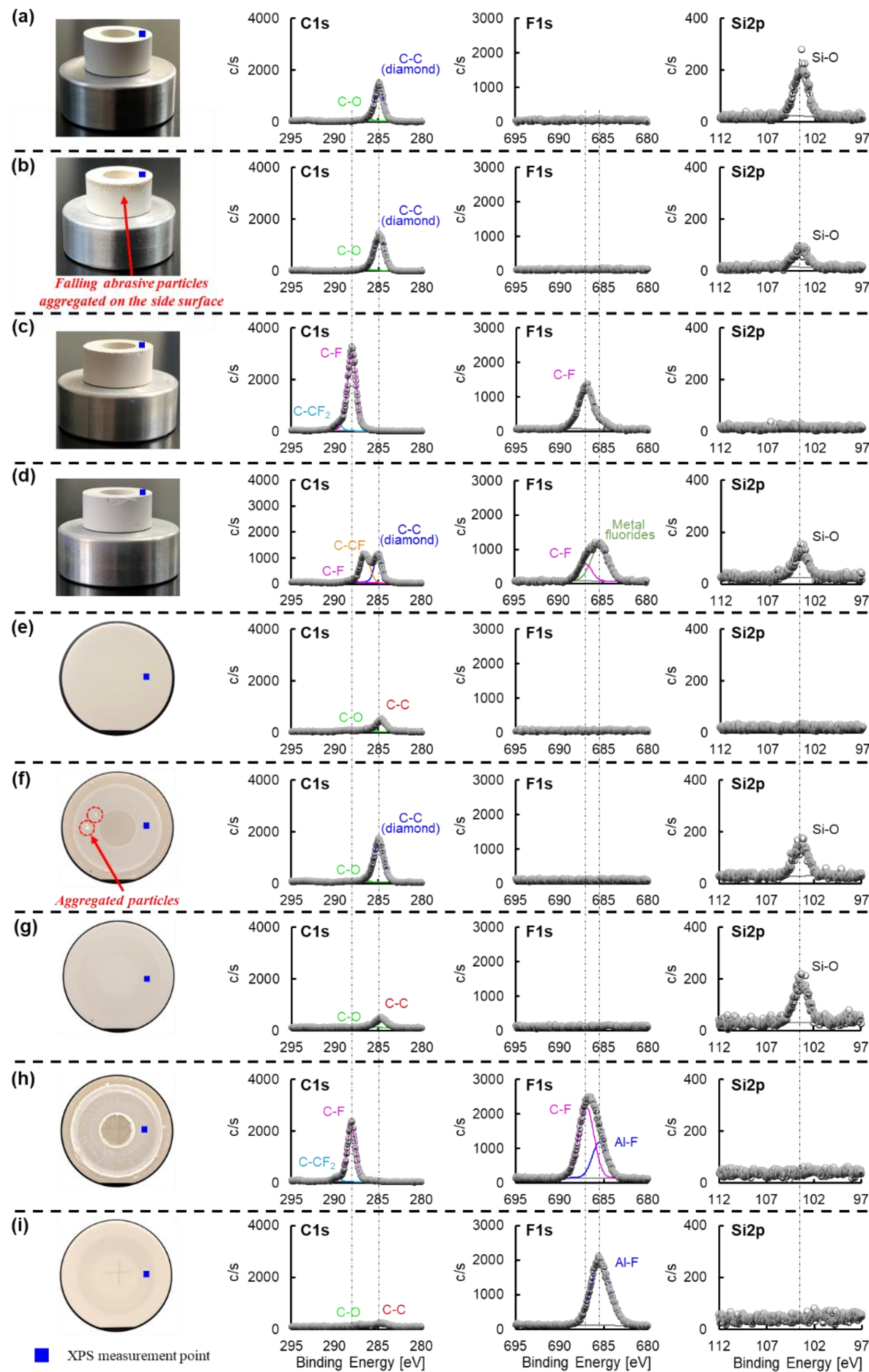

Figure 5.24 Photograph and XPS spectra of the (a) initial grinding stone, (b) grinding stone after conventional mechanical dry polishing, (c) grinding stone after PAP, (d) grinding stone after PAP and cleaning using N_2 gas blows, (e) initial AlN wafer, (f) AlN wafer after conventional mechanical dry polishing, (g) AlN wafer after conventional mechanical dry polishing and IPA ultrasonic cleaning, (h) AlN wafer after PAP, and (i) AlN wafer after PAP and IPA ultrasonic cleaning.

before and after conducting conventional mechanical dry polishing and PAP were performed. Figure 5.24(a) shows a photograph and XPS spectra of the grinding stone initial surface. A C–C (285.0 eV [33, 34]) peak attributed to the diamond abrasive particles and a Si–O (103.5 eV [35]) peak attributed to the bond materials were observed from the C1s and Si2p spectra, and no peaks attributed to the fluorine compound were observed from the F1s spectrum. As for the initial surface of the AlN surface, as shown in Fig. 5.24(e), only a weak C–C (284.8 eV [36]) peak attributed to organic contamination was observed from the C1s, and no peaks attributed to the fluorine and silicon compounds were observed from the F1s spectrum and Si2p spectrum. After the conventional mechanical dry polishing process, the chemical state of the grinding stone components was not changed, as shown in the XPS spectrum in Fig. 5.24(b). The grinding stone components were also observed on the AlN surface, as shown in Fig. 5.24(f). It was considered that the abrasive particles and bond materials falling from the grinding stone were accumulated on the AlN surface. Since the falling bond materials can also fix abrasive particles, the falling abrasive particles were agglomerated on the AlN wafer and on the grinding, stone surfaces, as shown in Figs. 5.24(b) and 5.24(f). Agglomerated abrasive particles have always been responsible for scratch formation in polishing processes. As shown in Fig. 5.24(g), although the abrasive particles were removed, the bond materials could not be removed after a simple IPA ultrasonic cleaning process. Thus, an additional cleaning process had to be conducted to remove the bond materials. As a comparison, in the case of PAP, the surface of the diamond abrasive particles was modified to CF_x because a strong peak corresponding to C–F (288.0 eV [37]) was observed, and most importantly, no peaks attributed to the silicon compound were observed from the Si2p spectrum, thus confirming that the main components of the bond materials (SiO_2) were etched by CF_4 plasma and that they became volatile products, as shown in Fig. 5.24(c). After 3-h PAP process, the surface of grinding stone was cleaned using N_2 gas blows, and the XPS measurement results of the grinding stone surface after cleaning is shown in Fig. 5.24(d). A C–C (285.0 eV) peak attributed to the diamond abrasive particles and a Si–O (103.5 eV) peak attributed to the bond materials were observed from the C1s and Si2p spectra, respectively. Only a weak peak corresponding to C–F (288.0 eV) was observed. Therefore, only an extremely thin modified layer was generated on the outermost surface of the newly exposed diamond abrasive particles. In the PAP process, because the modified abrasive particles were not firmly fixed, they fell off easily because of the friction between the grinding stone and AlN wafer (Fig. 5.24(c)). These newly exposed diamond abrasive particles were involved in the material removal process in PAP. Figure 5.24(h) shows a photograph and XPS spectrum of the polishing area on the AlN wafer surface after PAP. Since the main components of the bond materials were etched, the falling abrasive particles were not fixed or agglomerated, and they could easily be removed and accumulated on both sides of the ring-shaped polished area. Also, from the F1s spectrum, in addition to the C–F peak attributed to the modified layer of the diamond abrasive

particle, an Al-F peak attributed to the AlF_3 modified layer was observed. This is the reason why the MRR of the PAP was greater than that of conventional mechanical dry polishing with grinding stone dressing every 30 min. After the IPA ultrasonic cleaning, the grinding stone components were easily removed because no bond materials were there to fix them, as shown in Fig. 5.24(i).

5.11.2 Fine surface finishing of AlN polished surface [38)]

PAP using CF_4 plasma and vitrified-bonded grinding stone, which combined PAD and surface modification process, has been proved to be very effective for the preliminary polishing of AlN grinded surface. In this section, the polishing characteristics of PAP in the fine surface finishing of AlN polished surface was also investigated under the experimental conditions shown in Table 5.5. As shown in Fig. 5.25(a), the surface used in this study was prepared by mechanical polishing using diamond slurry. Many pits due to the shedding of grains can be observed on the surface, and the SWLI images and SEM images of AlN surface before and after polishing without plasma irradiation are shown in Fig. 5.25. Compared to the AlN surface after grinding, the surface roughness after

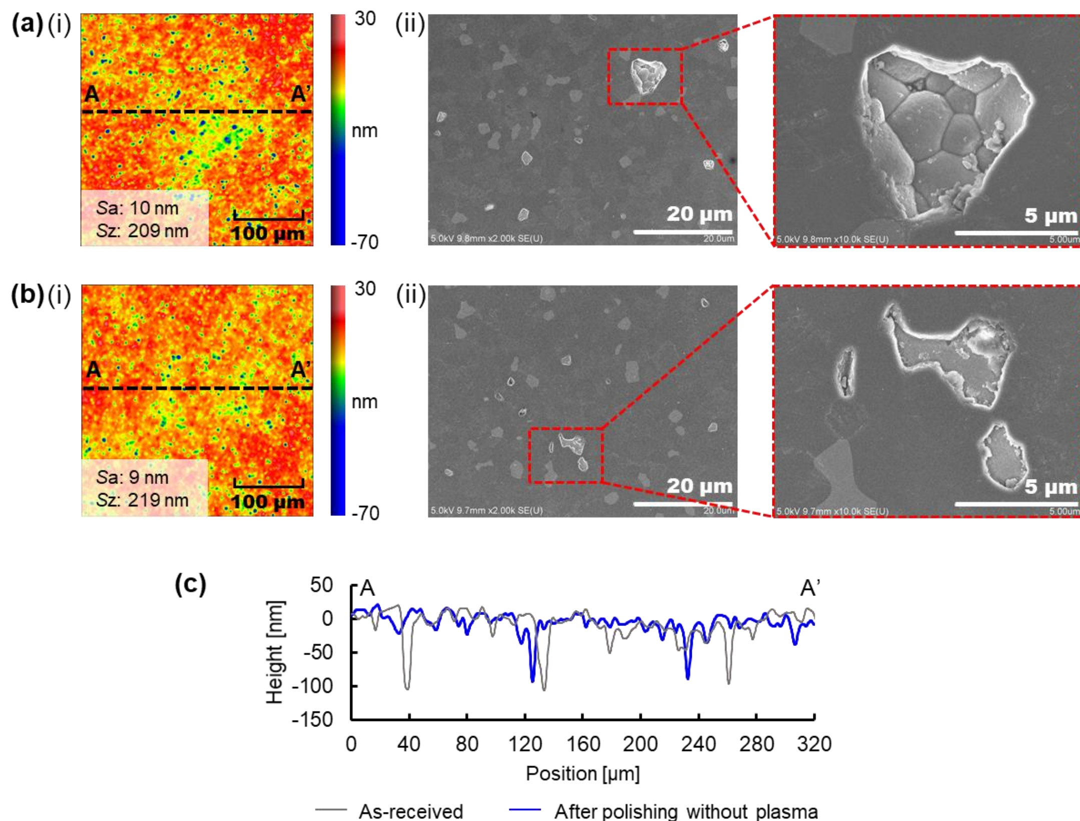

Figure 5.25 (i) SWLI and (ii) SEM images of the AlN surface (a) before polishing without plasma irradiation, (b) after polishing without plasma irradiation, and (c) cross section of the surface before and after polishing without plasma irradiation with a polishing load 800 Pa.

Table 5.5 Experimental conditions of dry polishing.

Parameters	**Conditions**
Experimental setup	Figure 5.2
Substrates	AlN ceramics (polished surface)
Abrasive material	vitrified-bonded diamond (ϕ 0.25 μm)
Polishing pressure	800 / 7000 Pa
Grinding stone rotation	121 rpm
Substrates rotation	100 rpm
Chamber pressure	800 Pa
Carrier gas	Ar (100 sccm)
Process gas	CF_4 (5 sccm)
Applied RF power	PAP: 100 W / Polishing without plasma: 0 W
Polishing time	2 hours

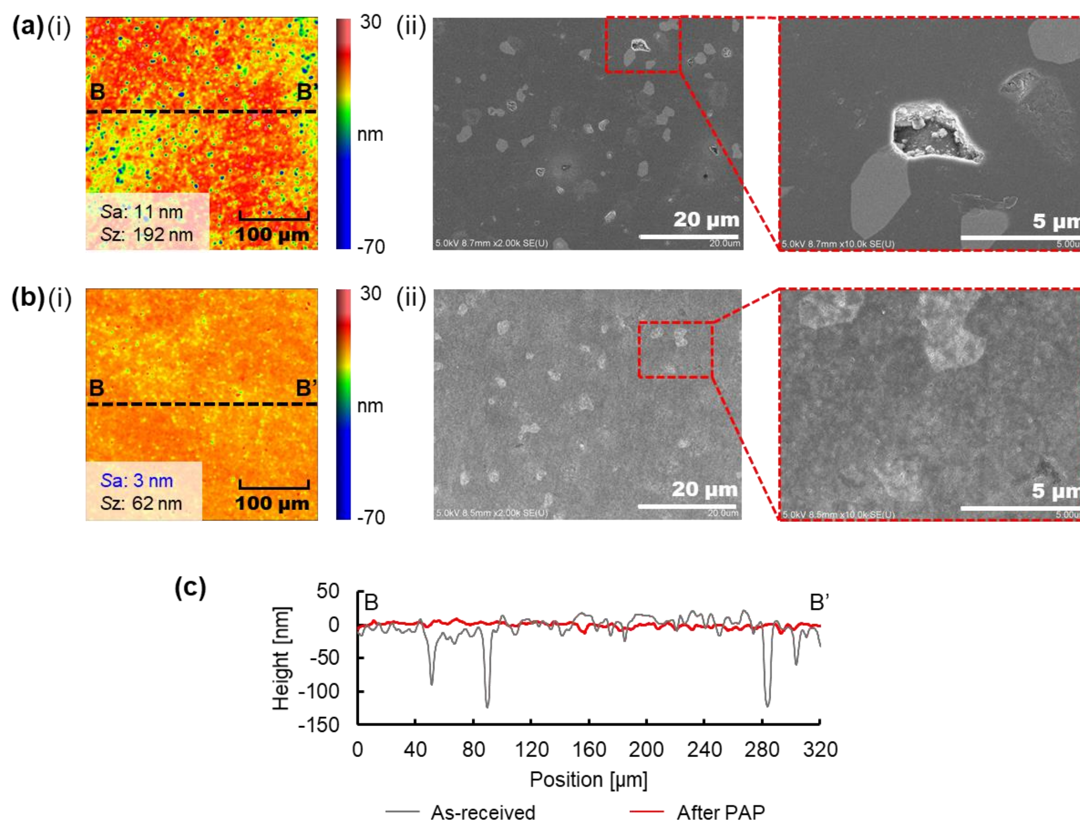

Figure 5.26 (i) SWLI and (ii) SEM images of the AlN surface (a) before PAP, (b) after PAP, and (c) cross section of the surface before and afterPAP with a polishing load 800 Pa.

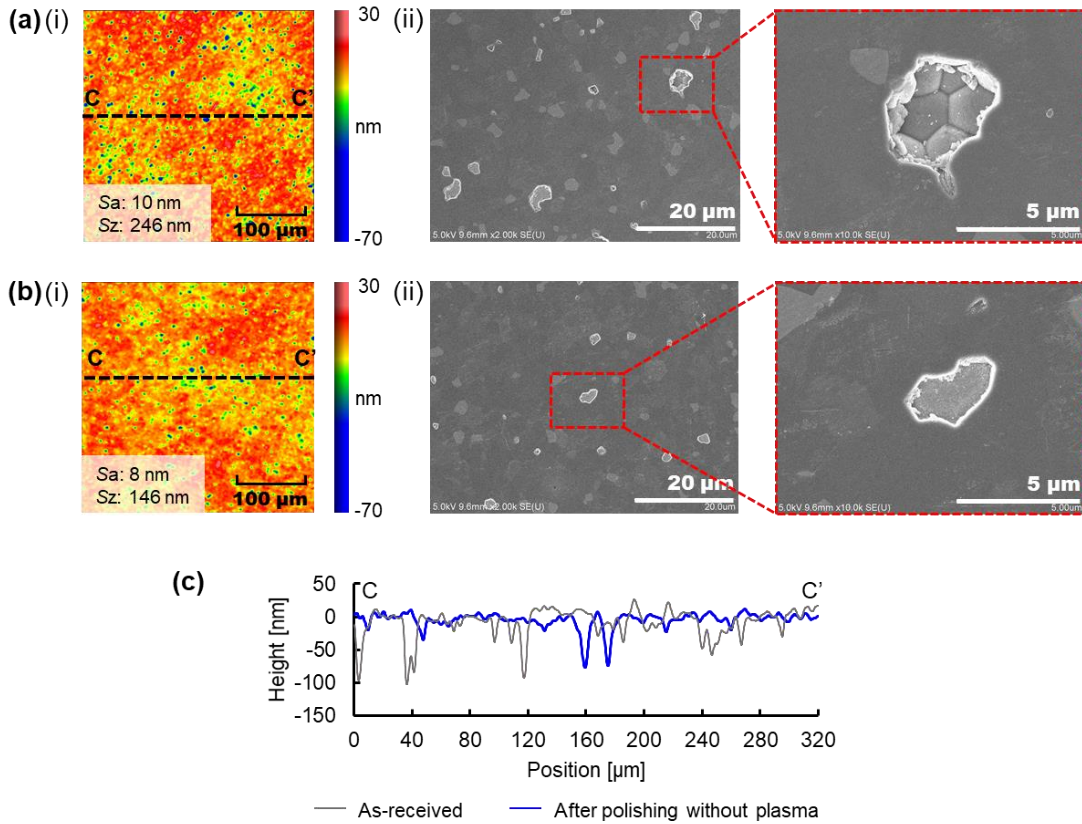

Figure 5.27 (i) SWLI and (ii) SEM images of the AlN surface (a) before polishing without plsama irradiation, (b) after polishing without plsama irradiation, and (c) cross section of the surface before and after polishing without plasma irradiation with a polishing load 7000 Pa.

polishing was much lower, which resulted to a larger contact area between AlN surface and abrasive particles. A contact area led to a smaller polishing pressure on each abrasive particle for the same polishing load. Since only ultralow polishing pressure was applied, these abrasive particles were considered to have an almost zero indentation depth, but only a slid on the AlN surface. Thus, the surface roughness *S*a of AlN remained nearly the same, and the pits remained. For PAP, although only ultralow polishing pressure was applied, the modified layer AlF_3 can be removed easily due to the increase of adhesion force between AlN surface and diamond abrasives after CF_4 plasma irradiation. After the modified layer was removed, the newly exposed AlN could not be removed by the diamond abrasives (the same situation with the polishing process without plasma irradiation), and so, only the modified layer was removed during the PAP process. The surface roughness *Sa* decreased from 10 to 3 nm for the measurement area of 315 µm × 315 µm, and no pits were observed on the polished surface as shown in Fig. 5.26. The polishing pressure was increased from 800 to 7000 Pa, while the other experimental parameters remained the same. As shown in Fig. 5.27, for the polishing without plasma irradiation, the surface roughness could not be decreased even if the

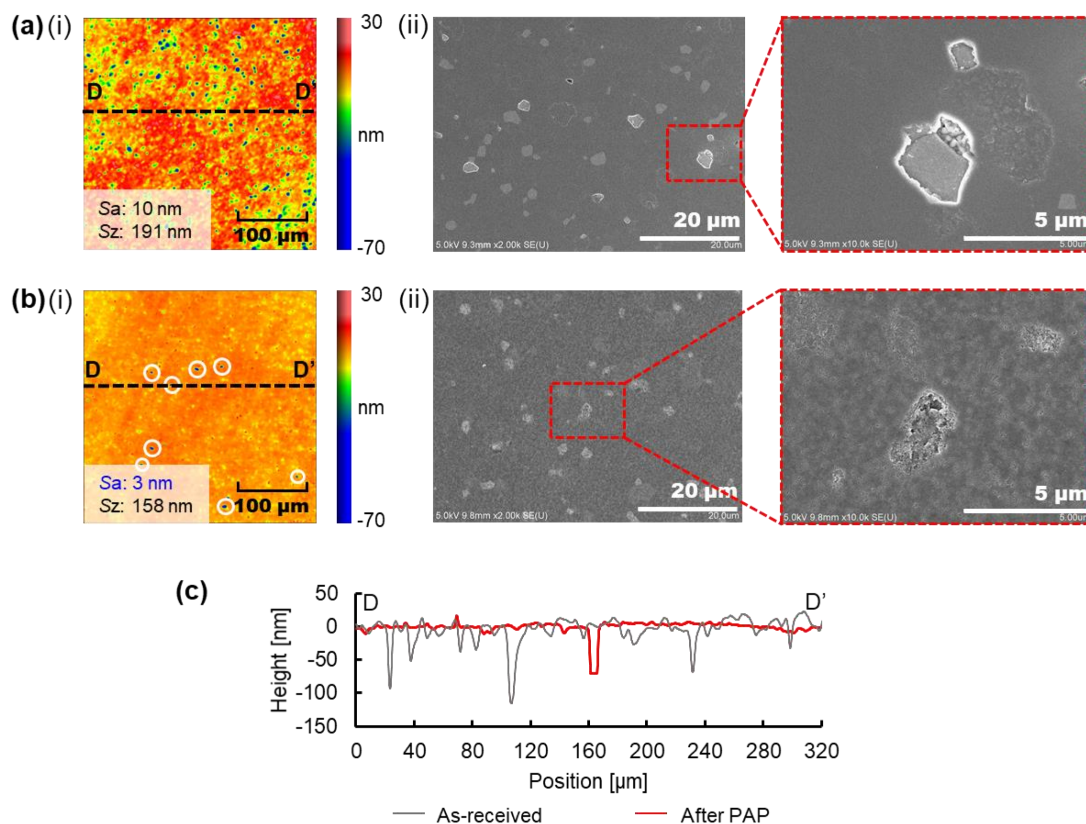

Figure 5.28 (i) SWLI and (ii) SEM images of the AlN surface (a) before PAP, (b) after PAP, and (c) cross section of the surface before and afterPAP with a polishing load 7000 Pa.

polishing pressure was increased. However, the *S*a roughness decreased because of the removal of the surface waviness after PAP, a situation like a mechanical polishing process, and pits formed locally on the surface because of the large polishing pressure (Fig. 5.28). Thus, the combination of plasma modification and ultralow-pressure polishing is essential to obtain nanometer-order surface roughness for sintered AlN.

5.12 Dress-free polishing model using CF_4 plasma and a vitrified-bonded grinding stone [39)]

Figure 5.29 shows the model of the probable mechanism for conventional mechanical dry polishing processes and the PAP process using a vitrified-bonded grinding stone. As seen from the diagram in Fig. 5.29(a), the vitrified-bonded grinding stone comprises of abrasive particles, bond materials, and holes (three main elements). After a period mechanical dry polishing with ultralow polishing pressure, worn-out abrasive particles, and bond materials fall from the grinding stone and accumulates on the AlN wafer surface. Since the polishing force was not enough to break the bonds

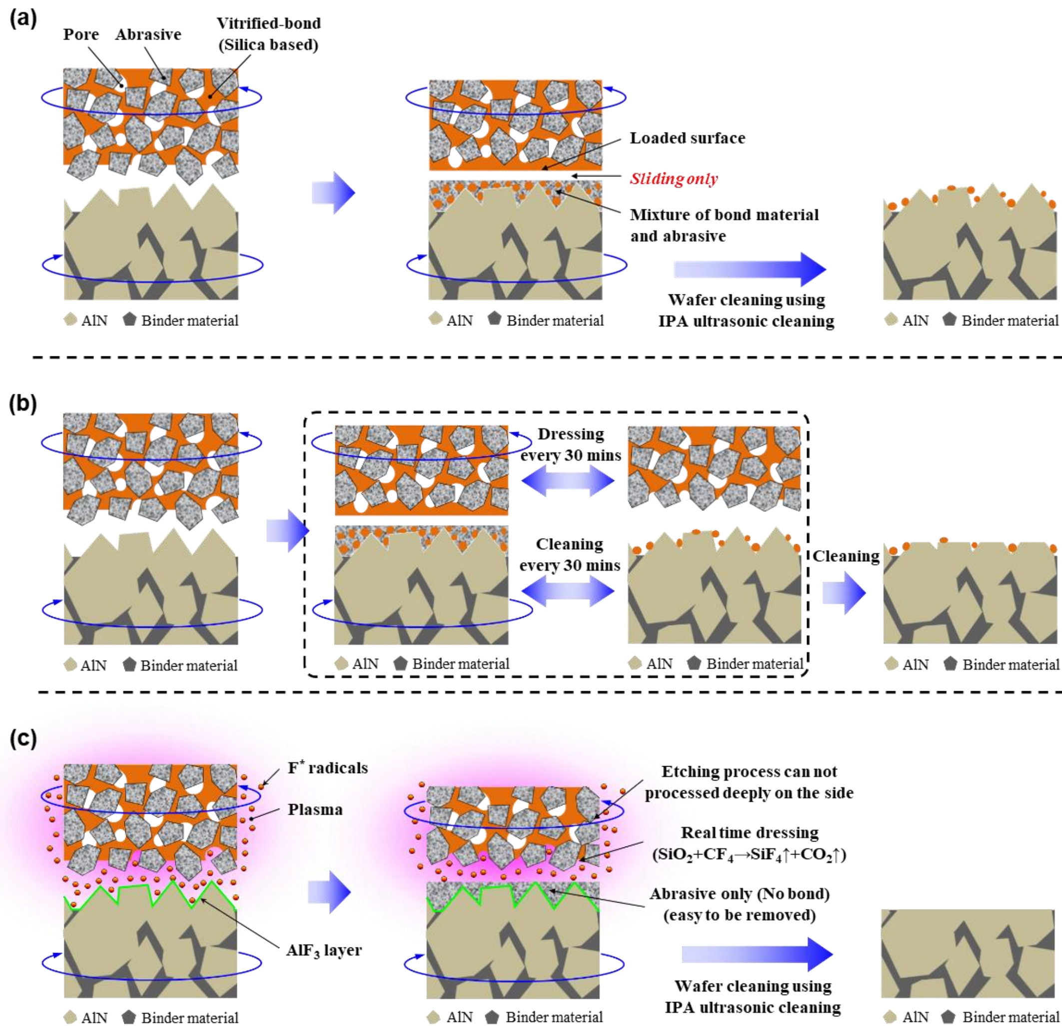

Figure 5.29 Model of the probable mechanism for (a) conventional mechanical dry polishing without dressing and for (b) conventional mechanical dry polishing with dressing every 30 min. (c) PAP using CF_4 plasma without dressing.

between the abrasive particles, self-sharpening could not occur. Thus, no new abrasive particles could be exposed. More so, the falling bonding materials fixed and agglomerated the falling abrasive particles, which could not be easily removed, on the AlN surface. In this condition, the grinding stone was only slid on the AlN surface, and the MRR was very low. The accumulated bond materials could not be removed using simple IPA ultrasonic cleaning, and an additional cleaning process was required. As shown in Fig. 5.29(b), the dressing process could effectively break the bonds between the abrasive particles and could expose new abrasive particles to maintain a great MRR. However, frequent dressing impacted both the processing efficiency and tooling costs. Figure 5.29(c) shows the probable mechanism of the dress-free polishing process in PAP. The bottom surface of the grinding stone (surface contacted with the AlN wafer) had waviness with a height of micrometer

order, which created the gap of micrometer order to allow fluorine radicals to enter the contact area. Due to the relative movement of the AlN wafer and grinding stone, fluorine radicals attached to the AlN surface are continuously in contact with the bottom surface of the grinding stone. The fluorine radicals generated in the CF_4 plasma could modify the AlN wafer surface and react with SiO_2, which is the main component of the bond materials. The bonds between the abrasive particles were etched, and worn-out abrasive particles could be removed easily by the polishing force, which is equivalent to the continuous dressing of the grinding stone surface without impacting the processing efficiency. Due to the real-time PAD, new abrasives was constantly exposed, and a great MRR was maintained. On the side surface of the grinding stone, although SiO_2, which is the main component of bond materials, could be etched by the fluorine radicals in CF_4 plasma, the other components in bond materials (related to company patent that cannot be disclosed) could not react with the fluorine radicals. Thus, the abrasive particles were still fixed with weak bonding force and did not fall off because there was no polishing force acting on the side of the grinding stone. As the fluorine radicals could only react with the SiO_2 exposed on the surface, the diamond abrasive particles and other component of bond materials did not react with CF_4 and did not fall off. Thus, the deeper bond materials were not etched, and therefore only the contact surface of the grinding stone was constantly dressed by plasma, and the side surface of the grinding stone was not continuously dressed. The AlN surface was modified into an AlF_3 layer, which is easier to remove, resulting in a greater MRR than that of conventional mechanical dry polishing processes with frequent dressing. Also, the accumulated abrasive particles on the AlN surface was easily be removed due to the absence of the bond materials.

5.13 Summary

In this chapter, a novel dry high-efficiency dress-free polishing technique using CF_4 plasma and a vitrified-bonded grinding stone was achieved. By considering the changes in the surface morphology of AlN surface and grinding stone surface before and after polishing under different polishing conditions, and the analysis of the composition of the attachment, a probable mechanism for dress-free polishing in PAP process was proposed.

(1) Slurry was widely used in polishing of difficult-to-machine materials. However, has some limitations, such as the agglomeration of abrasives and high disposal cost. Although using fixed abrasive grains instead of slurry can solve these issues, the problems of wear and of loading fixed abrasive grinding stones, which result in decrease of MRR, also need to be solved. Since frequent dressing of the grinding stone results in a low processing efficiency, many research have been conducted on the need for. self-sharpening of fixed abrasive grinding stones.

However, the self-sharpening of grinding stones is not efficient with ultralow polishing pressure, which is not large enough to break bonds to expose new abrasives.

(2) As an ultraprecision dry polishing technique, PAP has been successfully applied to polish many difficult-to-machine materials. However, since fixed abrasives were used in PAP, the loading of grinding stone also greatly limited the MRR in PAP. Although a self-sharpening technique of metal-bonded grinding stones using ELID has been developed by H. Ohmori *et al.*, metal-bonded grinding stones cannot be used in PAP. Hence, a method that can achieve in-process dressing in PAP process, which can greatly improve the MRR in PAP, is desired.

(3) As a target material for vacuum PAP, sintered AlN ceramic was considered in this work. High-quality precision polishing of sintered ceramic materials was very difficult due to grains tend to shed off the surface during mechanical dry polishing processes. However, this shedding can be avoided, and the grains were flattened from the top using a vitrified-bonded grinding stone with small abrasive particles and by applying ultralow polishing pressure.

(4) The surface of the vitrified-bonded grinding stone was loaded, and it easily lost its polishing ability. Also, it was proved that the MRR of the mechanical dry polishing process with dressing every 30 min was 1.5 times higher than that without dressing. Thus, to maintain great MRRs, the frequent dressing of grinding stones is necessary for conventional mechanical dry polishing processes.

(5) The surface of AlN can be modified to AlF_3 by the irradiation of Ar-based CF_4 plasma. Through the measurement of the force-distance curve between diamond tip and AlN wafer before and after CF_4 plasma irradiation, it was confirmed that the adhesion force between diamond tip and AlN wafer was significantly increased after CF_4 plasma irradiation. Therefore, during the actual PAP process, it is considered that the adhesion force between the diamond abrasive particles and the AlF_3 modified layer was also increased, which made the AlF_3 modified layer can be removed much easier than before plasma irradiation.

(6) In the case of PAP using CF_4 plasma and a vitrified-bonded grinding stone, the CF_4 plasma irradiation not only generated an easily removable and modified AlF_3 layer on the AlN surface but also dressed the grinding stone surface simultaneously by etching the main components of the bond materials. Owing to the PAD simultaneously occurring in the PAP process, a novel highly-efficient dress-free polishing process was realized. Thus, the combined contribution of

PAP and PAD resulted in twice the MRR compared with mechanical dry polishing processes without dressing.

(7) In the manufacturing process of functional ceramic materials, ultralow pressure dry polishing using CF_4 plasma and vitrified-bonded grinding stones with small abrasive is a very promising technique for replacing conventional mechanical polishing processes.

References

1) A. F. Junior, D. J. Shanafield, Thermal conductivity of polycrystalline aluminum niturde (AlN) ceramics, *Ceramica.* **50** (2004) 247-253.
2) I. Yonenaga, Thermo-mechanical stability of wide-bandgap semiconductors: high temperature hardness of SiC, AlN, GaN, ZnO and ZnSe, *Physica B*. **308-310** (2001) 1150-1152.
3) Y. Zhou, G. Pan, X. Shi, *et al.*, Chemical mechanical planarization (CMP) of on-axis Si-face SiC wafer using catalyst nanoparticles in slurry, *Surface & Coatings Technology.* **251** (2014) 48-55.
4) H. Aida, H. Takeda, K. Koyama, *et al.*, Chemical mechanical polishing of gallium nitride with colloidal silica, *Journal of The Electrochemical Society.* **158** (2011) H1206-H1212.
5) K. Yamamura, T. Takiguchi, M. Ueda, *et al.*, Plasma assisted polishing of single crystal SiC for obtaining atomically flat strain-free surface, *CIRP – Manufacturing Technology.* **60** (2011) 571-574.
6) H. Deng, K. Endo, K. Yamamura, Plasma-assisted polishing of gallium nitride to obtain a pit-free and atomically flat surface, *CIRP Annals – Manufacturing Technology.* **64** (2015) 531-534.
7) H. Eichhorn, K. H. Schoenbach, T. Tessnow, Paschen’s low for a hollow cathode discharge, *Applied Physics Letters*. **63** (1993) 2481-2483.
8) L. Bardos, H. Barankova, Cold atmospheric plasma: Sources, processes, and applications, *Thin Solid Films.* **518** (2010) 6705-6713.
9) O. Ohnishi, H. Suzuki, E. Uhlmann, et al., Handbook of Ceramics Grinding and Polishing (Second Edition) – Chapter 4 – Grinding, *William Andrew Publishing*. (2015) 133-233.
10) K. Wegener, H. W. Hoffmeister, B. Karpuschewski, *et al.*, Conditioning and monitoring of grinding wheels, *CIRP Annals – Manufacturing Technology*. **60** (2011) 757-777.
11) R. Mohan, R. Deivanathan, A review of self-sharpening mechanisms of fixed abrasive tools, *International Journal of Mechanical Engineering and Technology.* **10** (2019) 965-974.
12) Y. Gu, W. Zhu, J. Lin, *et al.*, Subsurface damage in polishing process of silicon carbide ceramic, *Materials.* **11** (2018) 506.
13) G. Wang, Y. Wang, Z. Xu, Modeling and analysis of the material removal depth for stone polishing, *Journal of Materials Processing Technology.* **209** (2009) 2453-2463.

14) Y. Zhou, M. Atwood, D. Golini, *et al.*, Wear and self-sharpening of vitrified bond diamond wheels during sapphire grinding, *Wear.* **219** (1998) 42-45.
15) Area Roughness Parameters. Surface texture parameters in ISO 25175. https://www.keyence.eu/ss/products/microscope/roughness/surface/tab03_b.jsp
16) J. Qian, H. Ohmori, W. Lin, Internal mirror grinding with a metal/metal-resin bonded abrasive wheel, *International Journal of Machine Tools & Manufacture.* **41** (2001) 193-208.
17) H. Ohmori, T. Nakagawa, Mirror surface grinding of silicon wafers with electrolytic in-process dressing, *CIRP Annals.* **39** (1990) 329-332.
18) H. Ohmori, I. Takahashi, B. P. Bandyopadhyay, Ultra-precision grinding of structural ceramics by electrolytic in-process dressing (ELID) grinding, *Journal of Materials Processing Technology.* **57** (1996) 272-277.
19) D. J. Stephenson, X. Sun, C. Zervos, A study on ELID ultra precision grinding of optical glass with acoustic emission, *International Journal of Machine Tools & Manufacture.* **46** (2006) 1053-1063.
20) S. Yin, H. Ohmori, Y. Dai, *et al.*, ELID grinding characteristics of glass-ceramic materials, *International Journal of Machine Tools & Manufacture.* **49** (2009) 333-338.
21) H. Deng, Development of plasma-assisted polishing for highly efficient and damage-free finishing of single-crystal SiC, GaN and CVD-SiC, *Doctoral Dissertation, Osaka University Knowledge Archive*, 2016.
22) L. Rosenberger, R. Baird, E. McCullen, *et al.*, XPS analysis of aluminum nitride films deposited by plasma source molecular beam epitaxy, *Surface and Interface Analysis.* **40** (2008) 1254-1261.
23) R. Ramos, G. Cunge, O. Joubert, *et al.*, Plasma/reactor walls interactions in advanced gate etching processes, *Thin Solid Films.* **515** (2007) 4846-4852.
24) N. Chen, C. Wang, J. Hwang, *et al.*, MOCVD Al nanocrystals embedded in AlO_xN_y thin films for nonvolatile memory, *ECS Journal of Solid State Science and Technology.* **1** (2012) 190-196.
25) M. Watanabe, Y. Mori, T. Ishikawa, *et al.*, Thermal reaction of polycrystalline AlN with XeF_2, *Journal of Vacuum Science & Technology A.* **23** (2005) 1647-1656.
26) A. Kawai, H. Nagata, M. Takata, Characterization of surface energetic behavior by atomic force microscopy, *Japanese Journal of Applied Physics.* **31** (1992) L977-L979.
27) H. A. Mizes, K. G. Loh, R. J. D. Miller, *et al.*, Submicron probe of polymer adhesion with atomic force microscopy: Dependence on topography and material inhomogeneities, *Applied Physics Letters.* **59** (1991) 2901-2903.
28) AFM Modes and Theory – AFM Force Spectroscopy. https://www.nanosurf.com/en/support/afm-modes-overview/force-spectroscopy
29) N. A. Burnham, R. J. Colton, Measuring the nanomechanical properties and surface forces of materials using an atomic force microscope, *Journal of Vacuum Science & Technology A.* **7** (1989) 2906.

30) D. B. Asay, S. H. Kim, Effects of adsorbed water layer structure on adhesion force of silicon oxide nanoasperity contact in humid ambient, *The Journal of Chemical Physics.* **124** (2006) 174712.

31) R. Sun, X. Yang, K. Watanabe, *et al.*, Etching characteristics of quartz crystal wafers using argon-based atmospheric pressure CF_4 plasma stabilized by ethanol addition, *Nanomanufacturing and Metrology*. **2** (2019) 167-176.

32) R. Sun, X. Yang, Y. Ohkubo, *et al.*, Optimization of gas composition used in plasma chemical vaporization machining for figuring of reaction-sintered silicon carbide with low surface roughness, *Scientific Reports*. **8** (2018) 2376.

33) K. Paprocki, A. D. Wituski, M. Trzcinski, *et al.*, The comparative studies of HF CVD diamond films by Raman and XPS spectroscopies, *Optical Materials.* **95** (2019) 109251.

34) Carbon. XPS simplified. https://www.jp.xpssimplified.com/elements/carbon.php

35) R. Alfonsetti, L. Lozzi, M. Passacantando, *et al.*, XPS studies on SiO_x thin films, *Applied Surface Science*. **70/71** (1993) 222-225.

36) X. Chen, X. Wang, D. Fang, A review on C1s XPS-spectra for some kinds of carbon materials, *Fullerenes, Nanotubes and Carbon Nanostructures.* **28** (2020) 1048-1058.

37) N. Vandencasteele, F. Reniers, Plasma-modified polymer surfaces: Characterization using XPS, *Journal of Electron Spectroscopy and Related Phenomena.* **178-179** (2010) 394-408.

38) R. Sun, X. Yang, K. Arima, *et al.*, High-quality plasma-assisted polishing of aluminum nitride ceramic, C*IRP Annals – Manufacturing Technology*. **69** (2020) 301-304.

39) R. Sun, A. Nozoe, J. Nagahashi, *et al.*, Novel highly-efficient and dress-free polishing technique with plasma-assisted surface modification and dressing, *Precision Engineering.* **72** (2021) 224-236.

Chapter 6
Summary

An ultraprecision manufacturing process named plasma nanomanufacturing process, which combines PCVM and PAP, was proposed for the high accuracy, damage-free, slurry-free, and low-cost manufacturing of difficult-to-machine brittle functional materials, such as ultrathin quartz crystal wafer, reaction-sintered silicon carbide (RS-SiC) and AlN ceramics for different application target in this study.

In Chapter 1, the background of the study was presented. The properties, and applications of the difficult-to-machine brittle functional materials were presented and the aims of this study were introduced.

In Chapter 2, to realize the highly efficient, cost effective, and damage-free nanoscale manufacturing of different difficult-to-machine brittle functional materials for different target, a review of the current figuring and polishing technique was conducted and their advantages and disadvantages were summarized. Plasma nanomanufacturing process, which combines PCVM and PAP, was proposed. In this chapter, the basics of plasma for different processes, and the concepts and strategies of plasma nanomanufacturing process were described.

(1) High-efficient, low-cost, and high-quality damage-free ultraprecision manufacturing of difficult-to-machine brittle functional is difficult due to their high hardness and chemical inertness. In recent years, several figuring and polishing techniques have been developed for these materials. However, there are still several challenges associated with these polishing techniques such as the low polishing efficiency, high cost, and limitation of applicable materials.

(2) Due to its chemical activity and high reactivity, plasma is considered as a low-cost and effective processing tool for difficult-to-machine brittle functional materials. Frequent collisions between electrons and gas molecules/atoms in plasma can cause the reactions such as excitation, deexcitation, ionization, and dissociation. Since the released energy is related to the inherent properties of each atom or molecule, by measuring the characteristic emission light during the deexcitation process, the properties of the plasma can be monitored, making

the plasma become a controllable processing tool.

(3) As an efficient noncontact figuring technique with good form accuracy, PCVM has been successfully applied for the ultraprecision figuring of Si-based materials. However, PCVM cannot be used for finishing because of the isotropy of the etching process. As an excellent dry polishing technique, PAP has been proven to achieve damage-free finishing of a variety of difficult-to-machine brittle functional materials and obtain an atomically smooth surface. However, the problem of low MRR still needs to be resolved.

(4) Plasma nanomanufacturing process, which combines PCVM and PAP, was proposed in this study. Plasma nanomanufacturing combines the advantages of the two techniques and addresses the limitations in both processes. It is expected to achieve a highly efficient, cost effective, and damage-free nanoscale manufacturing of different difficult-to-machine brittle functional materials for different target.

In Chapter 3, as a part of plasma nanomanufacturing process, AP-PCVM has been successfully applied to improve the thickness uniformity of ultrathin quartz crystal wafer in the previous study. Helium, a gas with high cost and unstable supply, has been used as a carrier gas in AP-PCVM till date. Although argon, which is a low cost and easier to manufacture gas from liquid air, is also commonly used in vacuum plasma as the carrier gas. Since the high breakdown voltage for argon at atmospheric pressure easily leads to the formation of filamentary arc streamers, which can break a quartz crystal wafer, argon has not been used in AP-PCVM as the carrier gas to correct the thickness distribution of a quartz crystal wafer till date. In this chapter, it was confirmed that the plasma can be stabilized by adding a small fraction of ethanol into Ar, and the etching characteristics of ultrathin quartz crystal wafer by AP-PCVM using ethanol-added Ar as the carrier gas was investigated.

(1) The difference between He plasma and Ar plasma at AP was well explained using the Penning effect. The addition of a small fraction of ethanol to Ar can generate atmospheric-pressure plasma with a stable glow discharge state instead of arc streamers due to the Penning effect between metastable states Ar atoms and ethanol molecules.

(2) The etching characteristics of ultrathin quartz crystal wafer obtained by AP-PCVM using ethanol-added Ar-based atmospheric-pressure CF_4 plasma was investigated. Due to the incompletely decomposed carbon from ethanol, a large amount of carbon deposit was formed on quartz crystal wafer after AP-PCVM using ethanol-added Ar as the carrier gas. The

experimental results proved that the addition of oxygen into the process gas can suppress the formation of the carbon deposit.

(3) Since oxygen itself did not contribute to the etching reaction of the quartz crystal, and the generation of O and F radicals, of which both require the energy from Ar in the active state, the competition between O_2 and CF_4, however, led to a decrease in the etching rate at high oxygen fractions. An O_2 flow rate of 4 sccm is suitable because of the high etching rate that can be obtained without carbon deposition.

(4) Comparative experiments were conducted on ultrathin quartz crystal wafers in AP-PCVM using He and ethanol-added Ar as the carrier gas (the other experimental conditions were same). Since He has a much lower mass than air, and Ar has a higher mass than air, so the area of plasma using ethanol-added Ar as the carrier gas was wider than that of using He as the carrier gas. The diameter of the removal spot formed using ethanol-added Ar as the carrier gas was larger than that of the spot formed using He, though the maximum depth was lower. However, the volumetric removal rate using He and ethanol-added Ar were almost the same.

(5) Since the same etching rate was obtained using He or ethanol-added Ar as the carrier gas in AP-PCVM, and the removal volume was proportional to the processing time in both cases, hence it is considered that using argon instead of helium as the carrier gas in AP-PCVM will effectively solve problems such as the depletion of natural resources and high cost.

In Chapter 4, since AP-PCVM can quickly remove LSFR without the formation of SSD, and PAP can remove HSFR and achieve an atomically smooth surface, then plasma nanomanufacturing process, which combined AP-PCVM and PAP is considered a very suitable processing method to process RS-SiC. However, as a pure chemical processing method, the application of AP-PCVM to multicomponent materials such as RS-SiC faces many challenges, in this chapter, through the optimization of a variety of processing conditions, AP-PCVM was successfully applied to RS-SiC and a smooth surface was obtained. Until dateAP-PCVM was firstly applied to process a multicomponent material, which further broadened the application area of plasma nanomanufacturing process.

(1) A microwave plasma generator with special structure was used in this work. To clarify the mixed state of the carrier gas and the process gas before and after being ejected from the plasma generator, CFD fluid simulation was carried out. The CFD fluid simulation results better explained the reason why the etching rate and the shape of the removal spot changed

with the variation of the processing gap in AP-PCVM.

(2) Since the process gas was introduced from the other gas inlets and mixed with the carrier gas, enough time and distance were needed to enable a good mixture. However, due to insufficient mixing, a circular removal spot was obtained because the distribution of CF_4 was circular at a small processing gap. In contrast, a removal spot with Gaussian-shape was obtained at a relatively large processing gap, where the process gas (CF_4) was fully mixed with the carrier gas. The distribution in the direction of the injection can also explain the correlation between the etching rate and the processing gap. Since the Ar plasma (generated for the first time using carrier Ar gas), which is the energy source, hit the substrate and lost its energy before being mixed and collided with the ground state CF_4 to generate F radicals, the etching rate was low at small processing gap. But with the increase of the processing gap, carrier Ar and CF_4 were fully mixed, and the energy of Ar plasma was transferred to CF_4 to generate F radicals, and the etching rate also increased. The processing gap 6 mm, where the removal spot with good shape can be obtained and the change rate of etching rate was small, was considered as the optimal processing gap.

(3) According to the comparison of the SEM images, SWLI images and EDS spectra of the RS-SiC surface before and after AP-PCVM, the difference in the etching rate of the Si and SiC components was the main reason for the deterioration of surface roughness. This is also the reason why AP-PCVM was difficult for processing multicomponent materials like RS-SiC.

(4) Upon optimizing the oxygen fraction of the process gases, the etching rates of both Si (100) and 4H-SiC (0001) changed. Due to the promoting effect of oxygen on the formation of F radicals in CF_4 plasma, the etching rate reached the maximum at a certain oxygen fraction and decreased due to the competitive relationship between the oxidation and etching process as the oxygen fraction further increased. When the oxygen fraction was 90%, the etching rate of Si (100) coincides with that of 4H-SiC (0001). From the XPS spectra of the processed surface, the mechanism responsible for the coinciding of the etching rate of the two components in RS-SiC was seen to be the result of the competition between the oxidation process and the etching process. At high oxygen fraction, the oxidation reaction dominated the AP-PCVM process. Both two components were firstly oxidized to SiO_2 and was later etched, and thus, the Si and SiC components were removed at the same rate.

(5) The results of raster scanning experiments also proved that, when the oxygen fraction in-process gas was lower than 90%, the etching rate of Si was greater than that of SiC and the

surface roughness deteriorates since the region of Si becomes hollow. And when the oxygen fraction was higher than 90%, the etching rate of SiC becomes greater than that of Si, and the surface roughness also deteriorated due to the protruded regions of Si. SiC and Si could be etched at the same rate, and a smoothly etched surface will be obtained, only when the oxygen fraction is 90%.

(6) Aspherical shape figuring experiment using the optimal processing conditions was also conducted on RS-SiC by AP-PCVM. The diameter of fabricated shape was the same with target shape, but the depth was shallower than the target. The redeposition of reaction products is considered the cause of this result. Heating of the substrate was effective in preventing the redeposition of reaction products., but however, a highly substrate temperature also caused the decrease in the adsorption rate of reactive radicals, thereby resulting in the decrease of the etching rate. Therefore, there is need for the optimization of the substrate temperature.

(7) AP-PCVM can achieve figuring efficiently without forming SSD, but a further polishing is required to obtain an atomically smooth surface. In plasma nanomanufacturing, PAP plays the role of surface finishing, and the related work will be carried out in the future.

In Chapter 5, a novel dry high-efficiency dress-free polishing technique using CF_4 plasma and a vitrified-bonded grinding stone was achieved. By considering the changes in the surface morphology of AlN surface and grinding stone surface before and after polishing under different polishing conditions, and the analysis of the composition of the attachment, a probable mechanism for dress-free polishing in PAP process was proposed.

(1) Slurry was widely used in polishing of difficult-to-machine brittle functional materials. However, it has limitations such as the agglomeration of abrasives and high disposal cost. Although using fixed abrasive grains instead of slurry can overcome these limitations, the challenge of wear and of loading fixed abrasive grinding stones, which causes the decrease of MRR, also need to be solved. Since frequent dressing of the grinding stone results in a low processing efficiency, many researches have been conducted on the self-sharpening of fixed abrasive grinding stones. However, the self-sharpening of grinding stones is not efficient with ultralow polishing pressure, which is not large enough to break bonds to expose new abrasives.

(2) As an ultraprecision dry polishing technique, PAP has been successfully applied to polish many difficult-to-machine brittle functional materials. However, since fixed abrasives were used in

PAP, the loading of grinding stone also greatly limited the MRR in PAP. Although a self-sharpening technique of metal-bonded grinding stones using ELID has been developed by H. Ohmori *et al.*, metal-bonded grinding stones cannot be used in PAP. Hence, a method that can achieve in-process dressing in PAP process, which can greatly improve the MRR in PAP, is desired.

(3) As a target material for vacuum PAP, sintered AlN ceramic was considered in this work. High-quality precision polishing of sintered ceramic materials was very difficult since grains tend to shed off from the surface during mechanical dry polishing processes. However, this shedding can be avoided, and the grains could be flattened from the top using a vitrified-bonded grinding stone with small abrasive particles and by applying ultralow polishing pressure.

(4) The surface of the vitrified-bonded grinding stone was loaded, but can easily loose its polishing ability. It was proved that the MRR of the mechanical dry polishing process with dressing every 30 min was 1.5 times higher than that without dressing. Thus, to maintain great MRRs, the frequent dressing of grinding stones is necessary for conventional mechanical dry polishing processes.

(5) The surface of AlN can be modified to AlF_3 by the irradiation of Ar-based CF_4 plasma. Through the measurement of the force-distance curve between diamond tip and AlN wafer before and after CF_4 plasma irradiation, it was confirmed that the adhesion force between diamond tip and AlN wafer was significantly increased after CF_4 plasma irradiation. Therefore, during the actual PAP process, it is considered that the adhesion force between diamond abrasive particles and the AlF_3 modified layer increased, which allows easier removal of the AlF_3 modified layer than before plasma irradiation.

(6) In the case of PAP using CF_4 plasma and a vitrified-bonded grinding stone, the CF_4 plasma irradiation not only generated an easily removable and modified AlF_3 layer on the AlN surface but also dressed the grinding stone surface simultaneously by etching the main components of the bond materials. Owing to the PAD simultaneously occurring in the PAP process, a novel highly efficient dress-free polishing process was realized. Thus, the combined contribution of PAP and PAD resulted in twice the MRR compared with mechanical dry polishing processes without dressing.

(7) In the manufacturing process of functional ceramic materials, ultralow pressure dry polishing, using CF_4 plasma and vitrified-bonded grinding stones with small abrasive particles is a very promising technique for replacing conventional mechanical polishing processes.

In this study, plasma nanomanufacturing process was applied to ultrathin quartz crystal wafer, RS-SiC and AlN ceramics. For thickness correction of ultrathin quartz crystal wafer by AP-PCVM, the replacement of He using ethanol-added Ar as the carrier gas enabled the commercialized AP-PCVM technology successfully get rid of the unstable supply of He, and reduced production costs by of ensuring increased removal rate. By optimizing the gas composition used in AP-PCVM, the etching rate of the two components in RS-SiC coincided, and a smooth processed RS-SiC surface was obtained. AP-PCVM was firstly applied to process a multicomponent material, and thus further broadened the application area of plasma nanomanufacturing. Furthermore, owing to the combined contribution of PAP and PAD, a novel highly efficient dress-free polishing process was realized. A double MRR compared with mechanical dry polishing and a surface roughness Sa 3nm, which exceed the limits of conventional mechanical polishing method, has been obtained. As a high accuracy, damage-free, slurry-free, and low-cost manufacturing process, plasma nanomanufacturing process is strongly expected to be used in industrial applications such as in the processing of wide-gap semiconductor substrates, glass lens molds, functional ceramic materials, telescope mirrors, *etc*.

Acknowledgments

Six years ago, I graduated from Jilin University (Changchun, China). Before I could experience the joy of graduation, I came directly to Japan and embarked on another journey. Because of language barriers and cultural differences, the initial study abroad life was full of difficulties and bitterness. However, after experiencing countless successes and failures in daily life and academics, now I have to say, the six years of studying abroad has truly broadened my horizons and changed the trajectory of my life.

I would like to acknowledge and give my warmest thanks to my supervisor (Professor Kazuya Yamamura), who has influenced me the most in my academic career. From the interview in the room of Professor Kazuya Yamamura on the evening of January 20, 2016, my 6-year research life in the Yamamura Lab started. Thank you for your guidance, advice, academic rigor and your daily care. Although I felt disappointed and cried countless times because of my experiment results, even after giving it my best and it would not work, yet you will encourage me to do more. But it was yet, precisely because of your academic rigor that I made a rapid progress and experience the joy of successful experiments, my first overseas academic presentation, the first award, and the first journal paper publication. I will always be grateful because I couldn't have achieved all these without you. I am also grateful to Professor Katsuyoshi Endo, Associate Professor Kenta Arima, Assistant Professor Yuji Ohkubo, Assistant Professor Kentaro Kawai, and Assistant Professor Xu Yang, for giving me a lot of advice and guidance in my daily research, and also to all the professors in the Department of Precision Engineering, Graduate School of Engineering of Osaka University, including Professor Kazuto Yamauchi, Professor Kiyoshi Yasutake, Professor Yuji Kuwahara, Professor Hirotsugu Ogi, Professor Yoshitada Morikawa, Professor Heiji Watanabe, Associate Professor Yasuhisa Sano, and so on, for their valuable comments and advice on my research. I am also grateful to Mr. Keiichiro Watanabe and Mr. Daiki Morimoto from Kyocera Corporation, Mr. Masao Matsuda from Shimadzu Corporation, Mr. Masashi Adachi from Meisyokiko Corporation for their support on my research.

I would like to thank the current members of the Plasma Group including Mr. Nian Liu, Mr. Yugo Yamamoto, Mr. Naoya Yoshitaka, Mr. Tong Tao, Mr. Hayato Kitade, Mr. Kentaro Sugimoto, Mr. Kenta Suba and the graduate members including Assistant Professor Hui Deng, Mr. Yuiki Goto, Mr. Syogo Sakaiya, Mr. Hisaya Dojo, Mr. Yuki Kobayashi, Mr. Kentaro Tsujiuchi, Mr. Ken Emori, Mr. Shohei Arakawa, and Mr. Ren Suzuki for their support and help. I sincerely appreciate the support of the other members of Yamamura Lab and Research Center for Ultra-Precision Science & Technology, such as Ms. Xiaozhe Yang, Junhuan Li, Zhida Ma, Haiyang Gu, and on the rest. I

would like to extend my sincerest thanks to Ms. Yukari Ogawa, the secretary of Yamamura laboratory, for her patient and kind support and for encouraging me in my daily life.

This work was partially supported by Japan Science and Technology Agency Adaptable and Seamless Technology transfer Program through target-driven R&D (JST A-STEP) Grant Number JPMJTS1623, Japan; Japan Society for the Promotion of Science (JSPS) KAKENHI Grant Number 18H03754 and JP19J20167; and a Grant-in-Aid for JSPS Fellows (201920167). Furthermore, I would like to express my gratitude to Kyocera Corporation for providing the ultra-thin quartz crystal wafers, to CoorsTek, Inc. for providing the AlN substrates, to Mizuho Co., Ltd. for providing the vitrified-bonded grinding stone.

Finally, I thank my parents, my wife, and my friends, who have always believed in me, encouraged me, and given me all their support whenever I have needed it. You shared my pain to reduced my sadness, and shared my joy to multiplied my happiness. Your continuous support for me was what sustained me this far. I feel so lucky to be your son, your husband, and your friends.